Simulation of Dynamic Triggering of Acoustic Emissions using a Bonded-Particle Method

by

Hang Lu

A thesis submitted in partial fulfillment of the requirements for the degree of

Master of Science

in

GEOPHYSICS

Department of Physics
University of Alberta

Abstract

Microseismic events are commonly recorded during hydraulic fracturing experiments. In microseismic interpretations, each event is often regarded as causally independent and uncorrelated to neighbouring ones. In reality, both the rock deformation (static stresses) and transient wave motion (dynamic stresses) associated with microseismic events influence the stress field together with the external loading (fluid injection). It is thus very likely that many microseismic events are caused by both static and dynamic stress changes. In other words, some events may be caused by propagation of transient waves instead of the stress changes purely related to fluid injection. In this thesis, dynamic triggering of acoustic emissions is studied as an analogy of microseismic events using Bonded Particle Method (BPM). A biaxial deformation test on a rock core sample is simulated. First, a major event is created and how dynamic waves influence the occurrence of the subsequent ones is qualitatively and quantitatively studied. Then an external vibration is applied to the model to investigate the influence of transient wave motion on failure in a controlled fashion. It is found that dynamic stresses can alter the stress field and hence cause a favorable change in the stress state for bond breakages. The external vibration can advance the formation of the upcoming large local failure events

and delay or advance the final catastrophic failure depending on the vibrational amplitude.

Preface

Part of Chapter 6 in this thesis has been presented by H. Lu and M. van der Baan as "Simulation of dynamic triggering of acoustic emissions using a bonded-particle method" in 50th US Rock Mechanics/Geomechanics Symposium, ARMA Paper 2016-519. I was responsible for the model simulation and results analysis as well as manuscript composition. M. van der Baan was the supervisory author and contributed to designing guidelines and manuscript edits.

Acknowledgements

I wish to thank Dr. Mirko van der Baan for his enormous patience and guidance. His unique and intelligent way of seeing and presenting problems enlightens me on critical thinking and logical writing.

Special thanks go to my committee members: Dr. Claire Currie, Dr. Moritz Heimpel, Dr. Derek Martin. Their feedback is an important part of my work.

I would also like to thank all members in microseismic group for their friendship and discussions. Special thanks to Drew, Zhenhua, Himanshu, Fernando, Melanie, Jean Baptiste, Vicent for sharing me with their intelligence.

I would like to thank all sponsors of the Microseismic Industry Consortium and especially Itasca for providing licenses for the PFC software.

Finally, I would like to thank my parents for their love and support. Their saying of methods being more than difficulties provides me with courage and positive attitude towards life.

I am grateful for all your supports and encouragements.

Contents

List of Tables

List of Figures

Chapter 1

Introduction

1.1 Background

Hydraulic fracturing is a well stimulation technique applied in unconventional tight reservoirs. It breaks down rocks by injecting pressurized fluids and creates fractures and fissures as connected pathways for hydrocarbon migration up to the ground. Wellbore parameters, for example, borehole pressure, are monitored to offer direct information about fracturing effectiveness. Besides, microseismicity, originating from the fracturing process, is used as an indirect method to monitor the development of hydraulic fractures. Microseismic monitoring has become a routine application over the past decade. Microseismic signals generated by the instantaneous underground deformation are recorded and processed to map microseismic sources (Maxwell, 2011). This continuous recording delivers diagnostic information in terms of location, geometry and evolution of the resulting fractures, as well as additional geologic information on the reservoir. Recently, progress in real-time microseismic processing allows operators to react in real time with fracture control to improve stimulation coverage and avoid potential geohazards (Le Calvez et al., 2007).

Microseismic mapping has been proven a success in evaluating hydraulic fracturing treatments (Cipolla et al., 2005; Wolhart et al., 2006; Warpinski et

al., 2013). Nonetheless, several interesting field observations raise a number of questions. The input energy, calculated by the pressure and injection rate is found to be nine orders of magnitude larger than the output energy calculated based on microseismic measurement (Maxwell et al., 2008). Spatially speaking, some microseismic events are observed above and below a large fracture, challenging the assumption in hydraulic fracturing interpretations that microseismicity is indicative of the fluid fronts (Johnson et al., 2014). As a result, microseismic studies have turned from localization methods to source mechanism determinations. Restricted by the quantity and quality of microseismic recordings and the limited coverage of geophones, geomechanical modeling is employed as an important tool to simulate the fracturing process and test hypotheses beneath observations. Chorney et al. (2014) simulate triaxial tests to study energy budget associated with rock failure and they find the empirical Kanamori relation used in traditional seismology underestimates the failure energy for microseismic events. Johnson et al. (2014) incorporate flow and geomechanics in a fractured model at the field scale and validate the existence of dry microseismicity. Geomechanical modeling is a powerful tool potentially unveiling further details about the hydraulic fracturing process (Hazzard et al., 2002; Zhao and Young, 2009; Zhao et al., 2014; Garcia-Teijeiro and Rodriguez-Herrera, 2014). The objective of this thesis is to use geomechanical modeling to study the relationship between individual acoustic emissions during the fracturing deformation in a compression test. The study will benefit microseismic interpretation and operation strategy in terms of treatment effectiveness.

1.2 Dynamic earthquake triggering

An earthquake is a rapid process of energy release due to the relative movement along a locked fault. This permanent deformation alters the in-situ stresses in

the surrounding area and hence the stability of local faults. The quantification of the influence of the permanent stress on local faults, termed the Coulomb failure function (CFF) by seismologists, is extensively used to interpret earthquake clusters concentrated in a certain region or time frame after one major earthquake (Das and Scholz, 1981; King et al., 1994; Toda et al., 1998). CFF evaluates the slip potential of a fault experiencing loading. The correlation between positive changes in CFF (permanent stress pushing faults closer to failure) and the distribution of aftershocks implies a causal relationship between a major earthquake and the following ones. This is called static earthquake triggering.

Besides the permanent deformation, seismic wave propagation is another indispensable component during an earthquake. The theory of dynamic triggering due to seismic wave propagation is also important. The observation of unexpected seismicities at great distances (larger than a few fault lengths) challenges the theory of static triggering. The static stress change is not significant enough to trigger an earthquake at large distances. Seismic waves transfer a transient but relatively greater stress. The calculation of CFF using dynamic stresses offers a plausible candidate for remote seismicity occurrences (Pankow et al., 2004). Following the study of dynamic triggering in remote seismicity, the importance of dynamic triggering in local earthquake triggering is gradually recognized (Cotton and Coutant, 1997; Kilb et al., 2000). Pollitz and Johnston (2006) first test the relative importance of the static and dynamic triggering in near-field aftershocks. They compare aftershock patterns because of aseismic events, corresponding to the static stress influence, and ones generated by impulsive events, which are influenced by both static and dynamic stresses. They conclude that dynamic triggering is more dominant in causing near-field aftershocks.

Recently, the theory of a secondary mechanism initiated by dynamic wave propagations is established through laboratory work. Jia et al. (2011) add waves of different amplitudes during a uniaxial compression test on polydisperse glass beads and find that the sound-matter interaction weakens the medium by causing a decrease in elastic wave velocities. Johnson et al. (2008) and Ferdowsi et al. (2014) observe frictional weakening in sheared granular media due to wave propagation through laboratory experiments and numerical simulations respectively. The nonlinear behaviour of rocks in response to dynamic waves seems to play a indispensable role in earthquake triggering.

Seismic waves transfer a transient and dynamic stress and initiate a weakening mechanism, influencing earthquake occurrences. It is possible that microseismic events also interact with each other through the transient wave motion. This thesis aims to study dynamic triggering of acoustic emissions by simulating a compression test using the bonded-particle method. This examination of the fracturing process offers insight into microseismic event interpretations and stimulation strategies.

The objectives of this thesis include:

1. Computation of the analytic dynamic stress induced by an event and exploration of the subsequent failure patterns in order to evaluate the relationship between individual acoustic emissions from the perspective of dynamic stresses.

2. The addition of an external vibration during the compression test to study the influence of their amplitudes and dominant frequencies on failure patterns.

1.3 Thesis structure

The study is carried out in the next six chapters:

Chapter 2 reviews fundamentals of geomechanics necessary to readers. Separated into two parts, continuum mechanics and fracture mechanics, basic definitions and observations, viewing conventions, and common criterion are introduced.

In **Chapter 3**, different geomechanical modeling methods are first outlined. Then, the tool used in this thesis, bonded-particle method (BPM) and the software, Particle Flow Code (PFC) are introduced on how the discrete elements are manipulated to simulate a realistic behaviour of a specific material.

Chapter 4 examines the performance of BPM handling elastodynamics problems by comparing the displacement and stress fields due to a single force excitement with the corresponding analytic solutions. Wave propagation in BPM due to the model's discrete nature, scattering, dependence of wave velocity on frequencies are also discussed. Then dynamic triggering of acoustic emissions are studied by simulating a major event in the next two chapters.

Chapter 5 creates a major event by breaking bonds within several particles in the center of the rock model. The influence of dynamic stresses are studied in two methods. First, two modes of simulations, static and dynamic modes, are carried out to compare the static and dynamic influences directly. The second approach is similar to the calculation of CFF in seismology. The analytic stress pattern induced by the major event are compared with the occurrence

of the next few events to determine relationships between dynamic waves and following events.

To work in a more controllable way, **Chapter 6** follows work done by Ferdowsi et al. (2014) by adding an external vibration with specified amplitudes and frequencies to initiate failure by wave propagation. The influence of amplitude and frequency of dynamic waves are studied respectively.

Chapter 7 summarizes the contents of this thesis, and ends with discussions of further possible research.

Chapter 2

Geomechanics

Geomechanics is a theoretical and applied science concerned with the mechanical responses of geological materials. The two main disciplines are soil mechanics and rock mechanics, the latter of which is the subject of this work. The rock has complex mineral constituents due to its complicated genesis conditions. It undergoes perpetual changes after formation, especially the external loading due to tectonic movement. The rock will deform, and even fail. Also, the rock can be a porous medium filled with fluids in the voids. All these factors makes rock a Discontinuous, Anisotropic, Inhomogeneous and Not-Elastic (DIANE) material (Hudson and Harrison, 2000). This chapter describes the fundamentals of rock mechanics and it is divided into two parts, continuum and fracture mechanics.

2.1 Continuum mechanics

Continuum mechanics is concerned with stresses in a medium without gaps or severe deformation. Although it is an oversimplification of rock, concepts and mathematical functions in continuum mechanics offer a great aid in rock behaviour analysis. The stress tensor describes the stress states at any point mathematically. Alternatively, a Mohr's circle offers a graphical expression in

the rock deformation analysis. This section will start with the basic concepts mentioned above and then introduces general laws depicting rock behaviour.

2.1.1 Stress

Rocks are subjected to external loading since their formation. Different parts inside a rock undergo relative changes in position in response to the applied force. The force may vary both in orientation and magnitude with spatial position. So another concept, stress, is also used in geomechanical study.

Stress is a second-order tensor with nine components, depicting the forces acting on all surfaces passing through a given point:

$$\boldsymbol{\sigma} = \begin{bmatrix} \sigma_{11} & \sigma_{12} & \sigma_{13} \\ \sigma_{21} & \sigma_{22} & \sigma_{23} \\ \sigma_{31} & \sigma_{32} & \sigma_{33} \end{bmatrix}, \tag{2.1}$$

where σ_{ij} (i,j = 1,2,3) represent the components of the stress tensor $\boldsymbol{\sigma}$. The stress tensor is a combination of three vectors which are mutually orthogonal. Each row represents one vector, indicating the force applied on one of the three orthogonal planes. So the first subscript of these components are the same along each row. The second subscript represents the direction of force decomposition on each plane. The stress components can be easily illustrated in a block shown in Figure 2.1.

The stress tensor is a symmetric matrix. Its diagonal elements are normal stresses and the off-diagonal ones are shear stresses (Malvern, 1969). In linear algebra, a real symmetric matrix can be diagonalized (Bronson and Costa, 2008). In the case of the stress tensor, a set of orthogonal basis vectors exists to make the six shear components in a general stress tensor vanish. The axes are called principal axes and represent the principal plane directions. Then the

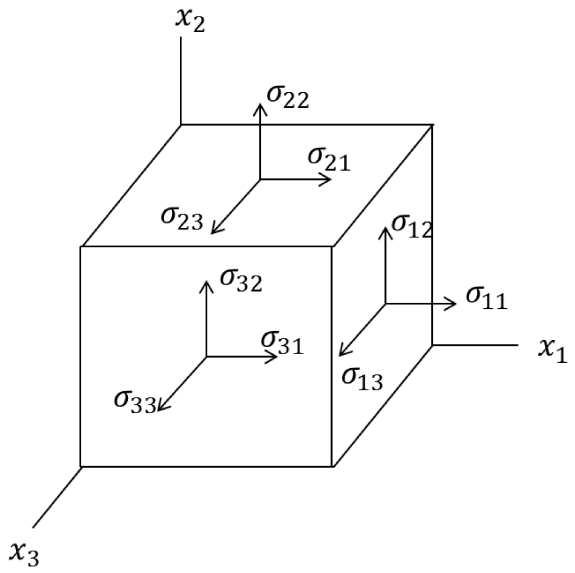

Figure 2.1: Stress components.

stress tensor becomes:

$$\begin{bmatrix} \sigma_1 & 0 & 0 \\ 0 & \sigma_2 & 0 \\ 0 & 0 & \sigma_3 \end{bmatrix}, \tag{2.2}$$

where σ_i (i=1,2,3) is the principal stress. In this case, the three normal stresses σ_i suffice to represent the stress state in the system of principal axes. For their simplicity in representation and analysis, principal axes and principal stresses are much used.

Two-dimensional Mohr's circle

Forces on an arbitrary plane can be easily expressed by the stress tensor:

$$\boldsymbol{t} = \boldsymbol{n} \cdot \boldsymbol{\sigma}, \tag{2.3}$$

where $\boldsymbol{n}$ represents the unit normal of the plane. Force $\boldsymbol{t}$ is also called traction.

The traction $\boldsymbol{t}$ can be projected into the normal and shear directions, with values equal to σ and τ respectively (Figure 2.2a). This algebraic expression can be represented graphically in a Mohr diagram, presented by Mohr in 1914 (Parry, 1995). Mohr circles offer a qualitative and quantitative way to express the stress states graphically. For example, principal stresses are given by the points where circles cross the axis is shown in Figure 2.2b.

The introduction of the Mohr circle is based on principal axes where only principal stress σ_i is needed to depict the stress state. In two dimensions, suppose the principal stresses are σ_1 and σ_2 ($\sigma_1 \geq \sigma_2$). Next consider a plane whose unit normal direction is rotated counterclockwise by angle θ from the maximum principal stress (Figure 2.2a) and compute the traction acting on this plane. This gives the resolved normal and shear components:

$$\begin{aligned} \sigma &= \frac{\sigma_1 + \sigma_2}{2} + \frac{\sigma_1 - \sigma_2}{2}\cos 2\theta, \\ \tau &= -\frac{\sigma_1 - \sigma_2}{2}\sin 2\theta. \end{aligned} \tag{2.4}$$

Equation 2.4 represents a circle in the (σ , τ) plane (Figure 2.2b). If the minus sign in the shear stress is absorbed into $\sin(-2\theta)$, and $\cos(2\theta)$ in the normal stress is interpreted as $\cos(-2\theta)$, then a circle can be expected at the locus of the end of a vector with length $(\sigma_1 - \sigma_2)$ fixed at the center point $(\frac{\sigma_1+\sigma_2}{2}, 0)$ rotating clockwise around the center (Figure 2.2b). This circle is called Mohr's circle. The circle represents the stress states of planes orientated in all directions. It intersects with the σ axis at two points, with the abscissa equal to the principal stresses, σ_1 and σ_2. Mohr's circle can be used to calculate normal and shear stress at any plane. Though the calculation capacity of modern computers is more appealing, the graphic representation gives a more intuitive knowledge of the stress state especially in failure analysis.

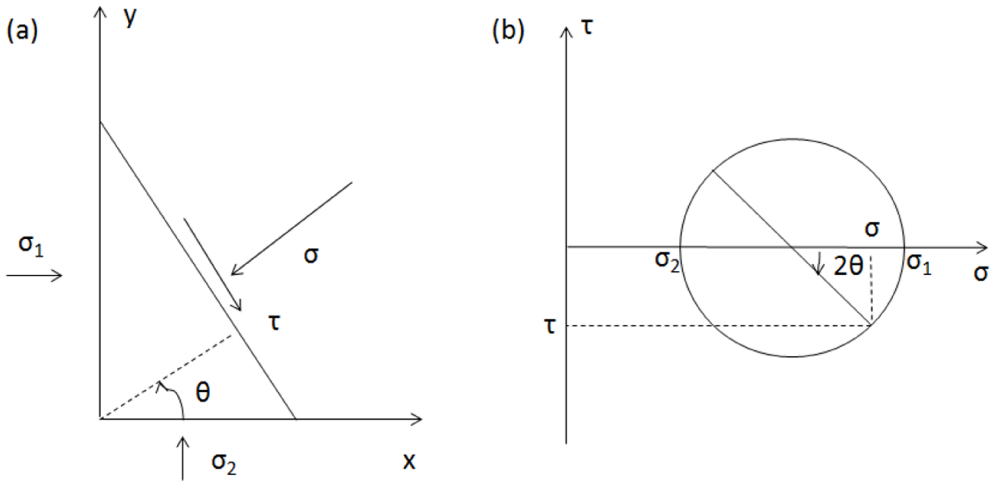

Figure 2.2: a. With principal stresses σ_1 and σ_2 , the traction on the surface with normal vector rotating an angle of θ from the maximum principal stress direction is resolved to normal and tangential direction with values σ and τ. b. Mohr circle of principal stresses equal to σ_1 and σ_2.

Three-dimensional Mohr's circle

Similarly, the three-dimensional Mohr circle can be constructed when considering the stress in three dimensions. The coordinate transformation is almost identical to the 2D case. Again, the coordinate system is constructed along the principal axes. Principal stresses are σ_1, σ_2 and σ_3 ($\sigma_1 \geq \sigma_2 \geq \sigma_3$). Then the normal and shear stresses on the plane are:

$$\begin{aligned} \sigma &= l^2\sigma_1 + m^2\sigma_2 + n^2\sigma_3, \\ \tau^2 &= l^2\sigma_1^2 + m^2\sigma_2^2 + n^2\sigma_3^2 - \sigma^2, \end{aligned} \tag{2.5}$$

l, m, n are the cosines of the angles between the normal vector and the three axes in a rectangular coordinate system. The endpoints of normal vectors of all the planes in different orientations will shape a sphere in the coordinate system. Then if one of the three direction cosine is fixed, the collection of the normal vectors will form a circle intersecting with the unit sphere. And the normal and shear components, σ and τ, on the plane will satisfy a circle equation in

the σ - τ plane. Take the fixed direction cosine n for example,

$$\tau^2 + [\sigma - \frac{1}{2}(\sigma_1 + \sigma_2)]^2 = \frac{1}{4}(\sigma_1 - \sigma_2) + n^2(\sigma_1 - \sigma_3)(\sigma_2 - \sigma_3). \tag{2.6}$$

This is a circle centered at $(\frac{1}{2}(\sigma_1 + \sigma_2), 0)$ with radius r equal to $\sqrt{\frac{1}{4}(\sigma_1 - \sigma_2) + n^2(\sigma_1 - \sigma_3)(\sigma_2 - \sigma_3)}$.

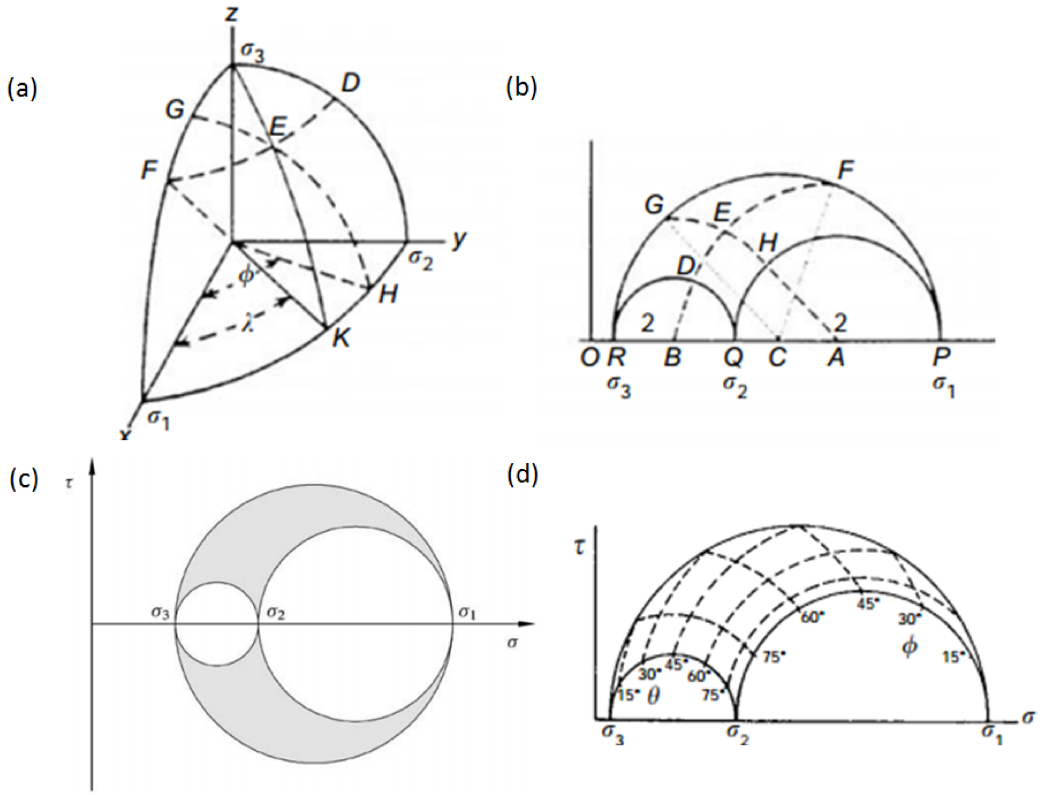

Figure 2.3: Mohr's circle in three dimensions, see text for description (Jaeger et al., 2009).

Stress states on any orientation plane can be expressed on the σ - τ plane in this way. For an arbitrary normal vector, it will cross with the unit sphere in a point. For instance, consider point E in Figure 2.3a. It is the crossing point of two unit circles in the rectangular coordinate system (arc DEF and GEH in Figure 2.3a). The position in the σ - τ plane can then be located by the two corresponding circles with different centers and radii (arc DEF and GEH

in Figure 2.3b).

So the stress states on a plane of any orientation are represented by the shaded area in Figure 2.3c, an area bounded by three Mohr circles with diameters given by the differences between any two principal stresses. Figure 2.3d is a sketch showing the angles of the normal vector with the three principal stresses in a Mohr diagram.

Underground stress states

The orientation of the principal stresses must satisfy the boundary condition at the surface of the Earth where there is a nearly zero normal stress and no shear (Hubbert and Willis, 1957). Therefore, here, one principal stress is perpendicular to the surface, and the other two are surface parallel. Then the three principal stresses can be expressed as σ_V, σ_H and σ_h (with $\sigma_H \geq \sigma_h$). The vertical stress is approximately equal to the overburden pressure and increases with depth, yielding,

$$\sigma_V = \int_0^z \rho(z) g dz \approx \rho_a g z, \tag{2.7}$$

where ρ_a is the average bulk density of the rock, and z is the target depth.

As for the horizontal stresses, they are controlled by lithology and tectonic forces. In practice, it is observed that at shallow depths the minimum principal stress is the vertical stress because of weaker cementation and compaction at shallower depth as well as a reduced overburden weight. The minimum principal stress often becomes a horizontal one at some depth depending on the regional regime. There are three patterns of the relative stress magnitudes shown in Table-2.1. The stress pattern determines the relative motion of rocks, hence promoting a certain type of faulting (Anderson, 1951).

In some areas of tectonic activity, the principal stress may be tilted from the

Type	σ_1	σ_2	σ_3
Normal faulting	σ_V	σ_H	σ_h
Reverse faulting	σ_H	σ_h	σ_V
Strike-slip faulting	σ_H	σ_V	σ_h

Table 2.1: Anderson's classification of faulting regime and the corresponding relative stress magnitudes.

horizontal/vertical direction.

2.1.2 Strain

Upon loading, rocks can change in position as well as in shape (Figure 2.4). Due to their deformability, different parts inside rocks may undergo nonuniform displacements. Similar to stress, a tensor-form variable, strain, is used to give a quantitative measure of the deformation:

$$\boldsymbol{\epsilon} = \begin{bmatrix} \epsilon_{11} & \epsilon_{12} & \epsilon_{13} \\ \epsilon_{21} & \epsilon_{22} & \epsilon_{23} \\ \epsilon_{31} & \epsilon_{32} & \epsilon_{33} \end{bmatrix}, \tag{2.8}$$

where ϵ_{ij} (i,j = 1,2,3) represent the components of the strain tensor $\boldsymbol{\epsilon}$.

Strain results if relative change in position between neighbouring parts happens. However, not all relative displacement results in strain, e.g., rotation (Figure 2.4b). The strain tensor can be expressed in terms of relative displacement when the displacements of the material particles are assumed to be much smaller than the dimension of the body (small-strain theory):

$$\epsilon_{ij} = \frac{1}{2}(\frac{\partial u_i}{\partial x_j} + \frac{\partial u_j}{\partial x_i}), \tag{2.9}$$

where u_i (i=1,2,3) is the relative displacement. The relationship between strain ϵ_{ij} and relative displacement u_i is called the geometric equation. The strain tensor is also symmetric.

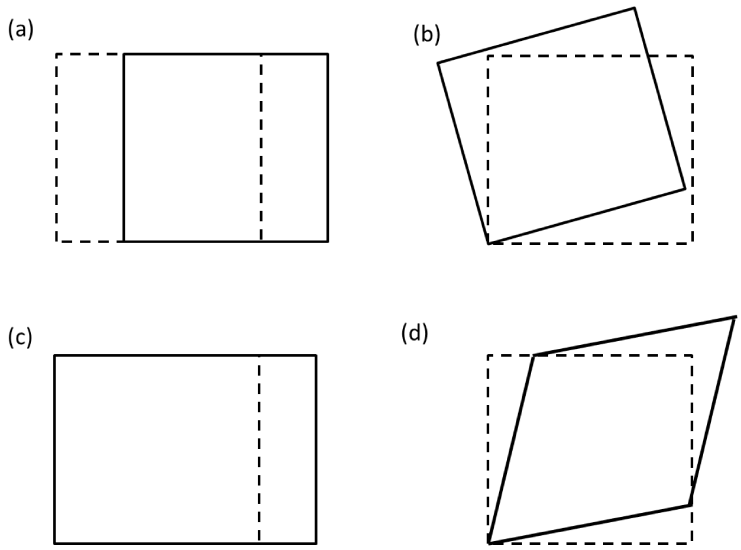

Figure 2.4: Spatial changes of rocks in response to applied force: a. translational displacement; b. rotation; and exemplary deformation changes in two dimensions: c. pure normal strain in the form of uniaxial extension and d. pure shear strain without rotation (dash and solid lines denote the states before and after force application respectively).

Normal strain results in either a decrease or increase (Figure 2.4c) in length along the uniaxial direction. Pure shear strain quantifies the decrease in the right angle set up by two orthogonal sides (Figure 2.4d). Following Equation 2.9, the normal strain along the i-th direction can be expressed as:

$$\epsilon_i = \frac{\partial u_i}{\partial x_i}. \tag{2.10}$$

And the shear strain ϵ_{ij} is acting along the j-th direction on the plane perpendicular to x_i axis and expressed as:

$$\epsilon_{ij} = \frac{1}{2}(\frac{\partial u_i}{\partial x_j} + \frac{\partial u_j}{\partial x_i}). \tag{2.11}$$

The strain tensor has the same definitions of principal axes and principal strains. However, the principal axes of strain are always inconsistent with those of stress. In practice, the geometry is based on the principal axes of stress.

2.1.3 Constitutive relations

Rocks deform if a load is applied. Figure 2.5a shows a sketch of stress-strain curve for a rock under uniaxial compression. Stress increases nearly linearly with strain until point B, starting from which the stress-strain slope begins to decrease. The rise of stress terminates at point C with a stress value equal to C_0 known as the uniaxial compressive strength (UCS). In region CD, the rock cannot sustain any more stress shown as the decline of the curve, implying failure. The exact rock behaviour is decided by the internal constitution (Malvern, 1969). So the mathematical equation describing the reaction in terms of a stress-strain relationship is called constitutive equation. Rocks behaviour can be quite diverse subject to a range of external conditions including confining pressure, loading strategy, temperature, etc. For example, rock will creep under long-term constant confining stress (Lockner, 1993) and fail at a different stress. Because of this complex behaviour, only the ideal elastic case (Figure 2.5b), is introduced mathematically. Other cases including plasticity, viscoelasticity and viscoplasticity will only be mentioned briefly.

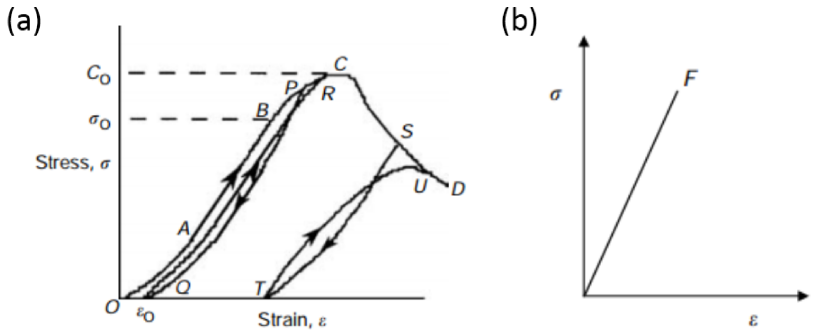

Figure 2.5: a. Sketch of stress-strain curve for a rock under uniaxial compression showing elastic, plastic behaviour and failure, and different loading-unloading paths. b. Ideal case of stress-strain curve for a rock displaying linear elastic behaviour (Jaeger et al., 2009).

Linear elastic theory

In classic elasticity, stress and strain has a one to one correspondence and stress depends linearly on strain. In one dimension, for example, external compression at the two ends of a bar causes shortening. The relationship between the applied loading and the material deformation obeys Hooke's law stating that the force F needed to attain a certain displacement x of a spring is proportional to the distance, $F = kx$. It is a simple linear relation. The proportionality coefficient k characterizes the spring's elastic property and is called stiffness. For rocks, moduli are used to describe the elasticity. The Young's modulus E describes the tendency to deform subject to opposing forces along one axis (Figure 2.4c). The shear modulus μ describes an object's tendency to shear (Figure 2.4d) when acted upon by opposing forces. In a more realistic situation, the opposing force along one axis not only causes shortening along that direction, it also leads to expansion in the perpendicular directions. The parameter ν, called Poisson's ratio, is defined as the ratio between the transverse expansion and the axial compression. These parameters are commonly measured and used in geomechanical studies. Under triaxial loading, the linear dependence between stress and strain is more complex:

$$\sigma_{ij} = c_{ijpq}\epsilon_{pq}, \tag{2.12}$$

where c_{ijpq} $(i, j, p, q$=1,2,3) is a fourth-order tensor, called the stiffness tensor. As Equation 2.12 has a similar form to Hooke's law, it is called the generalized Hooke's law. Generally, a fourth-order tensor has 81 components. The stiffness tensor decreases to 36 independent coefficients due to the symmetry of the stress and strain tensors. If the material is isotropic, having no preference in elastic properties along any orientation, the fourth-order tensor can be uniquely expressed by only two parameters:

$$c_{ijpq} = \lambda\delta_{ij}\delta_{pq} + \mu(\delta_{ip}\delta_{jq} + \delta_{iq}\delta_{jp}), \tag{2.13}$$

where λ is Lamé's first parameter. This parameter and the shear modulus μ, also called Lamé's second parameter, characterizing the elasticity of the material. λ can be expressed using the Young's modulus E and shear modulus μ by:

$$\lambda = \frac{\mu(E - 2\mu)}{3\mu - E}. \tag{2.14}$$

Inserting Equation 2.13 into Equation 2.12, the generalized Hooke's law in an isotropic medium is:

$$\sigma_{ij} = \lambda\epsilon_{kk}\delta_{ij} + 2\mu\epsilon_{ij}. \tag{2.15}$$

Other constitutive relationships

Rock behaviour is much more complex than elastic theory predicts. In Figure 2.5a, immediately beyond the elastic range OB with a steep stress-strain slope, a decreased slope occurs. The transition point B is called yield point as irreversible deformation starts to form after this point. The rock enters the plastic domain. The loading-unloading curve O-A-B-P-Q illustrates a permanent deformation ϵ_0. Figure 2.5a shows stress continues to increase with strain after the yield point. It means the rock still supports the load without gross fracturing. This phenomenon is called ductile behaviour, which is common in carbonates and some sediments.

Rocks may also depend on strain rate, instead of purely strain alone. Rocks resist deformation with time upon loading. Rocks then show viscoelastic and viscoplastic features.

2.1.4 Governing laws

The governing law in geomechanics is the equation of motion. The mechanical model of rocks can be constructed, together with the constitutive equations depicting stress-strain relationships.

According to Newton's law of motion, the net force F equals the product of the acceleration a and mass m:

$$F = ma. \tag{2.16}$$

In continuum mechanics, this equation is applied to an arbitrary object. A random unit of mass occupying the volume V and bounded by the surface S (Figure 2.6) is considered here. The net force of the mass is the sum of the external body forces acting on the volume and surface forces applied to the surface. The equation of motion becomes:

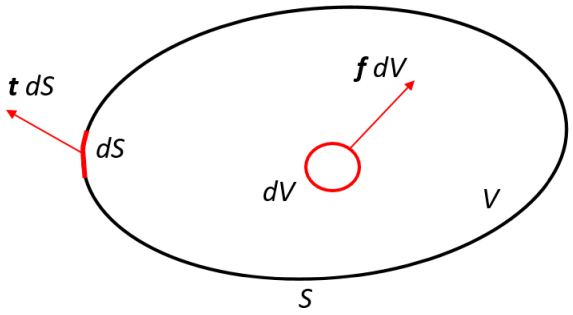

Figure 2.6: Sketch of a unit mass used for motion equation derivation.

$$\oint_S \boldsymbol{n} \cdot \boldsymbol{\sigma}\, dS + \iiint_V \boldsymbol{f^b}\, dV = \iiint_V \rho \ddot{\boldsymbol{u}}\, dV \tag{2.17}$$

where ρ is the mass density, $\boldsymbol{f^b}$ is the body force, $\ddot{\boldsymbol{u}}$ is the second derivative of the displacement $\boldsymbol{u}$ with respect to time. Using the divergence theorem, the

surface integral can be absorbed into the volume integral, that is:

$$\iiint_V (\bigtriangledown \cdot \boldsymbol{\sigma} + \boldsymbol{f^b})\, dV = \iiint_V \rho \ddot{\boldsymbol{u}}\, dV, \tag{2.18}$$

where $\bigtriangledown$ represents the divergence operator. Due to the arbitrary choice of the volume V, the integral can be discarded and the final expression is:

$$\bigtriangledown \cdot \boldsymbol{\sigma} + \boldsymbol{f^b} = \rho \ddot{\boldsymbol{u}}. \tag{2.19}$$

This equation governs the dynamic problem at any point in the continuum. In a homogeneous, unbounded, isotropic and elastic medium, Equation 2.19 becomes as follows by incorporating the constitutive relationship (Equation 2.15):

$$\rho \ddot{u}_i = f_i^b + (\lambda + \mu) u_{j,ji} + \mu u_{i,jj}, \tag{2.20}$$

where the vectors, force and displacement, are expressed in the indicial notations as f_i^b and u_i (i = 1,2,3). The comma in the subscripts denotes partial derivatives with respect to space. Repeating indices implies the use of the summation convention which states that the repeating letter should be given all possible values and the results added together.

The governing equation can be used to set up a geomechanical model and compute the stress distribution with the proper boundary and initial conditions. This is the basis of the analyses in the following chapters.

2.2 Fracture mechanics

Underground rocks are subject to external loading including overburden stress, tectonic forces, etc. Rocks fail if the applied stress reaches a certain limit, lead-

ing to permanent deformation. This characteristic limit is called rock strength. Compressive strength is generally assessed with laboratory tests, including uniaxial, triaxial and true-triaxial or polyaxial tests. The most common test is an axial compression test on a circular cylinder specimen. If confining pressure is zero, it is called a uniaxial test and the stress at which rock fails is termed unconfined compressive strength (UCS). When the confining pressure is not zero, the experiment is generally called a triaxial test, even though the radial stress is homogeneous. The strength generally increases with the confining pressure. A true triaxial or plolyaxial test simulates the more general underground states where three principal stresses are different.

Tensile failure is an alternative to compressional failure. Tensile strength can also be attained in the laboratory by a Brazilian test.

2.2.1 Compression failure

The failure of rocks in compression is a complex process that involves microscopic failures manifested as the creation of small tensile cracks and frictional sliding on grain boundaries and cracks (Brace et al., 1966). Eventually, a shear plane is formed through coalescence of these microscopic failures (Lockner et al., 1991).

Mohr–Coulomb failure criterion

The Mohr-Coulomb failure envelope is an experimentally determined failure condition. A series of triaxial tests defines an empirical Mohr-Coulomb failure envelope. One plots the Mohr circles when failure occurs at different combinations of principal stresses. The curve enveloping all the stress state points on different circles is the Mohr-Coulomb failure envelope (Figure 2.7b). The Mohr circle represents the stress states (the normal and shear stress) on planes of any orientation. Points below the envelope are stable without possibility of

failure; whereas points on the curve will fail and those above the envelope are not supposed to exist.

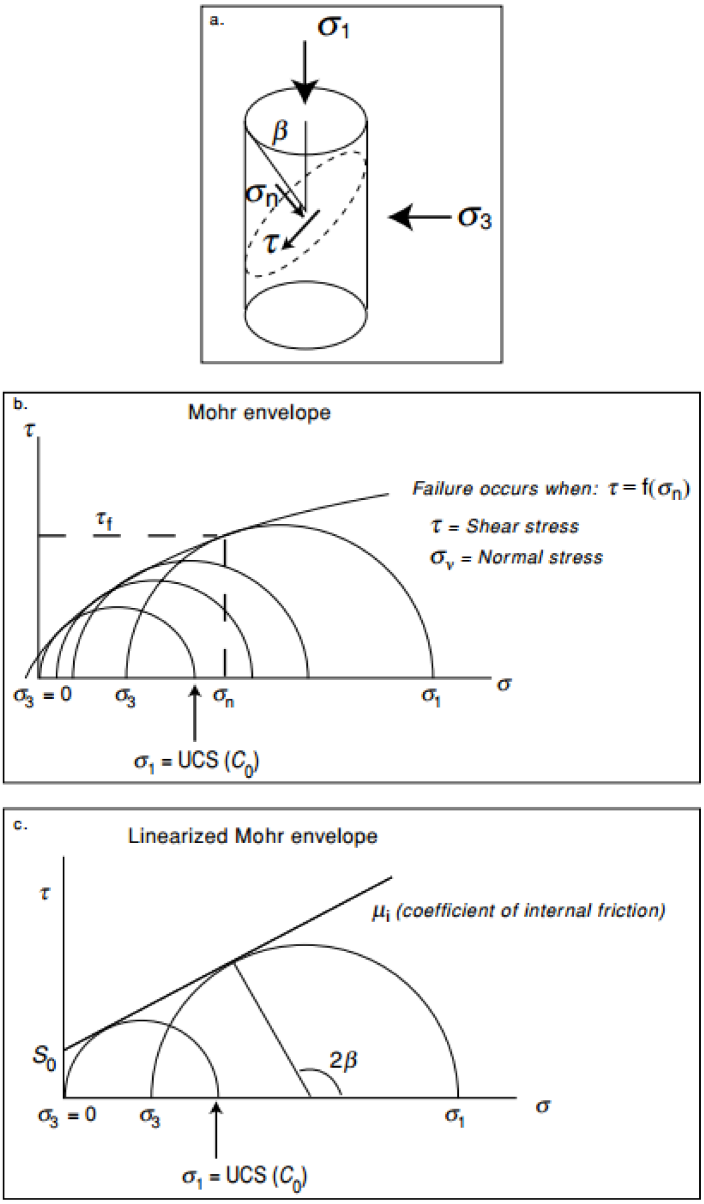

Figure 2.7: a. Shear failure under compression. b. Mohr envelope determined by experiments. c. Linearized Mohr envelope (Zoback, 2010).

Linearized theory of Mohr–Coulomb failure criterion

A linearized simplification is usually used in reality (Figure 2.7c). Amonton's law of friction states that two contacting bodies over an inclined surface must overcome a shearing force T related to the normal force N and the friction coefficient μ_i to slip, $T = \mu_i N$. Similarly, the shear component of the traction along the plane τ, needed to overcome the friction, is proportional to the applied load σ. Sliding will occur as soon as the shear stress overcomes the friction. But different from Amonton's law, an inherent cohesive force exists in the process. That is, even when the normal load is zero, sliding will not occur unless the value of shear stress exceeds this inherent threshold. Then the linearized theory can be defined by two parameters: (1) the slope of the failure line μ_i, termed as the coefficient of internal friction, where the subscript in μ_i is used to distinguish from the shear modulus μ; and (2) the inherent force S_0, which is called the cohesive strength (or cohesion), that is,

$$\tau = S_0 + \sigma\mu_i. \tag{2.21}$$

Figure 2.8 shows the stress states (principal stresses S_1 and S_3) of failure derived in a series of triaxial tests under different confining stresses in laboratory. It shows the linearized Mohr-Coulomb criterion in the $\sigma_1 - \sigma_3$ plane, which can also be derived analytically by replacing σ, τ in Equation 2.21 with σ_1 and σ_3 using Equation 2.4.

2.2.2 Tensile failure

When tensile stress is applied and exceeds a critical limit, the rock will fail in tension. The subjected tensile stress equals then the rock tensile strength, T_0. The tensile strength for all rocks is quite low compared with their compressive strength. A purely tensile stress is quite rare underground especially below a certain depth where stresses are generally compressive.

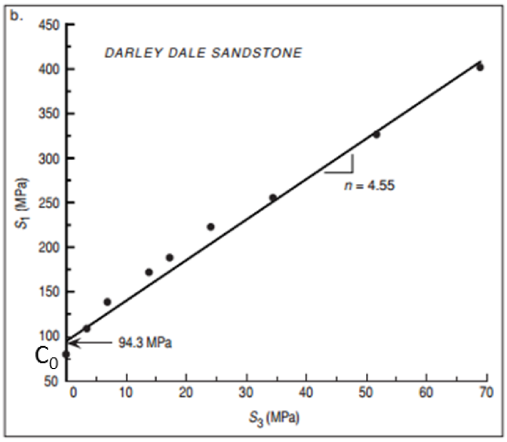

Figure 2.8: The linearized Mohr-Coulomb criterion shown in the $\sigma_1 - \sigma_3$ plane (Zoback, 2010).

The failure criterion for tensile failure is when the stress σ reaches the tensile strength, that is,

$$\sigma = -T_0. \tag{2.22}$$

Combined with the linearized Mohr-Coulomb criterion, a bilinear failure criterion can be used under tensile and compressive loads (shown in Figure 2.9). Figure 2.9 shows the failure curve in (σ_3,σ_1) plane instead of σ-τ plot (Figure 2.8). The inclined line is responsible for failure in compressional loading. The vertical portion represents the tensile failure. Rock fails in tensile mode when the minimal principal stress σ_3 is tensile and exceeds the tensile strength T_0.

2.2.3 Griffith theory of failure

Even though the Mohr-Coulomb criterion is widely used, it is not perfect (Jaeger et al., 2009). First, the ratio of uniaxial compressive and tensile strength, C_0/T_0 predicted by the bilinear Mohr-Coulomb is much less than experimentally derived values. Second, compressive strength (the value of σ_1 when at failure) increases linearly with confining stress as shown in Figure 2.8, while experiments show it increases at a less-than-linear rate.

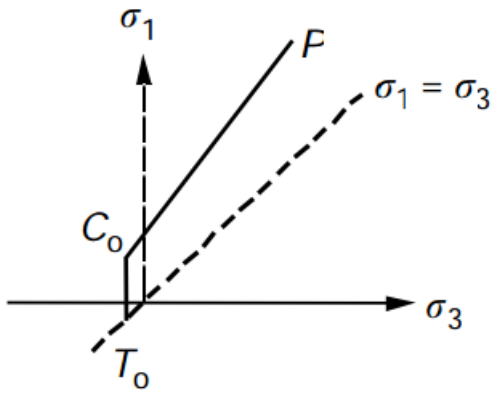

Figure 2.9: Bilinear failure criterion used in both tensile and compressive loads (Jaeger et al., 2009).

So apart from these empirical laws, much effort has been made in developing criteria from physical models of the deformation in fracture processes. Based on the fundamental concept of surface tension, Griffith (1924) created a new theoretical framework to calculate strength. He assumed the sum of surface tension energy of the crack, potential energy of the applied forces and strain energy of the specimen stays constant during the crack development. Griffith dealt with a two-dimensional problem, the stress in a plate pierced by a small thin elliptic crack. Following Inglis' solution to this general question (Inglis, 1913), he calculated the tangential stress along the boundary of the crack. According to the theory that a crack will extend when the maximum tensile stress reaches some value characteristic for the rock, the maximum tangential stress and the corresponding crack orientation were derived.

The ratio of uniaxial compressive strength and uniaxial tensile strength, C_0/T_0 is 8 from Griffith's theory. This is larger than the prediction of Coulomb theory (less than 5.83) but still lower than commonly observed in most rocks (on the order of 10); yet it is a reasonable result (Jaeger et al., 2009).

Applying Griffith's criterion to the Mohr space, the resulting Mohr envelope can be written as:

$$\tau^2 = 4T_0(\sigma + T_0). \tag{2.23}$$

This nonlinear failure curve in Mohr space, shown in Figure 2.10a, is more realistic than the linear Coulomb law, and can be applied under tensile and compressive loads.

Although Griffith's theory gives a general form satisfying the observed be-

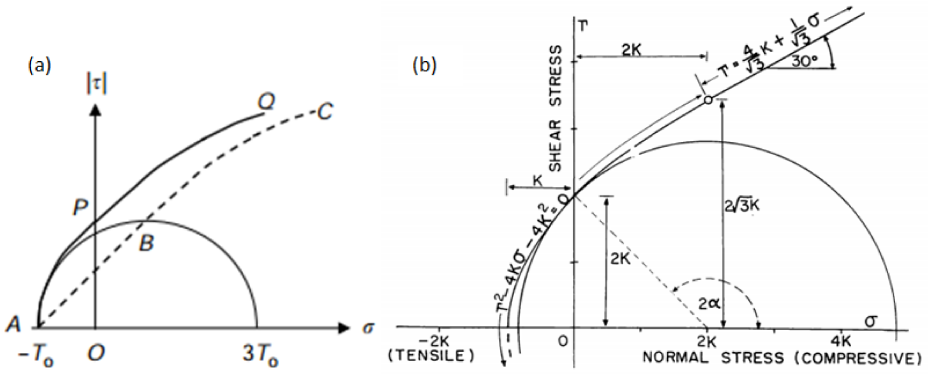

Figure 2.10: a. Griffith theory and b. its revised version (Jaeger et al., 2009; Secor, 1965).

haviour of rock specimens, it does not provide a good model for it ignores frictional forces on closed cracks. The effect of frictional forces along cracks in compression leads to a straight line in the failure envelope (Hubbert and William, 1959; Secor, 1965). Thus, the envelope becomes the composite of a parabolic curve and a straight line. The transition point can be determined by imposing continuity in slope. The straight part is experimentally determined with a slope of 30°. The composite failure envelope is shown in Figure 2.10b.

The fundamentals introduced in this chapter only concern the characteristics associated with dry rocks. The existence of fluids in rock voids and its influence on rock behaviour, e.g., increasing pore pressure leads to faster rock failure (Secor, 1965), are beyond the scope of this thesis.

Chapter 3

Geomechanical modeling

Different methods have been used to study the mechanical behaviour of rocks and they can be analytical (Deresiewicz, 1958; Marketos and O'sullivan, 2013), physical (Jia et al., 2011) or numerical (Cundall and Strack, 1979). All these three methods can show mechanical characteristics to some extent. Besides, they can provide an alternative test to validate each other. Numerical modeling is insightful due to its repeatability and possibly continuous information stream. However, observations from numerical tests should be taken with caution.

3.1 Numerical modeling of rocks

Numerical methods can be subdivided into two categories:

- Continuum approaches
- Discontinuum approaches

These two methods are classified by the treatment of the problem domain (Jing, 2003). A model 'qualifies' for being continuous only when subdivided into infinite number of components with the assumption of an infinitesimal element. A model can be seen as discrete if it is represented by a finite number of well-defined components/elements. In terms of damage representation, the continuum method is called an indirect model as the damage is addition-

ally supplemented; the discontinuum method is a direct modeling approach as damage is the result of formation of microcracks (Potyondy and Cundall, 2004). Following different methodologies, the governing equations and constitutive relations are adaptively formulated.

3.1.1 Continuum approaches

In continuum models, as the assumption of infinitesimal elements made, the equation of motion is represented at local points by a partial differential equation (PDE) (Equation 2.18) which is then replaced by an assembly of algebraic equations by different numerical methods.

The finite difference method (FDM) directly approximates the partial derivatives by differences. The problem domain in FDM is generally discretized into a regular rectangular grid of nodes (Figure 3.1). A truncated Taylor series is used for system variables like displacement. The partial derivatives in the governing PDE can be represented by the remaining polynomials. Then the unknowns at each point can be solved by the values at its surrounding nodes. Using this treatment, combined with boundary values, the unknowns at nodes in the whole domain can be calculated.

The finite element method (FEM) is one of the most popular numerical methods (Strang and Fix, 1973). Instead of directly solving the partial derivatives in the PDE, an integral is solved instead by summation and the PDE becomes a global algebraic system of equations in matrix form. The integral is a multiplication of the partial derivative and a polynomial (Figure 3.1b). The polynomial is called the shape function. A triangular element is often used in the discretization and hence FEM is more applicable in handling rock inhomogeneity and anisotropy. Also, the efficiency of FEM makes it a powerful

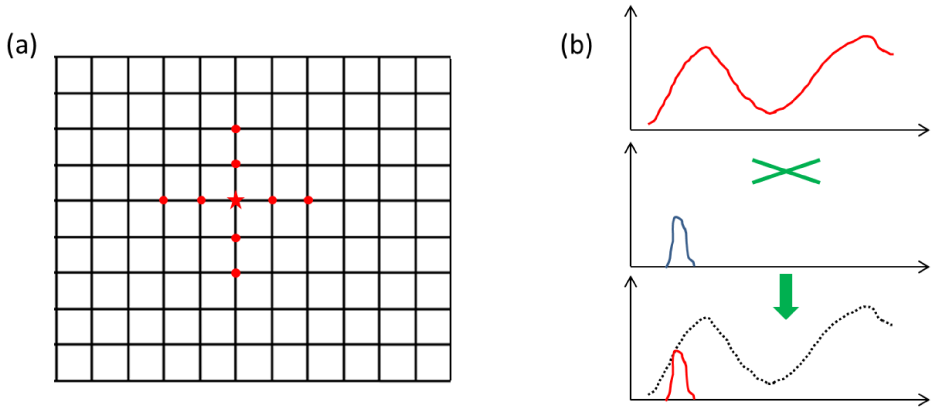

Figure 3.1: Sketch of numerical methods: (a) FDM, a second-order difference scheme, the unknowns at the red star are calculated by eight known values at its surrounding nodes, two along four directions (red dots) and (b) FEM, showing the conversion from a partial derivative to an integral.

numerical tool.

3.1.2 Discontinuum approaches

Continuum approaches are powerful tools. However, these methods inevitably suffer from the representation of the intrinsic discontinuities and their influence on rock behaviours. A general constitutive law for discontinuities is hard to derive. Therefore, the discontinuum method is developed. It models the material as an assembly of independent bodies with intrinsic discontinuities. The model behaviour is the result of the interaction of these well-defined bodies. Each body in a discontinuum method has its own properties. The constant recognition and updating of contacts developing at two contacting bodies gives a resultant force on each body. Direct application of the motion equation (Equation 2.16) on each body determines the global deformation of the system. As the bodies in discontinuum methods are independent, there is no displacement compatibility requirement. Bodies can rotate and/or detach to represent failure

in rocks directly. The continuous modeling method is often used to describe mechanical behaviour in engineering scenarios, whereas discontinuous modeling is generally used to study the mechanics governing rocks' behaviour (Potyondy and Cundall, 2004).

The modelling method used in this thesis is called the bonded-particle method (BPM) (Cundall and Strack, 1979). Modeling is performed by a commercial modeling software, the particle flow code (Itasca, 2008). BPM is a subset of the discrete element method (DEM) as bonding of two particles together is allowed. The details of how BPM is constructed and formulated will be introduced in the next section.

3.2 Particle flow code (PFC)

The particle flow code (PFC) is a simplified implementation of the discrete element method (DEM) as the components in the model, particles, are rigid bodies which cannot deform. It models a real material as an assembly of particles. The particles inside the model interact at the contacts connecting two bodies and hence the model evolves upon the prescribed conditions to simulate real-world behaviour of a certain material. Details on the model and its rationale are introduced in this section.

3.2.1 Model setup

The model generated in PFC has three basic components: particles, contacts and walls. Particles make up the main body of the model. Contacts become active when two particles come into contact (overlap), and together with particles, they define the mechanical behaviour of the model. Walls are artificial

interfaces used to apply external conditions to stimulate a certain response upon request.

Particles

The shapes of particles in PFC are not arbitrary. They are circular disks with unit thickness in 2D models or spheres in three-dimensional simulations. So particles are often referred as balls in PFC. However, it is also possible to simulate an irregular-shape particle by assembling several uniform particles together as a unit, called clump. It is worth noting that the type of particle in PFC is not necessarily equivalent to the unit of the real material, for example, grain in the rock. Particle sizes in PFC can be diverse. It can range from millimeters in rock core modeling (Chorney et al., 2012) to several meters when simulating a field scale case (Yoon et al., 2014). Naturally, smaller particles can more closely approximate the heterogeneity of real rocks and this gives a better representation of micromechanical behaviour. However, for the same size model, smaller particles mean larger quantities and hence more expensive computations. Therefore the determination of particle size should be duly considered. Apart from particle-size parameters, a particle is characterized by microproperties listed in Table 3.1. The particle is an elastic object resisting loads in the normal and shear directions. Because of the difference between particles and grains, particle properties cannot be directly assigned laboratory values. For example, the determination of particle density in a PFC model needs to take porosity ϕ into consideration:

$$\begin{aligned} \phi &= \frac{\sum_{i=1}^{n} V_i}{\rho V}, \\ \rho_P &= \frac{\rho}{\phi}, \end{aligned} \tag{3.1}$$

where V_i is the volume taken by each particle of the model comprising of n particles with volume equal to V. ρ_P is the particle density and ρ is rock density.

Symbol	Parameter
ρ	Ball density
E_c	Modulus, $k_n = 2E_c$
k_n/k_s	Stiffness ratio
μ	Friction coefficient

Table 3.1: Microproperties of particles in a PFC model.

Contacts

As particles in PFC are rigid objects absent of deformation, the interaction between particles needs a specific treatment. The method used in PFC is called soft contact approach which is widely used in discrete element simulations. Two particles overlap each other after they get into contact and interaction between particles begins. The interaction between two contacting particles has three basic modes: compressed, slip and tearing apart. Parameterized in PFC, the interaction is described by three microparameters associated with contacts: stiffness, maximum shear contact force and bond strength. These three parameters can describe any potential relative motion between two particles.

Contacts have two forms according to the contacting entities: ball-ball and ball-wall contact. Figure 3.2a shows the geometry of two interacting particles A and B. x_i denotes the location, and superscripts identify particles A and B and contact C. Other geometric information includes particle radius $R^{[A/B]}$, the distance between two particles d, overlap U^n and the unit normal of the contact plane n_i. The contact plane is the plane going through the contact point and perpendicular to the line connecting the centers of two particles. A

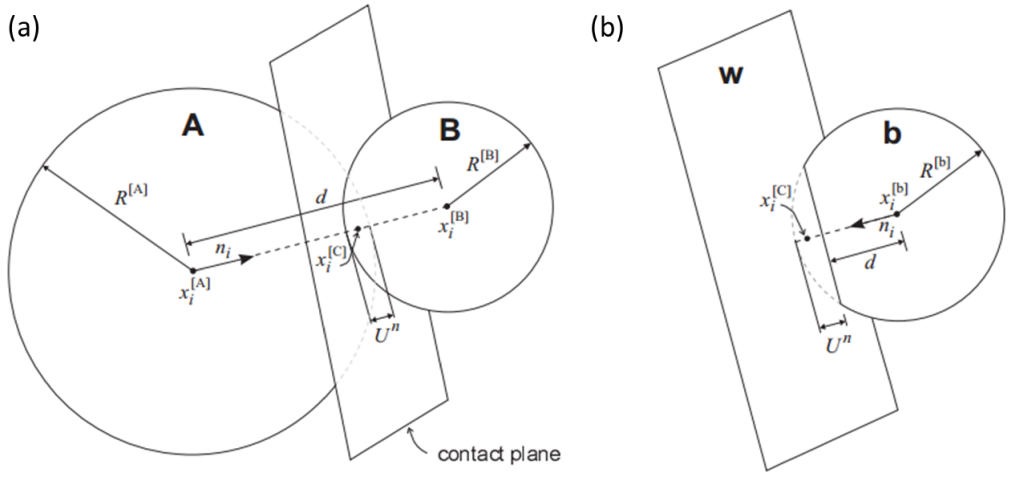

Figure 3.2: Sketch showing the geometry of two interacting particles through a contact: (a) ball-ball contact and (b) ball-wall contact (Itasca, 2008).

ball-wall contact has similar configuration parameters characterizing locations, overlapping and the contact plane shown in Figure 3.2b.

Similar to the mass point used to represent an object in kinetics, a contact is a surrogate for the physical interaction between particles relating to force and momentum. There exist three kinds of behaviour patterns associated with contacts: stiffness, slip and bonding. When two particles overlap, compression develops between them and the force value is related to particle stiffness and overlap quantity. When shear force exceeds a specified maximum value, two particles slip relative to one another. When a bond exists and two particles are pushed away, tensile force accumulates according to the bond stiffness. The bond breaks the connection if the tension is greater than the bond strength. Dynamics in terms of forces and motion of interacting particles are determined by the contact properties. Similar to diverse constitutive relations representing various types of material behaviour, different contact models are needed to parameterize particle communication. In the simplest form, a linear contact model is used to explain how a contact model works.

A linear contact is the basic contact model in PFC. It is characterized by a linear stiffness (force/displacement) during particle interaction. It allows for both slip and bonding (Figure 3.3b and c). The bond is a cement-like material joining two particles together. The bond can break under a certain condition and afterwards the once connected particles behave like unbonded ones.

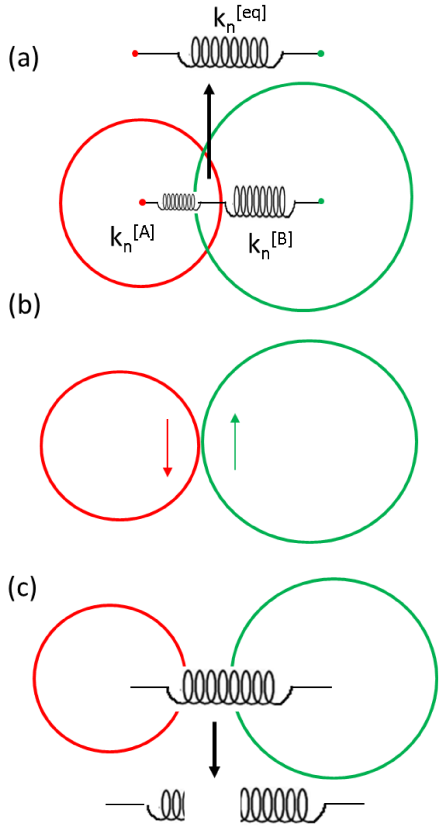

Figure 3.3: Component behaviours associated with the linear contact model: (a) stiffness at the contact point, (b) slip behaviour and (c) bonding between particles and bond failure (adapted from Itasca, 2008).

Similar to particles, contact stiffness includes shear and normal components. The stiffness of the contact is determined by the stiffness of two connecting particles. It can be seen as two springs working in series. The equivalent spring of two springs in series experiences the same value of force as each of

the connecting springs does, otherwise the springs will buckle:

$$\begin{aligned} F^{eq} &= F^A = F^B, \\ k_n^{eq}(x_n^A + x_n^B) &= k_n^A x_n^A = k_n^B x_n^B, \\ k_n^{eq} &= \frac{k_n^A k_n^B}{k_n^A + k_n^B}, \end{aligned} \tag{3.2}$$

where F^{eq} is the force on the equivalent spring, equal to forces F^A and F^B on the springs representing particles A and B. k_n is the normal stiffness and superscripts identify the three springs (Figure 3.3a). Similarly, x_n is the spring displacement.

The shear stiffness of a contact has the same form of relationship with the shear stiffness of particles. Different from compressive forces, the shear force F_s between particles has a limit F_s^{max}. It is subject to a Coulomb-type friction threshold determined by the normal force F_n at the contact and the particle friction coefficient μ (minimum value of two connecting particles):

$$F_s^{max} = \mu \cdot F_n. \tag{3.3}$$

Particles slip relative to one another once the shear force exceeds the limit F_s^{max} and the shear force is then automatically set to this maximum value. The fraction of slipping contacts represents the intensity of particle motions. So the slipping contact ratio (SCR) has been widely used in analysis of granular material modeling (Ferdowsi et al., 2013).

The fact that the contact is inactive until two particles overlap implies the normal component of the contact force can only be compressive. For a more realistic representation of particle interaction, PFC provides the option of adding a bond at the contact. This corresponds to a wide range of rocks

in nature whose cohesion between particles results from compaction or binding phase during their formations (Radjai et al., 2010). The bond works like a glue combining two particles together so tensile forces are attainable. There are two kinds of bonds built into PFC, namely contact and parallel bonds. Bonds in PFC are parameterized by stiffness and strength in the normal and shear directions. When bond strength (normal or shear) is exceeded, the bond will break (Figure 3.3c).

These two bonds differ in application area. Contact bonds act on a vanishingly small area. It does not resist relative rotation, so only forces can be transmitted. The contact bond can be seen as springs with limits in the normal and shear directions (Figure 3.4a). In the normal direction, the spring continues working when two particles are no longer in touch compared with unbonded particles (Figure 3.4b). The contact force is computed by:

$$\begin{aligned} F_n &= k_n \cdot U_n, \\ F_s &= k_s \cdot U_s, \end{aligned} \tag{3.4}$$

where F_n and F_s are the normal and shear components of the contact force. k_n and k_s represent stiffnesses in the normal and shear directions. U_n is the distance between particles. There is overlap when $U_n \geq 0$ and $U_n < 0$ means two particles are pulled away. U_s is the shear displacement. If the normal/shear component of the contact force exceeds the corresponding strength, F_c^n and F_c^s, the bond will break (Figure 3.4b and c).

Another difference is that contact bonds and slip behaviour are not compatible (Figure 3.4a and d). If the contact bond is installed, slip behaviour is inactive regardless of the value of shear force unless the bond is broken. The contact bond is defined by normal and shear bond strength, F_c^n and F_c^s. The strength used in the contact model is force. The contact force is iteratively

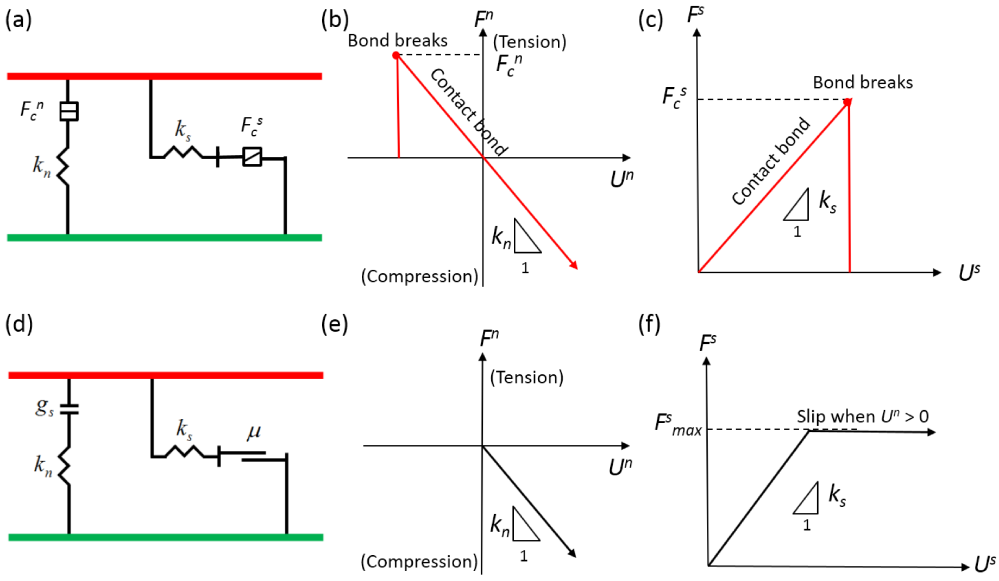

Figure 3.4: Particle interactions at a point: the top panel shows the bonded behaviour and the bottom depicts the unbonded behaviour. (a) and (d) are physical analogs. (b), (c), (e) and (f) illustrate the behaviour in terms of forces $F^{[n/s]}$ and displacement $U^{[n/s]}$ (adapted from Itasca, 2008).

compared to the strength values to update the bond state. The particles act like unbonded particles once the bond breaks. The interactions between unbonded particles are like springs linked with dividers, sustaining forces only when particles overlap (Figure 3.4d). The normal and shear stiffness values of the bond are equal to those of the contact.

Parallel bonds work on a small area whose radius $\overline{R}$ is defined by the user (Figure 3.5b). As rotation between particles is resisted, both forces and momentum can be transmitted from particle to particle via parallel bonds. Reflecting its name, parallel bond works in parallel with the contact. It can be seen as two springs working in parallel (Figure 3.6a) with stiffnesses k_n and $\bar{k}_n$ in the normal direction and k_s and $\bar{k}_s$ in shear. The overbar is used to distinguish the bond properties from those of the contact. The bond breakage criterion is stress-based. By beam theory, the maximum tensile and shear stresses in the

periphery of the bond are calculated using force and momentum applied on the bond (Figure 3.5b):

$$\bar{\sigma}^{max} = \frac{-\bar{F}^n}{A} + \frac{|\bar{M}_3|}{I}\bar{R}, \bar{\tau}^{max} = \frac{-\bar{F}^s}{A}, \tag{3.5}$$

where A and I are the area and moment of inertia of the parallel bond cross-section, respectively. The bar accent is used to distinguish the bond-related quantities from the contact-related ones. If the maximum stresses exceeds its corresponding strength, the bond breaks.

The linear contact model is one implementation of particle interaction. It

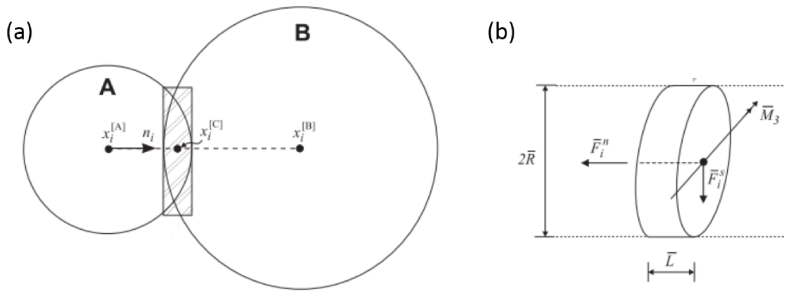

Figure 3.5: (a) Sketch of two particles with a parallel bond and (b) details of the bond in terms of size and transmitted force and momentum (Itasca, 2008).

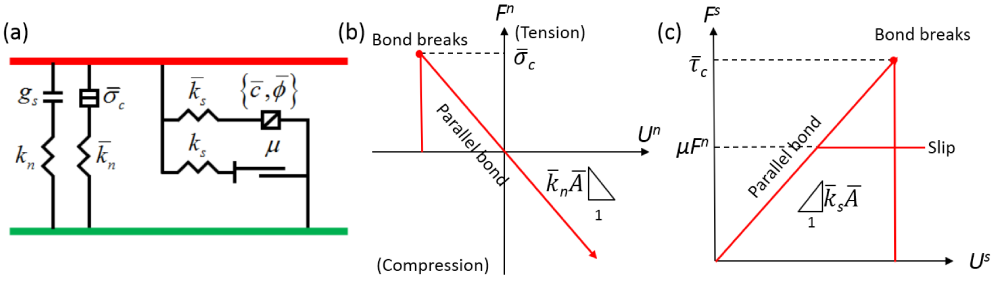

Figure 3.6: Parallel bond behaviour: (a) the physical analog and bond behaviour in terms of forces and displacement in (b) normal and (c) shear directions (adapted from Itasca, 2008).

depicts compression, slip, tearing apart and complete detachment between par-

ticles as mentioned before. However, the assumption of a constant stiffness can be oversimplified for a variety of materials and loading conditions. PFC also provides other options. Table 3.2 lists several contact models in PFC to simulate a certain rock behaviour. The linear contact model with parallel bonds is used to simulate compression tests.

Contact models	Features
Simple ductile model	Softening slope instead of constant slope of force-displacement curve in contact-bond behaviour
Smooth-joint model	Simulate a joint-like structure, a weak plane larger than contact interface, in PFC
Simple viscoelastic model	Add a dashpot in series with springs to simulate a time dependence of stress on strain
Stress corrosion model	Add a damage-rate law to the parallel-bond for a time-dependence of brittle failure (Potyondy, 2007)

Table 3.2: Examples of additional contact models in PFC.

Walls

Walls in PFC have two main functions. The first one is to use walls as a temporary constraint for particle generation. The walls set up a vessel customized to hold the model with a specified shape and size. Then particles are generated within the region. The outcome is called a specimen. After generation, the specimen can be removed from the vessel by deleting walls.

The second use is to apply boundary conditions. If not deleted, walls can continue working in the form of boundary constraints. In PFC, forces cannot be applied on walls directly by the user. The only way to control walls is to set a velocity. Constant velocity corresponds to a fixed strain rate. The resultant force on the particles can be monitored during simulation. Another boundary condition is to use a feedback mechanism to maintain constant stress on walls

by adjusting their velocities. This boundary condition is sometimes used to introduce excitations in the model. A more complex velocity history can be implemented too. Then the model evolves with the stimulation and the resulting particle interaction can again be monitored.

3.2.2 Model formulation

As mentioned before, geomechanical modeling is based on two key items, namely the equation of motion and the constitutive relations appropriate for the modeled material. In PFC, the constitutive relation is depicted at a microscale, that is, the contact model at each contact. The contact behaviour links the displacement and resultant force/momentum at the contact. The force/momentum in turn determines the particle motion according to Newton's second law in terms of translational and rotational motion. PFC adopts a time-stepping algorithm to develop a dynamic simulation of the model. The calculation alternates between contact model and motion equation at each step.

Figure 3.7 shows the calculation cycle in PFC. Each step starts from the spatial information of balls and walls, $x_i^{(P)}$ and $x_i^{(w)}$. Then the assembly of contacts gets updated in terms of position $x_i^{(c)}$ based on the contact geometry (Figure 3.2). According to the contact model, contact forces F^n and F^s are then derived. The state of the parallel bond is checked at every calculation step, if intact, bond forces and momentum ($\overline{F}_i^s$, $\overline{F}_i^n$ and $\overline{M}_3$) are also calculated. Before jumping to the application of the motion equation, the shear component of contact force F^s and maximum stresses at the bond, $\overline{\sigma}_{max}$ and $\overline{\tau}_{max}$, are compared with their limit values. If the shear force is greater than the maximum value F_s^{max} (Equation 3.3), the connecting particles will slip and the shear force is set to the maximum value. If either of the maximum stresses around the bond area exceeds the strength values ($\overline{\sigma}_c$ and $\overline{\tau}_c$), the bond will

break, and forces and momentum on the bond are deleted. Then the resultant forces on the related particles become available to update the motion of particles. Together with the updated wall positions calculated from the prescribed wall velocities, they are used in the next calculation step. The time step should be determined based on considerations of both the computation stability and efficiency.

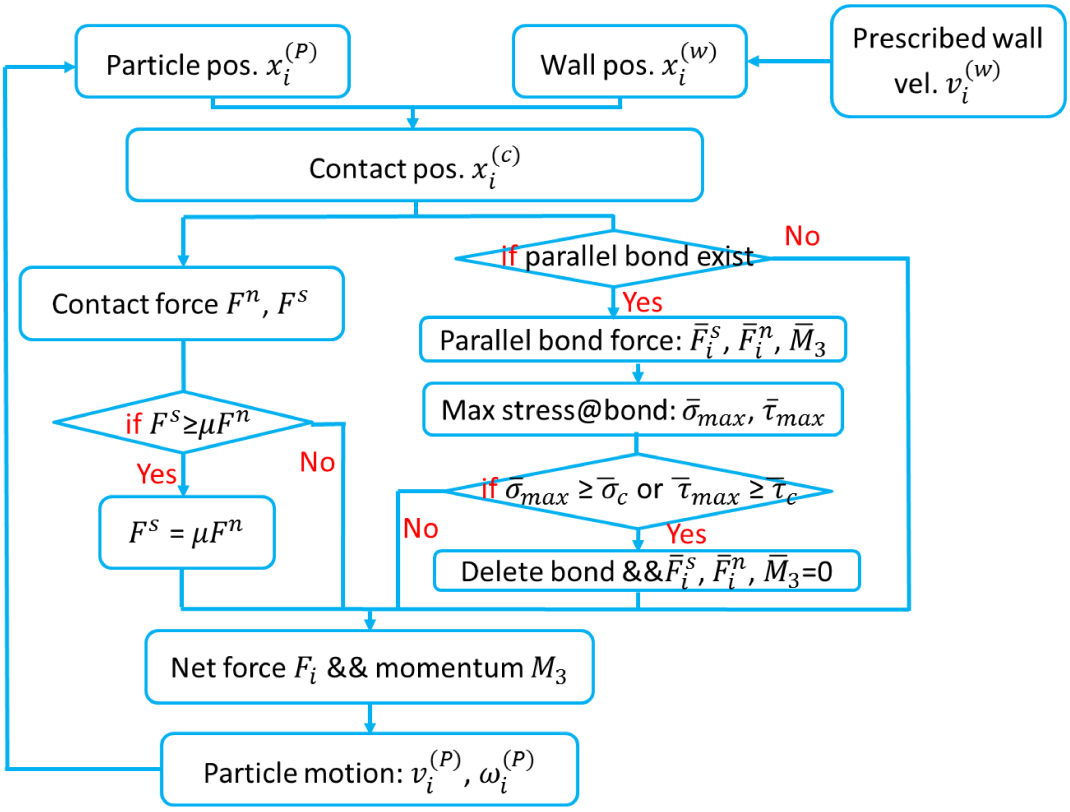

Figure 3.7: Calculation cycle in PFC.

3.2.3 Model implementation issues

The previous content introduces how a PFC model works. This section is concerned with several practical issues encountered in rock behaviour simulations.

Stress measurement strategies

One advantage of numerical simulations is its possibly continuous information stream during the simulation process. The kinetic and dynamic information are recorded to interpret the model behaviour. Quantities like velocities and forces are easy to follow and can be extracted from the model results. However, stress needs an extra treatment.

Stress is a continuum concept whereas PFC is a discrete model. Stress does not exist at a single particle; instead contact forces and particle displacements are calculated and recorded. They can be used to estimate the stress in the model. Two techniques for stress calculation are included in PFC: (1) boundary-based stress by dividing forces on walls or outermost particles by the cross-sectional area of the specimen's side; (2) average stress within a specific area extracted by means of measurement circles (2D) or spheres (3D). Both of these methods are used in this work.

The wall-based stress calculation gives an overall estimate of the stress state in the sample during simulation. For example, the axial stress is calculated by dividing the forces on the horizontal walls, F_y, with the width of the sample, wd. Forces exerted on the walls are recorded using:

$$F_y = 0.5 \times \left(W_y^2 - W_y^1\right), \tag{3.6}$$

where W is the force on the wall. The subscript corresponds to the individual component of the force. The superscript represents wall index, where 1 is bottom and 2 is top wall (Figure 3.8). The wall-based stress calculation calculates average forces on two opposing walls so the factor $\frac{1}{2}$ is used.

Sample dimensions are measured by monitoring the location of the confin-

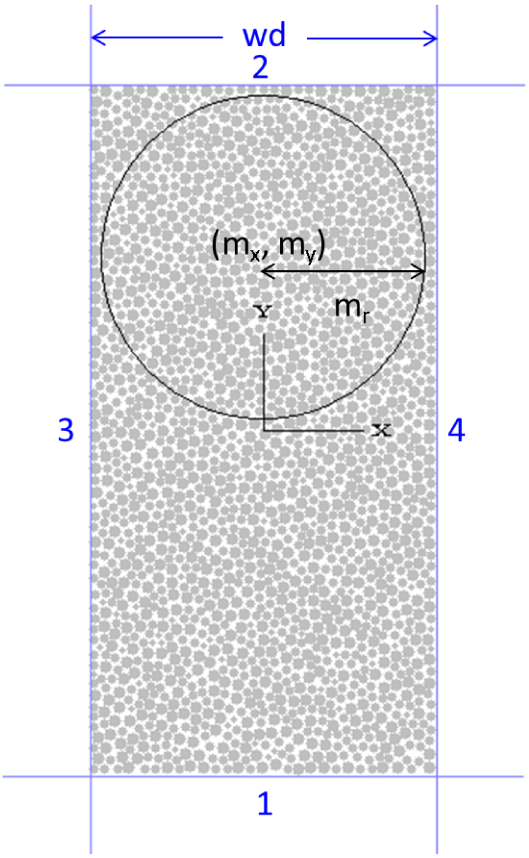

Figure 3.8: Sketch of wall- and measurement-based stress calculations. The blue numbers represent the specific walls: 1-bottom, 2-top, 3-left, and 4-right.wd is the width of the specimen used for the axial stress calculation (Equation 3.8). The black circle centering at (m_x, m_y) with a radius of m_r is an example of the measurement circle.

ing walls. The width is calculated by:

$$wd = x^4 - x^3, \tag{3.7}$$

where x^4 represents the position of the right wall and x^3 is the location of the left one (Figure 3.8).

Then, in two-dimensional simulations, the axial stress along the vertical

direction can be calculated through:

$$\sigma_{yy} = \frac{F_y}{wd}. \tag{3.8}$$

The wall-based stress is monitored during the whole simulation to give an overall picture of the stress state throughout the sample. Stress accumulation leads to bond breakage. A bond breakage is actually a conversion of strain energy into kinetic energy. When the released energy is large enough, the wall can 'detect' the change and a sudden drop occurs in the axial stress.

The measurement-based stress gives a detailed description of the stress state at a microscale defined by the size and position of the measurement circle. The circle is defined by its center (m_x, m_y) and radius m_r (Figure 3.8). The displacements and forces of all the particles within the measurement circle are used to calculate the averaged stress $\overline{\sigma}_{ij}$ based on the concept of homogenization (Jing and Stephansson, 2007):

$$\overline{\sigma}_{ij} = \frac{1-n}{\sum_1^{N_p} V^{(p)}} \sum_1^{N_p} \sum_1^{N_c^{(p)}} \left(x_i^{(c)} - x_i^{(p)} \right) F_j^{(c,p)}, \tag{3.9}$$

where n is the porosity in the measurement circle, N_p is the total number of particles within the measurement circle, $V^{(p)}$ is the volume taken by one particle, $N_c^{(p)}$ is the number of contacts around one particle, $x_i^{(c)}$ and $x_i^{(p)}$ give locations of a specific contact and its particle, and $F_j^{(c,p)}$ is the associated contact force. The derivation of Equation 3.9 can be found in the PFC2D manual (Itasca, 2008).

The measurement-based stress cannot be obtained in laboratory tests. Yet it gives pertinent information to analyze the behaviour of materials, including stress phenomena due to local failure. Laboratory tests can only obtain wall-

based stresses. So comparison between PFC models and real materials should rely on wall-based results.

Damping and dynamical modeling

A numerical damping force is added in the PFC system to absorb energy for an accelerated convergence. Rocks in nature have various mechanisms like internal friction and scattering to dissipate energy. However, a PFC model can only dissipate energy through frictional sliding, which is insufficient to reach a steady state within a reasonable number of calculation steps. A numerical damping force is introduced. It is added to each particle every step. The magnitude of the damping force is proportional to the unbalanced force to stabilize particles:

$$F^d = -\alpha |F| sign(v), \tag{3.10}$$

where F^d is the damping force, α is called the damping parameter which determines the damping level, $|F|$ is the magnitude of the unbalanced force and $sign(v)$ is the sign of the velocity of the particle. The measurement of attenuation in rocks, the quality factor, Q is inversely proportional to the damping parameter α (Hazzard and Young, 2004):

$$Q = \frac{\pi}{2\alpha} \tag{3.11}$$

The default value of the damping parameter α is 0.7, corresponding to a high level of damping. As simulations in this thesis involves dynamic processes where wave propagation is crucial, a lower damping equal to 0.0157 is used to attain a realistic level of energy dissipation in granite. It corresponds to a Q value equal to 100. The damping parameter is switched to this low value to allow for wave propagation when a bond breaks, and switched back to 0.7 after the influence of wave propagation is believed to terminate to maintain a reason-

able rate of convergence. Bond failure thus redistributes stress in its vicinity due to the deformation of contacts and bonds in the neighbouring particles.

Chapter 4

Analytical and numerical computation of stresses and strains

4.1 Introduction

The particle-based method allows for examination of wave propagation and stress patterns at the microscopic scale. In this section, wave propagation is simulated using a bonded particle method to validate its capability of wave propagation simulation. Elastic wave propagation is simulated by exciting a particle with a single force. I then compare the resulting displacements and radiation patterns with the analytic results to validate the simulation results. Finally, characteristics of wave propagations in a discrete model are discussed.

4.2 Theory

4.2.1 Analytic solutions

Displacement field

First, a point source is considered. More complex sources with a spatial extent can be constructed from an integral of this end-member case. The nth component of the displacement $\boldsymbol{u}(\boldsymbol{x}, t)$ at the observation position $\boldsymbol{x}$, due to a point force at the origin in the pth direction with a time-varying magnitude F_p, in a homogeneous, isotropic, elastic and unbounded medium is (Aki and Richards, 2002):

$$\begin{aligned} u_n(\mathbf{x}, t) &= F_p * G_{np} \\ &= \frac{1}{4\pi\rho}\left(3\gamma_n\gamma_p - \delta_{np}\right)\frac{1}{r^3}\int_{\frac{r}{\alpha}}^{\frac{r}{\beta}} \tau F_p\left(t-\tau\right)d\tau \\ &+ \frac{1}{4\pi\rho\alpha^2}\left(\gamma_n\gamma_p\right)\frac{1}{r}F_p\left(t-\frac{r}{\alpha}\right) \\ &+ \frac{1}{4\pi\rho\beta^2}\left(-\gamma_n\gamma_p + \delta_{np}\right)\frac{1}{r}F_p(t-\frac{r}{\beta}), \end{aligned} \tag{4.1}$$

where G_{np} is the Green's function, γ_i is the direction cosine with the ith axis at the observation point $\boldsymbol{x}$, r is the source-receiver distance, α and β are the P- and S-wave speed respectively, and ρ is the density of the medium. δ_{ij} is the Kronecker symbol.

Equation 4.1 shows the displacement is made up of three parts and they are known as the near-field, far-field P- and S-wave terms (Aki and Richards, 2002). Each term is made up of four constituents: (1) a constant, (2) a distance-dependent variable, responsible for geometric attenuation, (3) a space-dependent factor, included in the bracket, also called the radiation pattern, and (4) a time-dependent variable, modifying the shape of the source waveform F_p.

The radiation pattern is a linear combination of direction cosine γ_i. It reflects the wave polarization at a wavefront. The near-field wave motion has both radial and transverse components. It is a mixture of P- and S-waves. The far-field P-wave term has only a radial component and that is why it is termed as a P-wave. Similarly, only a transverse component exists in the far-field S-wave term.

The time-dependent variable which includes F_p, reflects the waveform of each term. According to Equation 4.1, the far-field P- and S- wavefields have the same waveform as the source wavelet, but with a lag. The P-wave arrives at a time of $\frac{r}{\alpha}$ while the S-wave has an arrival time of $\frac{r}{\beta}$. Both of them have the same period as the source, T. The near-field wavefield has an integration from the far-field P- to the S-wave arrival times. So it has a longer duration time equal to $\frac{r}{\beta} - \frac{r}{\alpha} + T$. According to the mathematical expression, the near-field waveform is part of the convolution of the source wavelet with time, depending on the integral interval related to the source-receiver distance r. So the near-field waveform varies with r. This can complicate for instance the calculation of wave velocities when the receiver is at a position where the near-field influence cannot be ignored.

The r-variable in each term is responsible for attenuation with travelled distance. It determines which term in Equation 4.1 is more dominant at a specific position. Aki and Richards (2002) gave the frequency-domain representation of Equation 4.1 to demonstrate the relative dominance. Following the notation and convention of the following Fourier transform:

$$F(\omega) = \int_{-\infty}^{+\infty} f(t)\, e^{+i\omega t} dt \tag{4.2}$$

The Fourier transform of Equation 4.1 is:

$$\begin{aligned} U_n(\mathbf{x},\omega) &= F_p(\omega)\, G_{np}(\omega) \\ &= \frac{F_p(\omega)\, e^{i\omega\frac{r}{\alpha}}}{4\pi\rho\alpha^2 r}\left[\gamma_n\gamma_p + (3\gamma_n\gamma_p - \delta_{np})\left(I_P + I_P^2\right)\right] \\ &- \frac{F_p(\omega)\, e^{i\omega\frac{r}{\beta}}}{4\pi\rho\beta^2 r}\left[(\gamma_n\gamma_p - \delta_{np}) + (3\gamma_n\gamma_p - \delta_{np})\left(I_S + I_S^2\right)\right], \end{aligned} \tag{4.3}$$

where $I_P = i\frac{\alpha}{\omega r}$ and $I_S = i\frac{\beta}{\omega r}$.

The frequency representation shows that P- and S-wavefields can be independently expressed in the frequency domain. Besides, the relative dominance of the near- and far-field components at a point can be determined by comparing the two terms in the square brackets. The first term within the brackets corresponds to the far-field term, and the second term to the near-field contribution. Since the radiation patterns are of the same order of magnitude, dominance can be decided by comparing the weights. The weight of the far-field contribution is a constant, equal to 1. For the near-field term, the weight is a quadratic polynomial of a distance-dependent variable, I_P and I_S. For simplicity, the imaginary unit is ignored and only the physical meaning of $\frac{\alpha}{\omega r}$ and $\frac{\beta}{\omega r}$ is explained here.

$$\frac{\alpha}{\omega r} = \frac{1}{\omega r/\alpha} = \frac{1}{2\pi f r/\alpha} = \frac{1}{2\pi r/\lambda_P} = \frac{1}{2\pi \times n_P}, \tag{4.4}$$

where n_P is the number of wavelengths λ_P at a distance r for a P-wave of frequency ω. Factor $\alpha/\omega r$ is inversely proportional to n_p and n_p is proportional to r for a given frequency wave. So the relative dominance depends on the distance. The factor $\alpha/\omega r$ approaches infinity and hence the near-field is more dominant, when receivers are positioned a small fraction of a wavelength away from the source. When positioned at several wavelengths, $\alpha/\omega r$ approaches zero and the far-field term becomes the significant contribution.

The factor$\beta/\omega r$ has the same property as $\alpha/\omega r$.

In short, the displacement due to a single force in a homogeneous, isotropic, elastic and unbounded medium is made up of three parts, namely the near-field waves, far-field P-wave and far-field S-wave. They propagate from the source with a circular front and a certain radiation pattern. They attenuate with the travelled distance r. The near-field waves dominate within a distance of a small fraction of the wavelength, and the far-field waves become dominant at positions several wavelengths away from the source.

Stress field

The transient stress perturbations due to wave propagation can be linked to the displacement expressed in Equation 4.1 by the stress-strain relationship and the geometric equation (Equation 2.9). Combined with Hooke's law for homogeneous and isotropic media (Equation 2.15), the following relationship is obtained:

$$\sigma_{ij} = \lambda \delta_{ij} u_{p,p} + \mu \left(u_{i,j} + u_{j,i} \right), \tag{4.5}$$

where λ and μ are known as the Lamé's moduli and $u_{i,j}$ is the spatial derivative of displacement component u_i along the jth direction.

Inserting Equation 4.1 into Equation 4.5, the dynamic stress associated with an elastic wave due to a point source in a homogeneous, isotropic, elastic and

unbounded medium is,

$$\begin{aligned}
\sigma_{ij}(\mathbf{x},t) = & \frac{1}{4\pi\rho}\frac{1}{r^4}\left(\lambda\delta_{ij}A_N+\mu B_N\right)\int_{\frac{r}{\alpha}}^{\frac{r}{\beta}}\tau F_p(t-\tau)d\tau \\
& + \frac{1}{4\pi\rho\alpha^2}\frac{1}{r^2}\left(\lambda\delta_{ij}A_{IP}+\mu B_{IP}\right)F_p\left(t-\frac{r}{\alpha}\right) \\
& + \frac{1}{4\pi\rho\beta^2}\frac{1}{r^2}\left(\lambda\delta_{ij}A_{IS}+\mu B_{IS}\right)F_p\left(t-\frac{r}{\beta}\right) \\
& + \frac{1}{4\pi\rho\alpha^3}\frac{1}{r}\left(\lambda\delta_{ij}A_{FP}+\mu B_{FP}\right)\dot{F}_p\left(t-\frac{r}{\alpha}\right) \\
& + \frac{1}{4\pi\rho\beta^3}\frac{1}{r}\left(\lambda\delta_{ij}A_{FS}+\mu B_{FS}\right)\dot{F}_p\left(t-\frac{r}{\beta}\right),
\end{aligned} \tag{4.6}$$

where the dot represents the temporal derivative. The parameters are given by:

$$\begin{aligned}
\begin{bmatrix} A_N \\ A_{IP} \\ A_{IS} \\ A_{FP} \\ A_{FS} \end{bmatrix} &= \begin{bmatrix} -15 & 6 & 3 \\ -6 & 2 & 1 \\ -6 & 3 & 1 \\ 1 & 0 & 0 \\ 1 & -1 & 0 \end{bmatrix} \begin{bmatrix} \gamma_n^2\gamma_p \\ \gamma_n\delta_{np} \\ \gamma_p \end{bmatrix}, \\
\begin{bmatrix} B_N \\ B_{IP} \\ B_{IS} \\ B_{FP} \\ B_{FS} \end{bmatrix} &= \begin{bmatrix} -30 & 6 & 6 & 6 \\ -12 & 2 & 2 & 2 \\ -12 & 3 & 2 & 2 \\ 2 & 0 & 0 & 0 \\ 2 & -1 & 0 & -1 \end{bmatrix} \begin{bmatrix} \gamma_i\gamma_p\gamma_j \\ \gamma_i\delta_{pj} \\ \gamma_p\delta_{ij} \\ \gamma_j\delta_{pi} \end{bmatrix}.
\end{aligned} \tag{4.7}$$

Similar to the displacement, the stress field can be subdivided into several terms. These are, in order of appearance, the near-field, mid-field P-wave, mid-field S-wave, far-field P-wave and far-field S-wave terms, also identifiable by the increasing power in the distance dependence and their arrival times.

4.2.2 Numerical solutions

Upon an excitation, PFC iteratively applies the force-displacement law and the law of motion to each particle in the model (see Chapter 3 for full details). The response to an excitation can be quantified by kinetic parameters like particle velocity and displacement, as well as dynamic parameters like stress and strain.

The wave motion and radiation pattern can be easily recognized from the particle velocity, displacement and stress. Also, the wave propagation velocity can be calculated. Particles can be selected to record signals, similar to receivers used in reflection seismology. Then it is straightforward to compute the propagation velocity using arrival times and positions of these particles.

4.2.3 Model setup

In this chapter I will compare analytic results for particle displacements and stress perturbations due to a single force with those obtained using a PFC simulation. However, general PFC models are confined by rigid walls exerting the boundary conditions. Therefore wave reflections on walls are inevitably complicating a direct comparison of the analytical and modeling results. As a result, a high damping layer is added around the model to absorb the reflections. The model for wave propagation is assembled by fitting together several uniform units using the AC/DC (Adaptive Continuum/DisContinuum) algorithm in PFC (Young et al., 2004). The AC/DC algorithm allows a large model to be quickly assembled with the unit which is already compacted and in equilibrium, and also inexpensive in memory and computation, instead of constructing a large one from scratch.

The unit used is an assembly of 1866 particles, representing a 31.7 x 63.4

mm block of Lac du Bonnet granite. The damping parameter is set to a lower value, 0.0157, to approximate a realistic attenuation in granite. Microproperties input into PFC are listed in Table 4.1. The average particle diameter is 1 mm. Compression tests on the unit model yield the value of macroproperties in Table 4.2 (Potyondy and Cundall, 2004).

Parameter	Value	Unit
Grain density	3169	kg/m^3
Grain Young's modulus	62	GPa
Stiffness ratio for grain	2.5	N/A
Friction coefficient	0.5	N/A
Parallel bond Young's modulus	62	GPa
Stiffness ratio for parallel bond	2.5	N/A

Table 4.1: Microproperties of the unit assembly

Parameter	Value	Unit
Density, ρ	2667	kg/m^3
Young's modulus, E	71.3	GPa
Poission's ratio, ν	0.22	N/A
P-wave velocity, v_P	5525	m/s
S-wave velocity, v_S	3310	m/s

Table 4.2: Macroproperties of the unit assembly (derived in a compression test with confining stresses equal to 10 MPa).

Then using the AC/DC algorithm, a large model used for wave propagation is assembled. The large model is square in shape, made up of 32 units and 60850 particles (Figure 4.1). Particles within the model can be subdivided into two categories according to their functions. The outer boundary (yellow particles) serves as a damping layer to eliminate reflections. These particles are assigned a high damping parameter compared with the inner particles, decreasing the reflecting energy on the boundary. The middle part (grey particles) is the observation area. It is a 126 mm-wide square. The model can be used to

observe the near-field as well as far-field wavefields due to its size. Before the excitation, the sample is subjected to a 10 MPa confining stress to mimic the in-situ stress state of rocks. Then a perturbation is added to the particle in the center to study the wave propagation from a point source and the associated dynamic stresses.

The model used in analytic solutions has the same size as the PFC model,

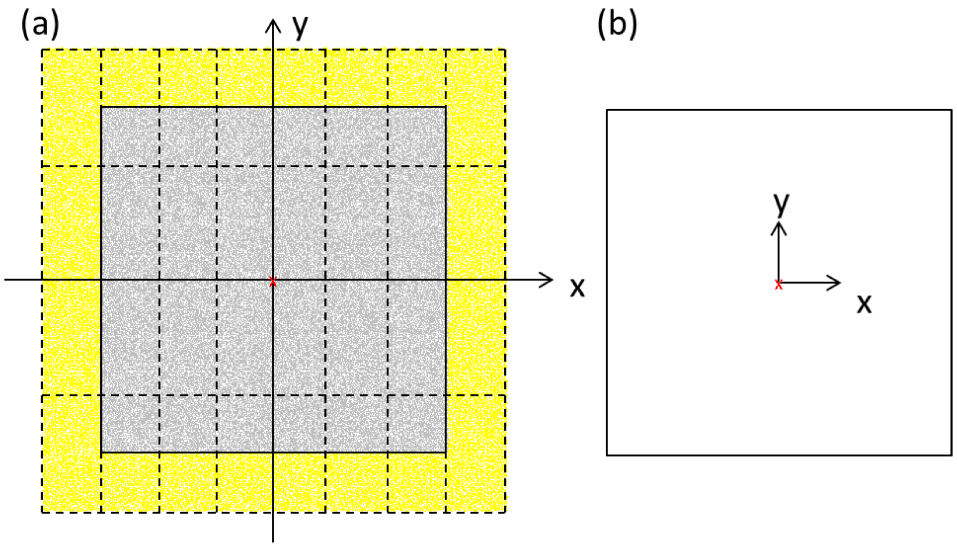

Figure 4.1: Setup of (a) model used in numerical calculation, a large model composed of 32 units (dashed rectangles): monitor area (grey particles), high damping layer (yellow particles) and the source (highlighted with red cross); (b) model used in analytic solution.

a 126mm-wide square. It is characterized by density, P- and S-wave velocity given by the macroproperties of the PFC model (Table 4.2). Resulting particle displacements and stresses are then compared with the analytic predictions, given by Equation 4.1 and Equation 4.6.

4.3 Results: excitation of a single force

A half cycle of a sine wave is input at the center as a point source with a displacement along along the vertical direction. The frequency is set at 100 kHz. The analytical displacement and stress fields are calculated by replacing F_p with a half cycle of sine function along the vertical direction in Equation 4.1 and Equation 4.7. The PFC model is stimulated by a particle displaced vertically with a sinusoidal-varying velocity lasting a half-period for the numerical results.

4.3.1 Analytic solutions

First I compute the resulting analytic wavefields and stresses.

Displacement field

Figure 4.2 shows the radiation pattern of the displacement field in terms of near- and far-field components. It clearly shows the near-field waves are a mixture of P- and S-waves, having both non-zero radial and transverse components. In the far-field terms, the P- and S-waves are decoupled. P-waves have only a radial component, as defined from the origin (center). The radiation pattern has a symmetry axis in the direction of the source motion, i.e., the y-axis. The S-wavefield has only a transverse component and the symmetry axis is perpendicular to the source particle motion, that is, the x-axis. For P-waves, both near- and far-fields have the same polarities whereas for S-waves, they have opposite polarities as predicted by radiation terms in Equation 4.1.

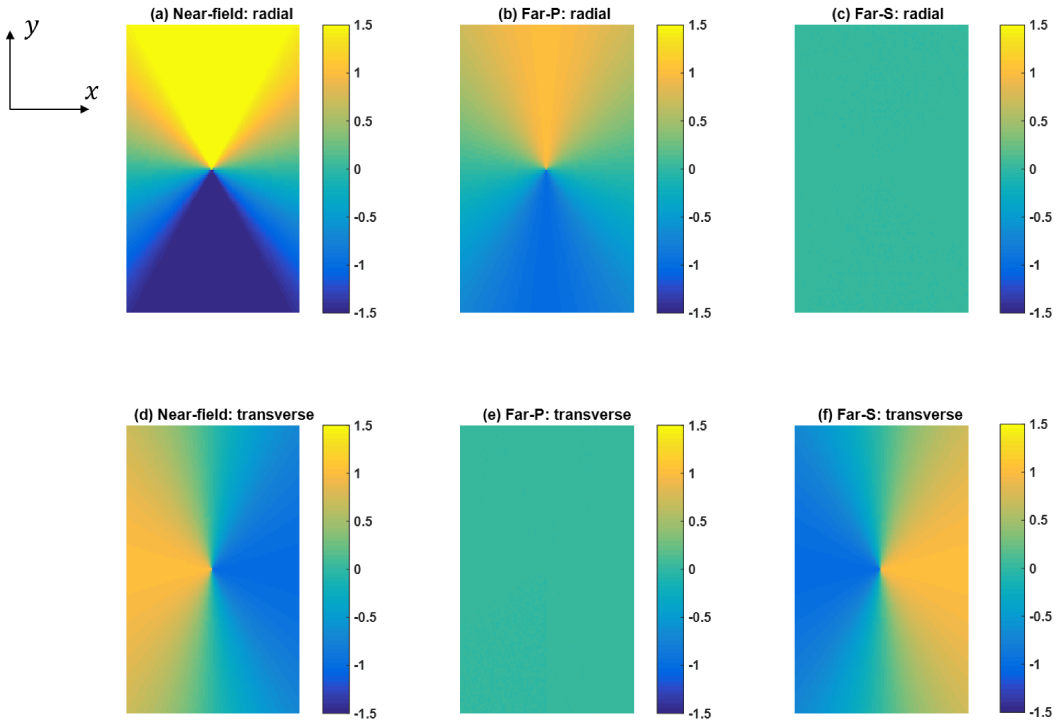

Figure 4.2: Radiation pattern of the displacement field due to a single force: (a) and (d) near-field waves, (b) and (e) far-field P-wavefield and (c) and (f) far-field S-wave in terms of radial (top panels) and transverse (bottom panels) components.

Figure 4.3 shows the analytic solution of the spatial distribution of the displacement field in terms of the different components. The x-components of the near-field, far-field P-and S-wavefields have four quadrants placed in an anti-symmetric way, whereas the y-components have two symmetric lobes but with a perpendicular axis of symmetry. This conforms to the properties displayed in Figure 4.2. It also shows the P-wave propagates faster than the S-wave, but the latter is stronger. The overall field, given by the sum of theses three terms, mainly shows the same pattern as the far-field S-wave motion (Figure 4.4). The displacement field is propagating outwards with the same pattern but decreased amplitudes due to geometric spreading.

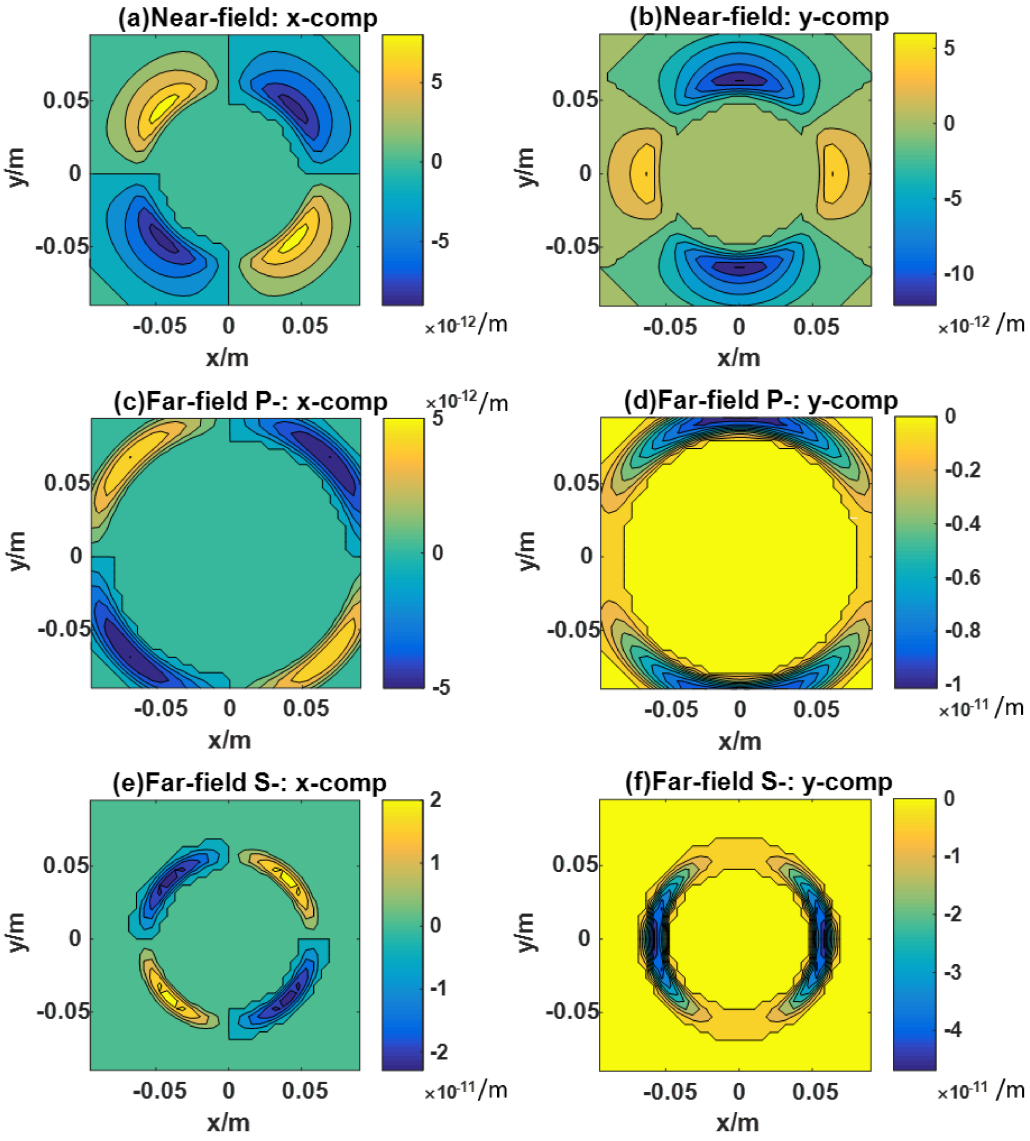

Figure 4.3: Analytic solutions of the displacements of the near-field (a and d), far-field P- (c and d) and S-wavefields (e and f) in terms of horizontal and vertical components.

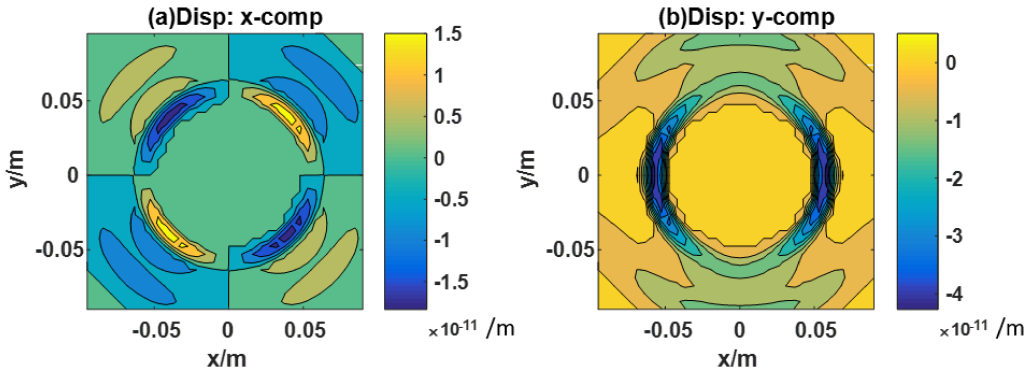

Figure 4.4: Analytic solutions of the complete displacement field: (a) horizontal component and (b) vertical component.

Stress field

According to Equation 4.6, the stress field can be subdivided into near-, mid- and far-fields (Figure 4.5). The far-fields display two concentric loops of alternating lobes because time derivatives of the waveforms are involved. Conversely, both the near- and mid-fields have only one concentric loop of lobes. Like the displacement field, the stress field also has various symmetries and again S-waves play a more dominant role. So the complete stress field (Figure 4.6), the sum of the above terms, show the same radiation pattern as the far-field S-wave stress field.

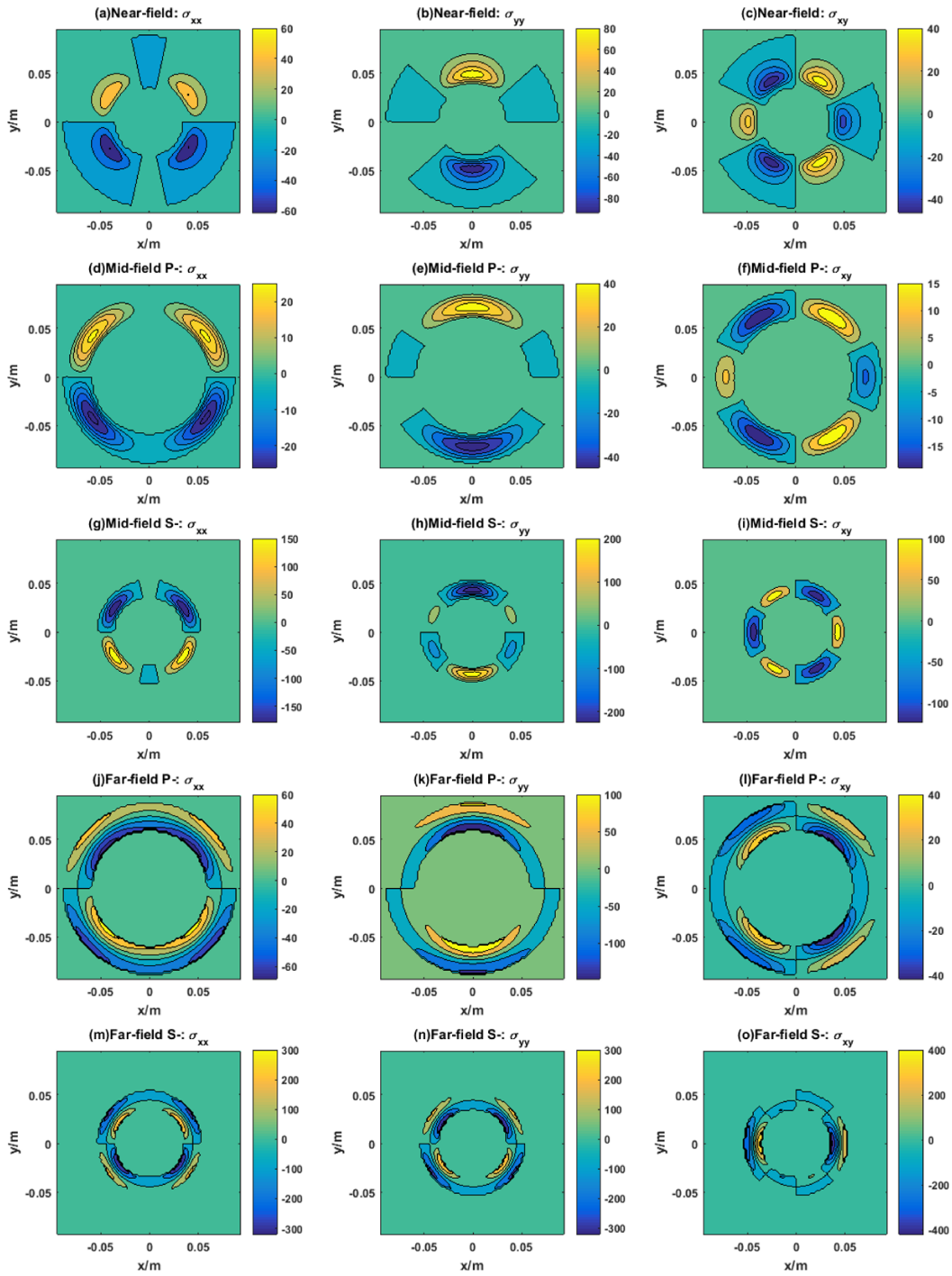

Figure 4.5: Analytic solutions of stresses of the near-field (a-c), mid-field P-wavefield (d-f), mid-field S-wavefield (g-i), far-field P-wavefield (j-l) and far-field S-wavefield (m-o) in terms of normal stresses σ_{xx}, σ_{yy} and shear stress σ_{xy}. See individual titles for the detailed figure information. For the normal stresses, positive values represent tension and negative ones denote compression.

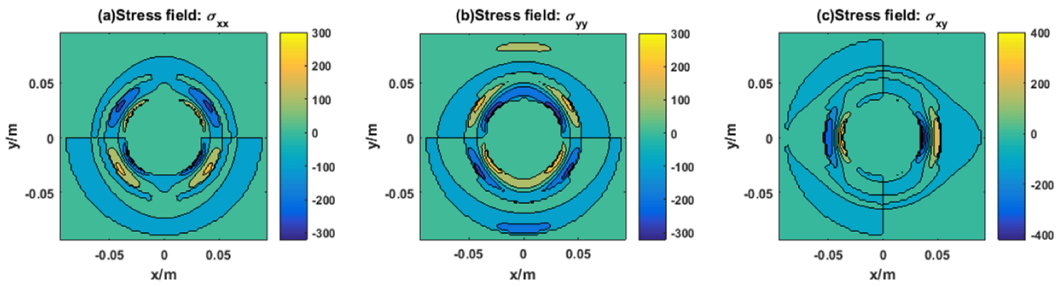

Figure 4.6: Analytic solutions of the stress field: (a) horizontal normal stress σ_{xx}, (b) vertical normal stress σ_{yy} and (c) shear stress σ_{xy}. For the normal stresses, positive values represent tension and negative ones denote compression.

4.3.2 Numerical solutions

A sinusoidal-varying particle velocity perturbation is injected at the center particle. The frequency is again 100 kHz. The perturbation is along the vertical direction and half-cycle long in time, same as the reference run. The downward movement of the source particle activates its adjacent particles, disturbing their neighbouring particles. This chain reaction of particle motion forms wave propagation. Figure 4.7 and 4.8 shows the resulting displacement and stress fields. The displayed numerical solutions are calculated at the time instants same as the analytic ones in Figure 4.3, 4.4, 4.5 and 4.6.

Displacement field

In the direction perpendicular to the source particle motion, the displacement field shows two concentric loops of four alternating quadrants (Figure 4.7a). The inner and outer loops have opposite polarities. The y-component of the displacement field also displays two loops. The outer loop has four quadrants: negative at the top and bottom and positive at the sides. The inner circle consists of two negative regions symmetric to the vertical axis.

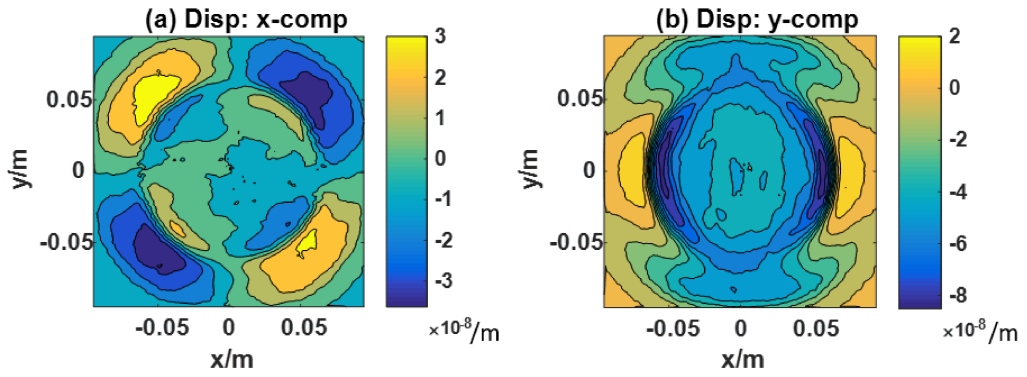

Figure 4.7: PFC results of the displacement field: (a) x-component and (b) y-component.

Stress field

The stress field is more ambivalent compared with the displacement field due to persistent speckle noise patterns (Figure 4.8). The former are partially created by wave scattering due to the packing of the bonded particles. Four quadrants exist in the horizontal normal stress σ_{xx}, displaying compression in the top and tension in the bottom respectively. The vertical normal stress σ_{yy} shows three concentric loops. The outer loop shows a 360-degree periodicity with opposite signs at the top and bottom. The two inner loops comprise four quadrants with opposite polarities. The shear stress-field is simpler with two portions of opposite signs placed at the sides.

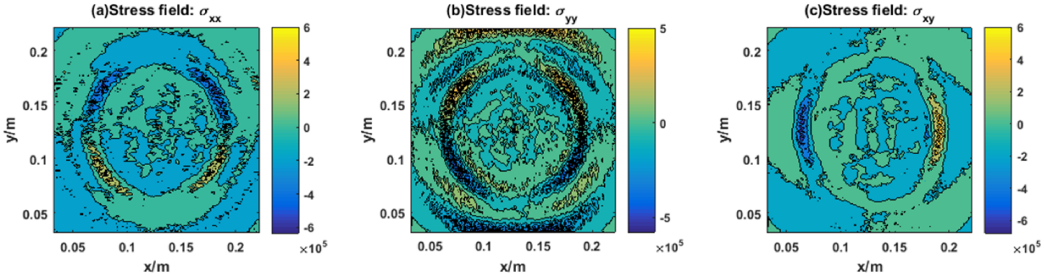

Figure 4.8: PFC results of the stress field: (a) horizontal normal stress σ_{xx}, (b) vertical normal stress σ_{yy} and (c) shear stress σ_{xy}. For normal stresses, positive values represent tension and negative ones denote compression.

4.3.3 Discussion: comparison between the analytic and numerical solutions

The analytic solution is based on the assumption of a homogeneous, isotropic and elastic medium, whereas the numerical calculator PFC is an inhomogeneous and damped system. So differences between these two solutions should be expected.

For the displacement field, basically, the PFC results have the same pattern as the analytic solutions (Figure 4.4 and 4.7). The differences reside in the location and shape of the main lobes. The main lobes extent to a further distance from the source. As the two solutions are shown at the same time instance, it implies a higher velocity of wave propagation in PFC. This relates in part to the difference between the dynamic velocity in PFC and the static velocity prescribed in the analytic solution. The static velocities are calculated by elastic constants E and ν given in Table 4.2. This coincides with the fact which is shown in the following section that the static velocities are smaller than the dynamic ones. Dispersion may also play a role as shown in the next section. Another difference is the shape of the outer loops. The outer two loops in the analytic solution are the remains of the near-field and far-field P-wavefields when summed together. They become one in PFC. Despite of these two points, PFC shows comparable features with the analytic solution.

The stress field is more complex than the displacement field. The analytic solutions and PFC results show similar stress fields in terms of patterns and polarity (Figure 4.6 and 4.8). However, the speckle noise masks many of the features clearly visible in the analytical solutions. The PFC stresses are likely more diverse due to the use of a discretized grid of individual particles, leading to wave scattering and stress heterogeneity.

The similarities between the analytic and simulated results in both the displacement and stress fields gives confidence that PFC can be used to study wave propagation and dynamic triggering due to brittle failure.

4.4 Further analysis

4.4.1 Characteristics of wave propagation in PFC

The previous section shows that displacement of a single particle generates both P- and S-waves. However, various aspects of wave propagation in PFC are not yet clear. For instance, what is the propagation speed? Are the results frequency dependent?

In this part, a series of 20 particles are registered (R1-20) to further study wave propagation in PFC with the same model (Figure 4.9). They serve as receivers used in laboratory and field work to record particle velocities. They are placed along the horizontal and vertical directions with the same spacing, about 15-particle-diameter lengths around a source particle in the center. According to the source-receiver geometry, the horizontal components of the receivers along the vertical direction (R11-20) record transverse motion and vertical components correspond to radial motion. Similarly, the horizontal and vertical components of the receiver recordings along the horizontal direction (R1-10) trace radial and transverse motion, respectively.

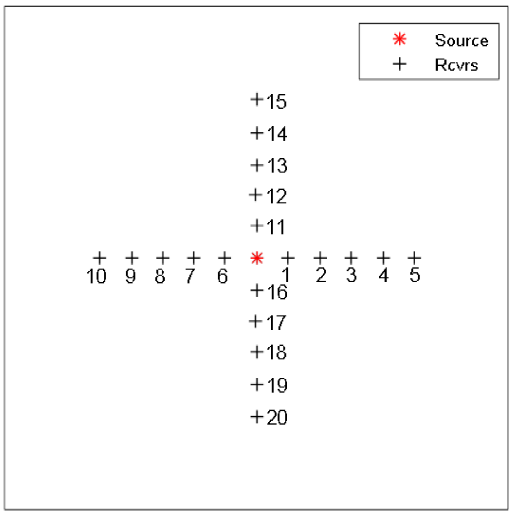

Figure 4.9: Geometry of the source (red asterisk) and receiver particles (plus signs).

Source particle motion

Both PFC and the analytic solutions allow for more complex excitation patterns than a partial sinusoid. The objective of this section is to study the frequency dependence of wave propagation. So it is important that the spectral characteristics are easily visualized. I will therefore use a longer excitation duration consisting of several cycles in a sinusoid. Figure 4.10 shows why. As the length of the excitation signal increases, the peak frequency is more localized around the base frequency and less side lobes are visible. For easier comparison in the frequency domain and limited calculation time, a five-period signal is used instead of the half-cycle used in the previous section.

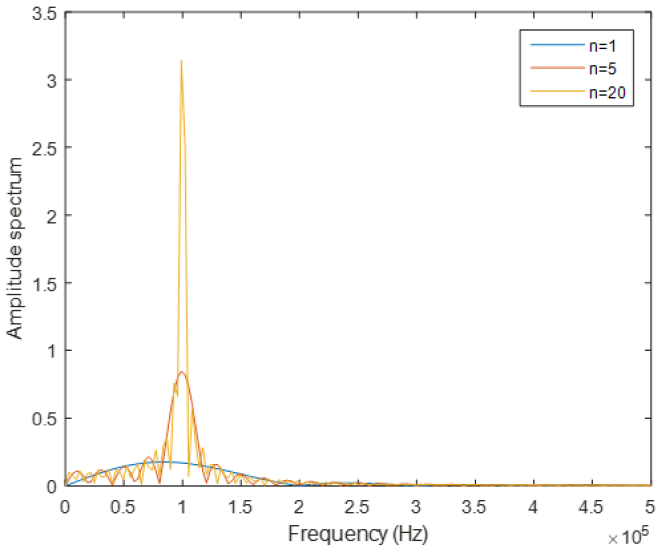

Figure 4.10: Spectrum of sine waves with different lengths (1,5,20 full periods) showing truncation leads to spectral leakage.

A five-period sine wave is input as the source particle velocity along the vertical direction. Due to the internal calculation algorithm, despite having a prescribed velocity perturbation, the source particle is still subject to forces applied by its immediate neighbouring particles. Thus the observed motion at the source particle is different from the input (blue curve in Figure 4.11a).

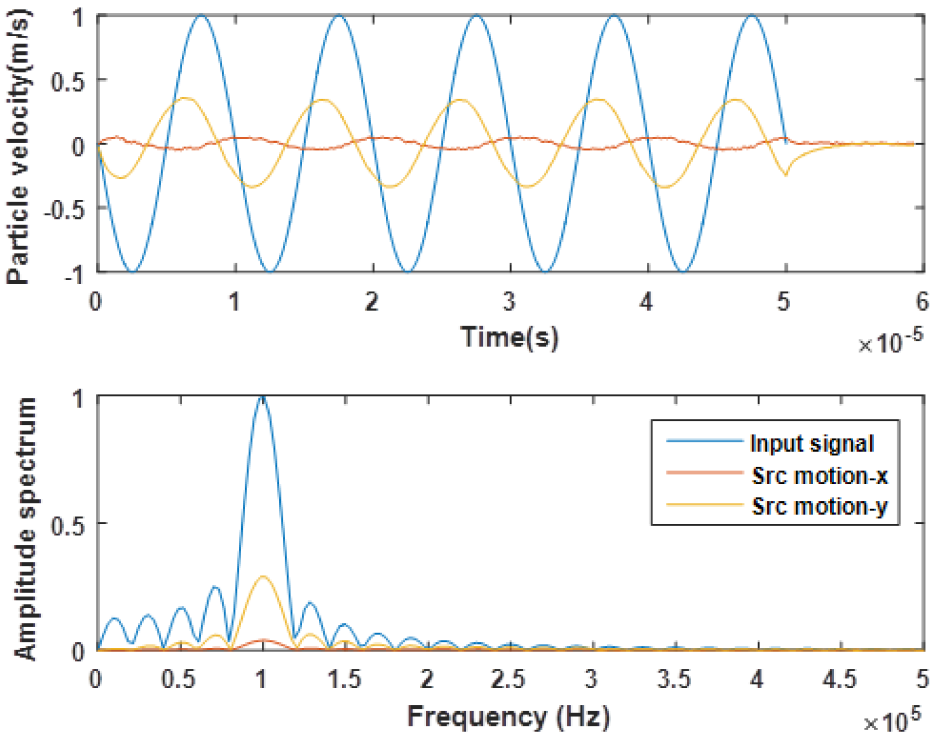

Figure 4.11: The input signal and the response of the recipient, the source particle motion, in (a) time and (b) frequency domain.

The excitation is applied in the vertical direction. However, both horizontal and vertical motions are observed which is due to the random packing and feedback between particles. Figure 4.12 shows the particle arrangement around the source area. The asymmetric distribution and the difference in size of the adjacent particles make the source particle motion deviate from the prescribed vertical direction. It has a slight rightward motion along the horizontal direction. The random packing also influences the vertical component. Different from the input standard sine waveform which has the same amplitude in peak and trough, the vertical components have a larger peak than trough amplitude and display a phase advance. Also the source particle slowly returns to equilibrium instead of coming to a full stop after the applied excitation is terminated.

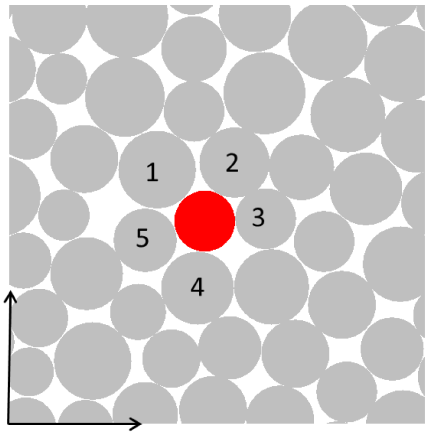

Figure 4.12: Zoomed-in image of Figure 4.1a showing random packing around the source particle (red).

Despite of these modifications of the source waveform, the frequency components are well preserved (Figure 4.11b); the peak frequencies are at the same location, 100 kHz. It also shows that the input signal as well as the source particle motion have side-lobes in the frequency domain between 0 to two times the base frequency as expected.

To sum up, the source wave motion in PFC deviates from the input standard sine wave in shape but the peak frequency components are the same. Also, different from the analytic solutions, source motion in PFC is more complex due to the random packing and associated wave scattering.

P- and S-waves

Next I analyze the recorded motion at the farthest receivers R-5 and R-15 shown in Figure 4.9. In both of the receiver recordings (Figure 4.13), the horizontal components (blue curves) are quite small compared to the vertical ones (red curves). This makes sense as the source particle is prescribed with a vertical motion in the first place. So, vertical components are more pronounced and hence are the main subjects in the wave analysis. The vertical motion of R-15 is

quite similar to the source particle (orange line in Figure 4.11a). It starts with a trough, followed by a larger peak. For R-5, the vertical motion starts with a small positive bump, followed by a waveform similar to the source particle. Both of the vertical recordings have the same initiation time, highlighted by red circles. Also, the vertical component at R-5 has a larger amplitude than R-15. The relative amplitudes of R-5 and R-15 can also be observed in the frequency domain (Figure 4.13b). Besides, motions at these two farthest receivers retain the characteristic frequency of the source motion.

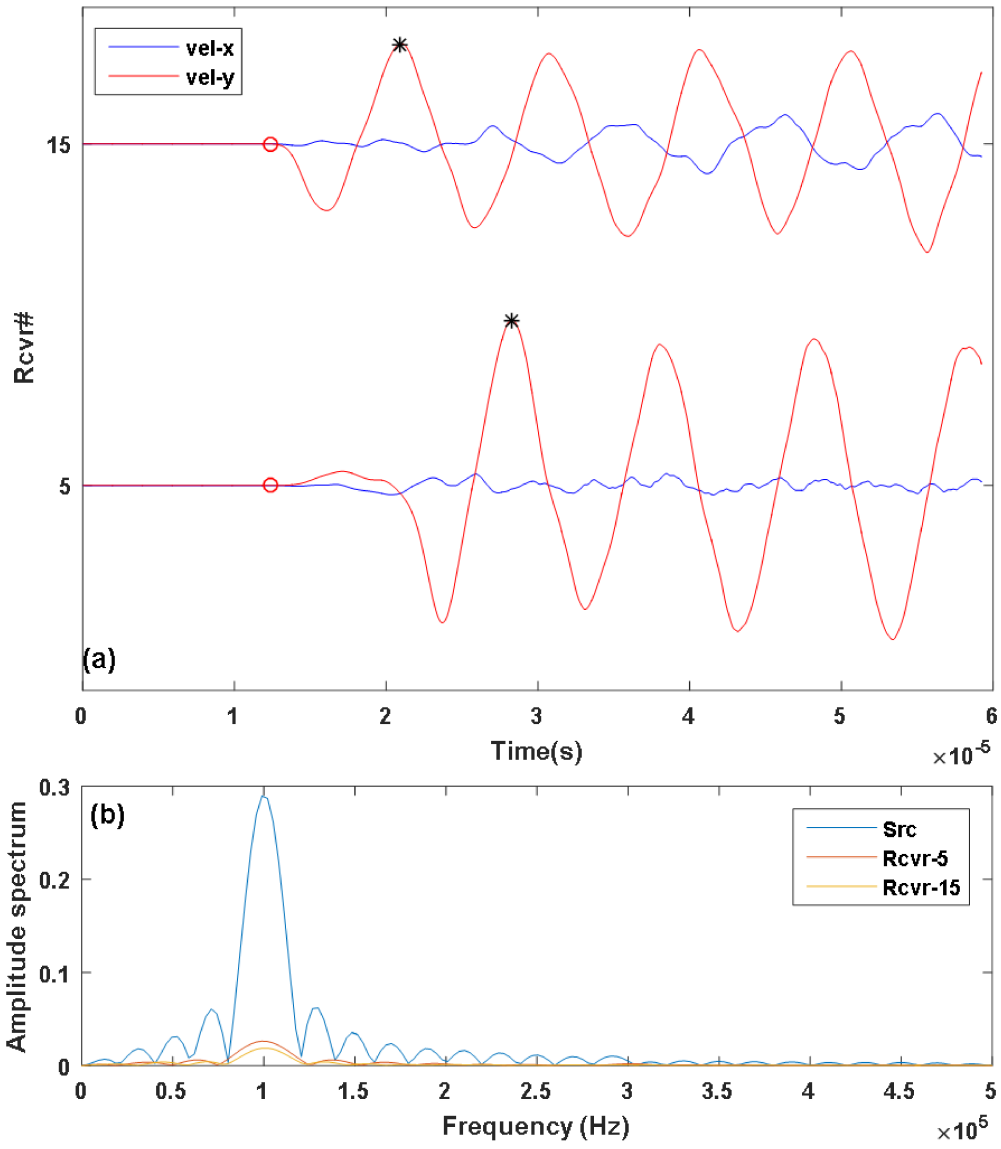

Figure 4.13: (a) Example of particle motion at R-5 and R-15 in time domain. Red circles represent the first arrival of the vertical component. Black asterisks highlight the points used for velocity calculations. (b) Comparison of these two receivers to the source particle in the frequency domain.

According to the geometry of the source-receiver layout (Figure 4.9), the vertical components along the horizontal and vertical directions are attributed to S- and P-waves respectively. Then the wave propagation velocities can be calculated by picking the arrival of the P- and S- waves. However, the sup-

posed S-wave recorded at R-5 has the same arrival time as the P-wave at R-15 (red circles in Figure 4.13). This could be explained by the random packing of the PFC model. R-5 is not perfectly located along the horizontal direction. So the P-wave motion cannot be excluded from the vertical motion recorded at R-5. Then the arrival time cannot be used to calculate the wave velocities. As a result, the first positive peak is chosen instead (black asterisks). The smaller positive peak is due to the fact that R-5 is not perfectly located in the horizontal direction. Also, Hazzard (1998) and Chorney (2014) use the same technique to differentiate P- and S- waves and derive promising results of wave propagation in PFC.

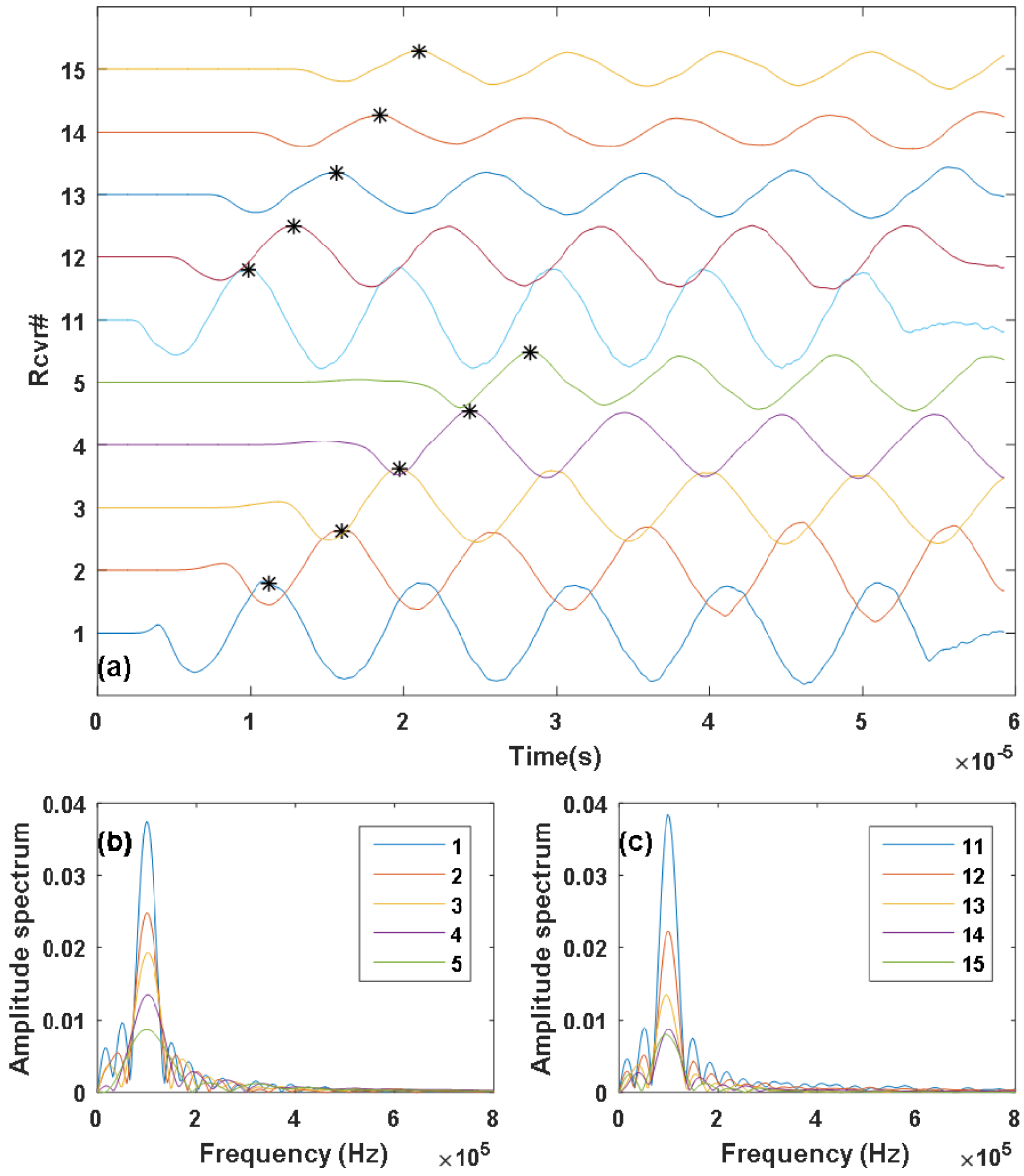

Figure 4.14: (a) Vertical components of R1-5 and R11-15 in time, demonstrating S- and P-wave propagation, respectively. Representation of the vertical components in the frequency domain for (b) R1-5 and (c) R11-15.

Figure 4.14 shows particle velocities recorded at a series of receivers positioned with an increasing distance from the source along both the horizontal (R-1 to 5) and vertical (R-11 to 15) directions. Black asterisks highlight the first peaks which are used to calculate wave velocity. It can be seen the waveform is well preserved as it propagates with a decreasing trend in amplitudes. Also the

propagation velocity is constant, as shown by the constant time separation in arrivals between the equally spaced receivers. As explained earlier, the vertical components at R1-10 represent the S-wave and R11-20 are the P-wave motion. The first positive peaks of these waveforms are picked to calculate the P- and S-wave velocities. It gives an average value of 5783.8 m/s and 3747.4 m/s for P- and S-wave velocities.

The decreasing trend in amplitudes can be attributed to several factors. First is geometric attenuation. The excitation is injected at a single particle. Different from plane waves, this point source creates a spherical wavefront, resulting in decreased energy density on the expanding sphere. Secondly, as damping is included, energy is extracted from the system at every step of calculation. In the frequency domain, it is seen that the amplitude of the dominant frequency declines too. The widening of the spectrum may be the result of the limited length of the recordings. As shown in the time domain, the farthest receiver (green curves) still moves as the fifth period of the sine wave is passing.

Influence of excitation frequency

The influence of excitation frequency is investigated next. The response of a PFC model to wave propagation is investigated on the influence of the excitation frequency. The amplitudes of the excitations are uniform for all simulations. Figure 4.15 shows the recordings at R-16 for different excitation frequencies. The amplitudes of the received signals display a dependency on the frequency. They increase with frequencies, attaining the maximum value at 100 kHz, and then starts to decrease. This might be related to a resonant frequency. PFC model is a multiple mass-spring system in nature which has its own natural frequency. The mass-spring system displays a severer oscillation at a natural frequency, i.e. 100 kHz, than at other frequencies.

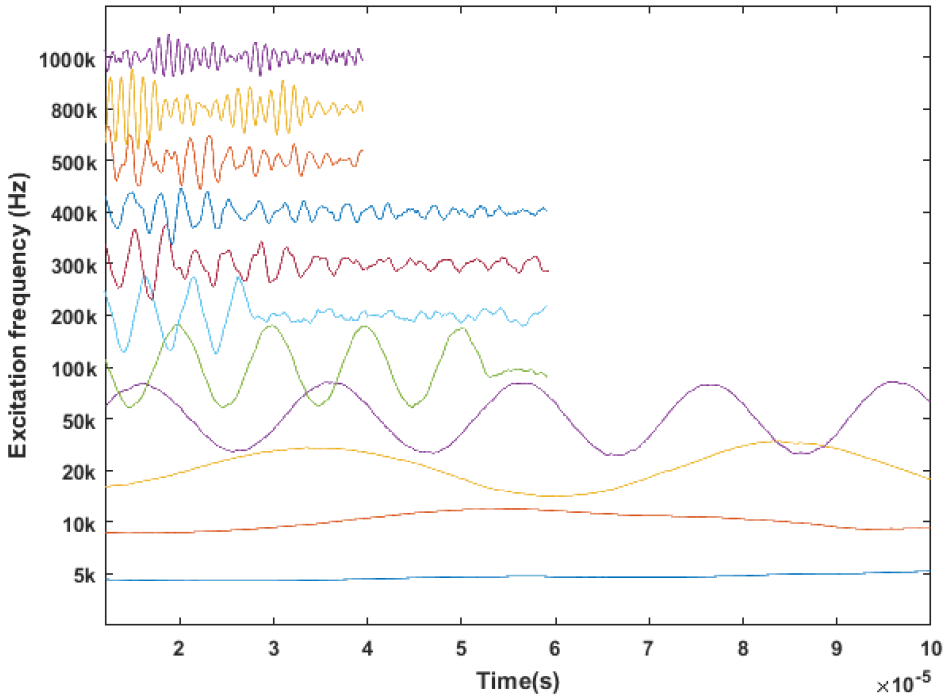

Figure 4.15: Vertical components of velocity recordings at R-16 for different excitation frequencies.

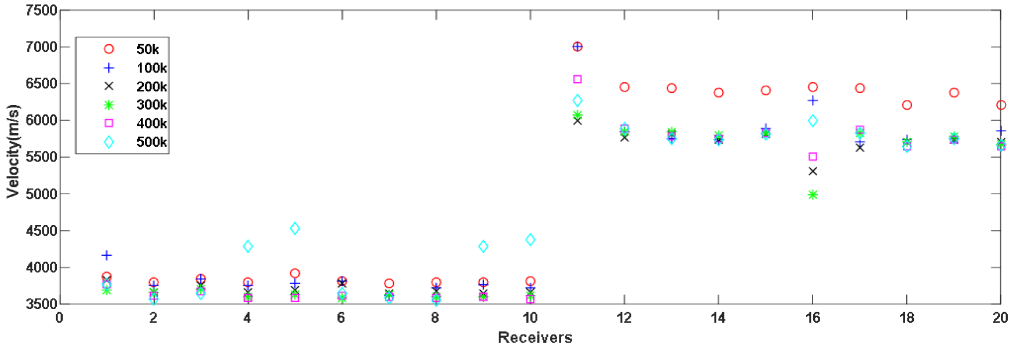

Figure 4.16: Wave velocities calculated at each receiver. R-1 to 10 are used to calculate S-wave velocities and R-11 to 20 give the P-wave velocities. The velocities are measured at a range of excitation frequencies (see legends).

The wave propagation velocity is also calculated for different excitation frequencies using the same peak-to-peak method as in the previous section. Figure

4.16 shows velocities calculated at 20 receivers for different frequency excitations. R-1 to 10 give P-wave velocities and R-11 to 20 offer S-wave velocities. The velocities measured with frequencies equal to 50 kHz and 500 kHz deviate from results for other excitations, especially the S-wave velocities. Also, receivers close to the source (R-1,6, 11, and 16) give more dispersive results. As a result, the velocities for each frequency wave are calculated by averaging results at the other 16 receivers. Table 4.3 shows the P- and S- wavelengths in terms of the average particle diameter (1 mm) for each frequency wave using the average velocities. For most P-waves, the four receivers close to source are located within one wavelength distance, where the near-field influence is quite obvious. So wave velocities using these four receivers are discarded. The inconsistence of 50 kHz simulation can be linked to its long wavelengths. The receivers are located in regions influenced by the near-field wave motion in this case and thus the measured velocities are not acceptable. For 500 kHz simulation results, the deviation is probably due to strong scattering due to high frequency perturbation.

Frequncy (kHz)	Wavelength (average particle diameter)	
	P-wave	S-wave
50	111	66
100	55.3	33.1
200	27.6	16.6
300	18.4	11.0
400	13.8	8.3
500	11.1	6.6

Table 4.3: Wavelengths of different excitation waves using the velocity shown in Figure 4.16.

An average wave velocity is derived for different frequency waves. The aver-

age P-wave velocity equals to 5627 m/s and S-wave 3560 m/s. For comparison, the static velocities using elastic parameters given in compression test (Table 4.2) are also calculated, 5525 m/s and 3310 m/s for P- and S-waves respectively. The dynamic velocities measured by simulating wave propagation are larger than static velocities. This can in part explain that lobes of the numerical wavefield are located at a farther distance from the source than analytic solutions (Figure 4.4 and 4.7).

The different excitation frequencies show the existence of dispersion and scattering. Toomey and Bean (2000) show that wave propagation in discrete systems is dispersive, that is, the wave speed is a function of the wavelength. Caution should be taken when choosing the excitation frequency in PFC. Generally, a minimum wavelength equal to 10 particles is used (Toomey and Bean, 2000; Chorney, 2014). Also, high frequency waves cause strong scattering.

4.5 Conclusions

1. A comparison of analytic and numerical simulations of the displacement and stress patterns due to a single vertical force shows that both produce comparable results. The random grid causes however wave scattering producing more complex stress and displacement patterns. Dispersion and attenuation is also important contrary to the analytical solutions for a homogeneous, isotropic medium.

2. The discrete model is a multiple spring-mass system having its natural frequency. The mass-spring system displays a severer oscillation at a natural frequency than at other frequencies. A discrete model can be excited in an efficient way by using the natural frequency.

3. The dynamic velocities are calculated by initiating wave propagation. It is found the measured velocities are stable at a certain range of frequencies. The dynamic velocities are found larger than the static velocities calculated from elastic constants.

Chapter 5

Radiation patterns of acoustic emissions and dynamic triggering

5.1 Introduction

In seismology, a large earthquake is generally followed by a series of aftershocks and they are found to have a preferential spatial pattern that could be used in the analysis of earthquake clusters in time and space and their possible interactions (Freed, 2005; King et al., 1994). Microseismicity deals with smaller-magnitude events. Each event is often interpreted as independent and uncorrelated to neighbouring ones. In reality, both the rock deformation (static stresses) and transient wave motion (dynamic stresses) associated with microseismic events add to the stress field together with the external forces (fluid injection). The study of the phenomenon of triggering can help in two ways: to promote local failure for more effective treatments and suppress unwanted seismicity for safety.

Vasudevan and Eaton (2011) calculate the static stress changes due to microseismic events and show the subsequent ones concentrate in regions where the static stress promotes failure. How about the dynamic stresses? Are dynamic stresses capable of inducing new failure? If so, how do they control the occurrence of the new failures? To answer these questions, the dynamic triggering of acoustic emissions during a numerical compression test is studied. The numerical method used is called the bonded-particle method, where crack development can be tracked and analyzed independently. First, we stimulate a major event and then simulate two runs on the same model, a static and a dynamic run using respectively a high and low damping factor to eliminate or encourage transient waves. The acoustic emissions are analyzed in terms of quantity, spatial distribution and source mechanisms to highlight the influence of dynamic wave propagation. Then, the stress changes due to a major event are computed and compared to the occurrence of the next few events. If a correlation exists, it implies a causative relation between the major event and the subsequent ones.

5.2 Theory and methodology

The source mechanism of real events, including earthquakes, microseismicity and acoustic emissions, is much more complicated than a single force as used in the previous chapter. Seismologists use the moment tensor to quantify the source mechanism of events. This is described first. Then the computational algorithm for moment tensors in PFC is presented. Next, with the moment tensor representation, the analytic solution of the dynamic stresses associated with an event characterized by an arbitrary moment tensor is derived. The dynamic stress cannot be used directly in determining the occurrence of failure as the bond force is the direct indicator determining if a bond fails or not. As

a result, the criterion most commonly used in seismology, the Coulomb failure function (CFF), is adapted in the bonded-particle method to estimate the likelihood of failure, that is, bond breakages. After the theoretical work, the model and analysis methodology is outlined.

5.2.1 Moment tensor

It is common to employ the body-force equivalent as a proxy for the actual forces of an earthquake. It is a useful tool in earthquake studies which generally involve discontinuities so that equations of continuum theories can be directly used. The body-force equivalent can be represented in terms of force couples. A force couple is made up of two parallel forces that are equal in magnitude, opposite in sense, and displaced by a certain distance called the arm. For three-component forces and three possible arm directions, there are nine basic couples (Figure 5.1). The quantification of the mechanism of the earthquake is a second-order tensor, called the moment tensor:

$$\boldsymbol{M} = \begin{bmatrix} M_{11} & M_{12} & M_{13} \\ M_{21} & M_{22} & M_{23} \\ M_{31} & M_{32} & M_{33} \end{bmatrix}, \tag{5.1}$$

where the component M_{pq} $(p, q = 1,2,3)$ represents the strength of the force couple along the direction of ξ_p with the arm in the ξ_q direction. The source coordinate system ξ_i (i=1,2,3) is used to distinguish from the general coordinates x_i (i=1,2,3), which are often referred to as the observation points. Similar to the stress and strain tensor, a moment tensor has its principal values. Generally, the moment tensor is represented by its principal components. These components correspond to force couples whose forces and arms have the same orientation, called vector dipoles. For earthquakes, the moment tensor is de-

rived by inversion of the recorded seismic data (Gilbert, 1973).

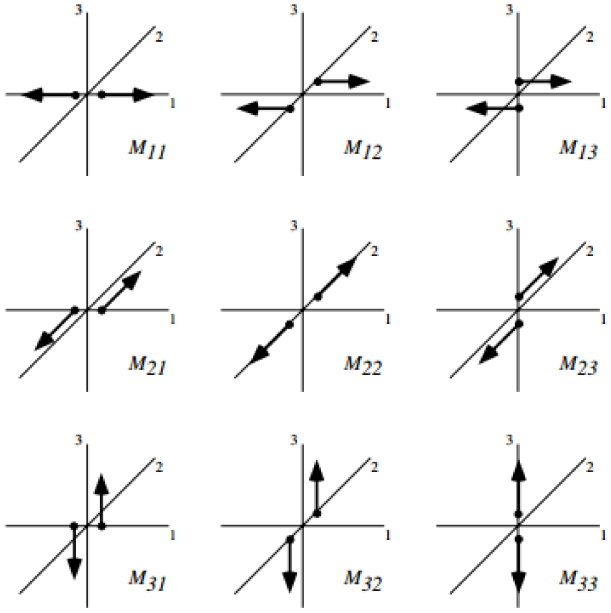

Figure 5.1: The components of the moment tensor represent force couples (Shearer, 2009).

5.2.2 Analytic solutions of the displacement and stress field induced by failures in PFC

Moment tensor algorithm in PFC

In PFC, failure can also be represented by a moment tensor. The moment tensor M_{pq} is expressed by Julian et al. (1998) as:

$$M_{pq}(t) = \iiint_V f_p(t) r_q \, dV, \tag{5.2}$$

where $f_p(t)$ is the force per unit volume in the p-th direction and r_q is the q-th component of the distance between the force and the source centroid. The moment tensor component M_{pq} is the integral of the moment of force, or torque,

$f_p r_q$ over the source volume, V.

As PFC is a discrete system, the integral in the moment tensor expression becomes a summation. Contact forces and particle locations around bond breakages are tracked to calculate the moment tensor by Hazzard and Young (2004) as:

$$M_{pq}(t) = \sum \triangle f_p(t) r_q, \tag{5.3}$$

where $\triangle f_p(t)$ is the p-th component of the change in contact forces from that prior to bond breakages, and r_q is the distance vector component in the q-th direction between the contact and the event centroid. The summation is over all contacts in the event area.

Analytic solutions of the stress field

Following the same strategy as in the previous chapter, the analytical stress field is derived from its displacement field (Equation 4.6). The displacement field due to an arbitrary source characterized by a moment tensor M_{pq} can be represented by the contribution of the nine force couples. For each component M_{pq}, the displacement v_n is the linear summation of the contribution of two parallel forces, identical in magnitude F_p and opposite in sense, displaced by a distance $\triangle l_q$ along the q-th direction shown in Figure 5.1:

$$v_n = u_n^{(2)} - u_n^{(1)}, \tag{5.4}$$

where $u_n^{(i)}$ (i=1,2) represents the displacement due to a single force F_p (Equation 4.1). As the arm $\triangle l_q$ is infinitesimal, the right hand of Equation 5.4, the difference of u_n, can be converted to a differential of u_n with respect to the source coordinate ξ_q:

$$v_n = \triangle l_q \frac{\partial}{\partial \xi_q} u_n. \tag{5.5}$$

Inserting Equation 4.1 which shows the displacement u_n due to a single force F_p is the convolution of the single force with the Green's function G_{np}, the right hand side becomes:

$$v_n = \triangle l_q \frac{\partial}{\partial \xi_q}(F_p * G_{np}). \tag{5.6}$$

As the single force F_p is independent of the source coordinates ξ_i, F_p can be removed from the spatial differential sign and thus:

$$v_n = \triangle l_q F_p * \frac{\partial G_{np}}{\partial \xi_q}. \tag{5.7}$$

According to the definition of the moment tensor (Equation 5.2), the first term $\triangle l_q F_p$ equals the moment tensor component M_{pq}. Then it follows that the displacement v_n due to a source characterized by M_{pq} is the convolution of the moment tensor and the spatial derivatives of the Green's function G_{np} with respect to source coordinates ξ_q. Aki and Richards (2002) give the expression of the displacement due to the moment tensor M_{pq} in a homogeneous, isotropic, elastic and unbounded medium:

$$\begin{aligned}
v_n(\mathbf{x},t) &= M_{pq} * G_{np,q} \\
&= \frac{1}{4\pi\rho}\frac{1}{r^4}\left(15\gamma_n\gamma_p\gamma_q - 3\gamma_n\delta_{pq} - 3\gamma_p\delta_{nq} - 3\gamma_q\delta_{np}\right)\int_{\frac{r}{\alpha}}^{\frac{r}{\beta}} \tau M_{pq}(t-\tau)d\tau \\
&+ \frac{1}{4\pi\rho\alpha^2}\frac{1}{r^2}\left(6\gamma_n\gamma_p\gamma_q - \gamma_n\delta_{pq} - \gamma_p\delta_{nq} - \gamma_q\delta_{np}\right)M_{pq}\left(t-\frac{r}{\alpha}\right) \\
&+ \frac{1}{4\pi\rho\beta^2}\frac{1}{r^2}\left(-6\gamma_n\gamma_p\gamma_q + \gamma_n\delta_{pq} + \gamma_p\delta_{nq} + 2\gamma_q\delta_{np}\right)M_{pq}(t-\frac{r}{\beta}) \\
&+ \frac{1}{4\pi\rho\alpha^3}\frac{1}{r}\left(\gamma_n\gamma_p\gamma_q\right)\dot{M}_{pq}\left(t-\frac{r}{\alpha}\right) \\
&+ \frac{1}{4\pi\rho\beta^3}\frac{1}{r}\left(-\gamma_n\gamma_p\gamma_q + \gamma_q\delta_{np}\right)\dot{M}_{pq}(t-\frac{r}{\beta}),
\end{aligned} \tag{5.8}$$

where v_n is the n-th component of the displacement at $\boldsymbol{x}$. On the right side,

γ_i is the direction cosine with the i-th axis of the observation point $\boldsymbol{x}$, r is the source-receiver distance, α, β are the P- and S-wave speed and ρ is the density of the medium, δ_{ij} is the Kronecker symbol. The dot represents the temporal derivative and the comma in the subscript means a spatial derivative.

Equation 2.13 sets up the relation between the dynamic stress and the displacement through the spatial derivative of the displacement. To derive the expression of the dynamic stress due to an event characterized by M_{pq}, the derivatives of the displacement v_n with respect to the observation coordinates x_m is necessary.

$$\begin{aligned} v_{n,m} = \frac{\partial v_n}{\partial x_m} = & \frac{1}{4\pi\rho}\frac{1}{r^5}C_N \int_{\frac{r}{\alpha}}^{\frac{r}{\beta}} \tau M_{pq}\left(t-\tau\right)d\tau \\ & + \frac{1}{4\pi\rho\alpha^2}\frac{1}{r^3}C_{IP1}M_{pq}(t-\frac{r}{\alpha}) + \frac{1}{4\pi\rho\beta^2}\frac{1}{r^3}C_{IS1}M_{pq}(t-\frac{r}{\beta}) \\ & + \frac{1}{4\pi\rho\alpha^3}\frac{1}{r^2}C_{IP2}\dot{M}_{pq}(t-\frac{r}{\alpha}) + \frac{1}{4\pi\rho\beta^3}\frac{1}{r^2}C_{IS2}\dot{M}_{pq}(t-\frac{r}{\beta}) \\ & + \frac{1}{4\pi\rho\alpha^4}\frac{1}{r}C_{FP}\ddot{M}_{pq}(t-\frac{r}{\alpha}) + \frac{1}{4\pi\rho\beta^4}\frac{1}{r}C_{FS}\ddot{M}_{pq}(t-\frac{r}{\beta}), \end{aligned} \tag{5.9}$$

where double dots denote the second-order derivative of the variable and the

parameters in the above equation are given by:

$$\begin{bmatrix} C_N \\ C_{IP1} \\ C_{IS1} \\ C_{IP2} \\ C_{IS2} \\ C_{FP} \\ C_{FS} \end{bmatrix} = \begin{bmatrix} -105 & 15 & 15 & 15 & 15 & 15 & 15 & -3 & -3 & -3 \\ -45 & 6 & 6 & 6 & 6 & 6 & 5 & -1 & -1 & -1 \\ 45 & -6 & -6 & -6 & -6 & -6 & -9 & 1 & 1 & 2 \\ -10 & 1 & 1 & 1 & 1 & 1 & 0 & 0 & 0 & 0 \\ 10 & -1 & -1 & -1 & -1 & -1 & -3 & 0 & 0 & 1 \\ -1 & 0 & 0 & 0 & 0 & 0 & 0 & 0 & 0 & 0 \\ 1 & 0 & 0 & 0 & 0 & 0 & -1 & 0 & 0 & 0 \end{bmatrix} \begin{bmatrix} \gamma_n\gamma_p\gamma_q\gamma_m \\ \gamma_p\gamma_m\delta_{np} \\ \gamma_m\gamma_n\delta_{pq} \\ \gamma_p\gamma_n\delta_{mq} \\ \gamma_n\gamma_q\delta_{pm} \\ \gamma_p\gamma_q\delta_{mn} \\ \gamma_m\gamma_q\delta_{np} \\ \delta_{nq}\delta_{pm} \\ \delta_{qq}\delta_{mn} \\ \delta_{mq}\delta_{np} \end{bmatrix} \tag{5.10}$$

Equation 4.1 and 5.9 give the analytic stress field due to a source quantified by a moment tensor M_{pq}. The numerical solution of the stress field will be derived by the measurement-based algorithm in PFC as outlined in Chapter 3.

5.2.3 Bond failure functions

The stress state can be used to estimate the likelihood of failure. In seismology where an earthquake is commonly a slippage on an incipient fault plane, the Coulomb failure criterion is used to characterize shear failure in rocks (Jaeger et al., 2009). The normal and shear stresses on the fault plane must satisfy conditions analogous to those of the shear slippage on a preexisting plane. So the Coulomb failure function (CFF) is presented to evaluate the possibility of aftershocks on neighbouring faults.

CFF is a function of the stress state and the friction coefficient according to the Coulomb theory. It represents the stability of a fault and it is a relative

value of two states, before and after a main earthquake. So CFF can be used to describe the influence of an earthquake on a nearby incipient fault in terms of its stability. A positive value means a less stable fault, closer to failure and a negative value represents the fault is stable and less likely to fail. Figure 5.2 gives an example of a Coulomb stress map associated with the 1979 $M_L = 5.5$ Homestead Valley earthquake overlain with the aftershock distribution (King et al., 1994). It shows positive (warm color) and negative (cold color) stress regions. The correlation of the aftershock locations and positive Coulomb stress changes demonstrates the success of the Coulomb stress as an indicator of aftershock location predictions.

In PFC, the failure mechanism is often different from the Coulomb theory as

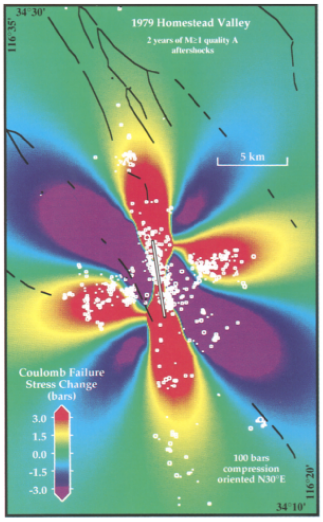

Figure 5.2: Calculated coseismic Coulomb stress changes and observed aftershocks (white circles) associated with the 1979 $M_L = 5.5$ Homestead Valley earthquake (from King et al. (1994)). The correlation of positive Coulomb stress changes and spatial locations of aftershocks demonstrates the usefulness of calculating Coulomb stress changes.

tensile failure is dominant. A bond is like an elastic beam connecting two particles. When either the tensile or shear stresses acting on the bond periphery exceed the strength values, the bond breaks. The normal and shear components of the bond force are proportional to the normal and shear stresses at

the bond respectively. So the relative changes of tensile and shear bond forces are calculated for the likelihood of bond failure. The bond force is calculated as the traction on the contact plane according to the particle-particle geometry (Figure 3.2a) using Equation 2.3. Then the normal and shear components can be easily derived by a dot product operation applied on the traction and the unit normal or tangent vector.

5.2.4 Model setup and workflow

A 126x62.3 mm Lac du Bonnet rock model composited by 1886 particles is constructed using the microproperties listed in Table 4.1. The average particle diameter is 1 mm. After calibration, the model is first confined at 10 MPa stress and loaded with an increasing axial stress until 90% of its peak strength is achieved (red dashed line in Figure 5.3b). Also shown are cracks that form before (Figure 5.3c) and after (Figure 5.3d) this point. The confining and axial stresses will be fixed from this point on. Then several particles in the center (yellow particles in Figure 5.4) are chosen and the bonds between them are broken and thus tensile (blue) or shear (red) cracks form depending on the original bond forces. As compression is dominant during the long-term loading, this is mainly a closing event and considered as the major failure event. The objective is to monitor stress changes due to this event, and look for relationships between the following new cracks and this one.

Two approaches are used here. The first method is to conduct two simulations with different damping parameters after the major event occurs. Both simulations before the major event use the same stress history and damping parameter 0.0157 to simulate a realistic attenuation of the granite (Q=100). This method gives a direct comparison between the static and dynamic stress changes due to the same event. This so-called dynamic run is done with a low

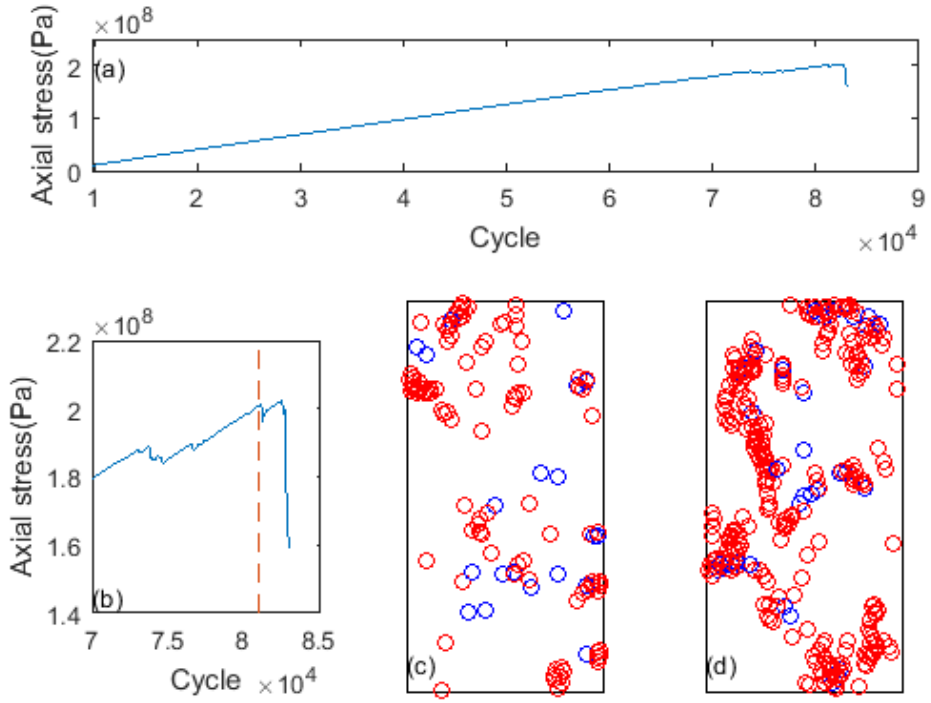

Figure 5.3: (a) History of the axial stress during a confined (10 MPa) compression test, (b) zoom-in image around the peak strength and red dashed line highlights the time point when the main event is stimulated, and cracks that form (c) before and (d) after this specific time point. Red cracks are tensile and blue are shear.

damping parameter (0.0157) so a large part of the released energy from the bond failures are converted into kinetic energy and thus elastic waves. Next a second run is done using the same damping parameter up to the main event, but then the damping is significantly increased to 0.7. A high damping parameter ensures most of the energy stored at the bonds are absorbed after the bond breaks. There is less elastic wave propagation throughout the system. It can be seen as if only static stress changes are involved, and it is called the static run. The cracks formed in these two runs are compared in terms of both quantities and locations to examine the effect of dynamic and static stress changes after a major failure event.

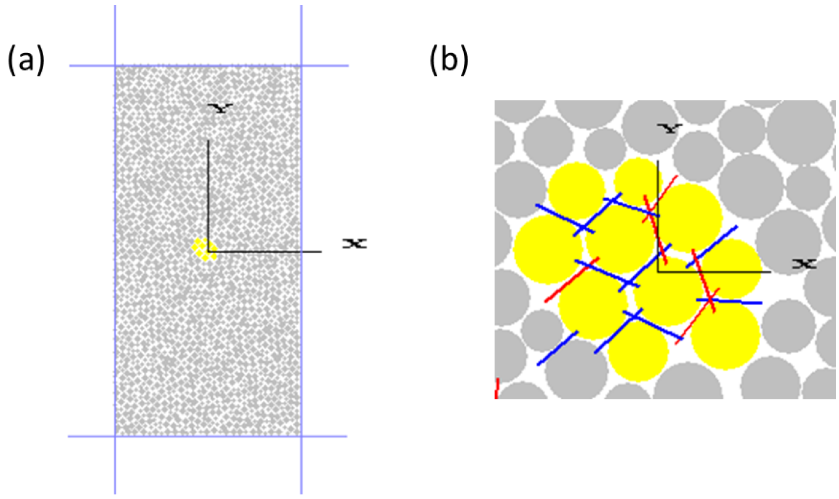

Figure 5.4: (a) Geometry of the model: the source particles are highlighted in yellow and (b) zoom-in image for the source region. Cracks are shown in short lines: red are tensile cracks and blue represents shear cracks.

The second approach deals with the influence of the dynamic stress directly, so it is run in a dynamic mode with low damping. The moment tensor algorithm (Equation 5.3) gives the source mechanism of the major event, which is then used to calculate the analytical stress field. The resulting stresses are resolved into normal and shear forces, the bond failure functions, on the contact plane. This reveals directly the relative stress changes due to wave propagation. Similar to the Coulomb failure function, they can be used to evaluate the probability of bond failures. Finally, the analytic results are compared with newly formed cracks to determine the influence of the dynamic stress.

5.3 Results and interpretation

5.3.1 Validation of the analytic expression

To begin with, the analytic expression of the spatial derivatives of the displacement by an arbitrary source characterized by a moment tensor (Equation 5.9)

is checked for its validity. Our results are compared with the semi-analytic solution using a numerical operator on the analytic solution of the displacement values. The semi-analytic solution are computed from the analytic displacement field using Aki and Richards's expression (Equation 5.8) by a first-order finite-difference approximation. The same source is used to calculate the spatial derivatives of the displacement using the analytic expression (Equation 5.9). The model is a homogeneous, isotropic, elastic medium with the same size and properties (Table 4.1) as the PFC model described above. The source injected in the center is an explosive source (Figure 5.5):

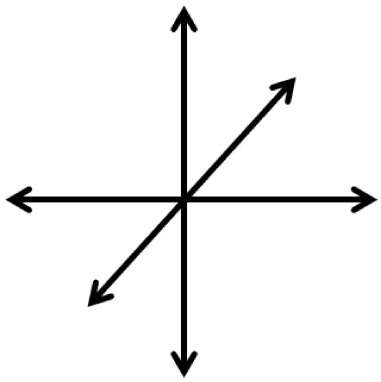

Figure 5.5: Force equivalents of the explosive source which is composed by three vector dipoles shown in Figure 5.1.

$$\begin{bmatrix} M_1 & 0 & 0 \\ 0 & M_1 & 0 \\ 0 & 0 & M_1 \end{bmatrix} \tag{5.11}$$

where M_1 is one cycle of a cosine function.

Figure 5.6 shows the contours of the spatial derivatives of the displacements. The results obtained by two different methods, namely the semi-analytic (left columns) and analytic (right columns) methods, show strong similarities. The

contour is composed by three loops of alternating lobes. The lobes in terms of location and shape are determined by the radiation pattern of the displacement field. These three loops with alternating polarities correspond to the input source, one cycle of a cosine wave. The noisy part in the center of the analytic solution is due to the generation of fluctuations on the order of machine precision. The consistency of the results by these two methods indicate the accuracy of our analytic expression of the spatial derivatives of the displacements and hence the stress calculations using Equation 2.9 and 2.12 in the next section.

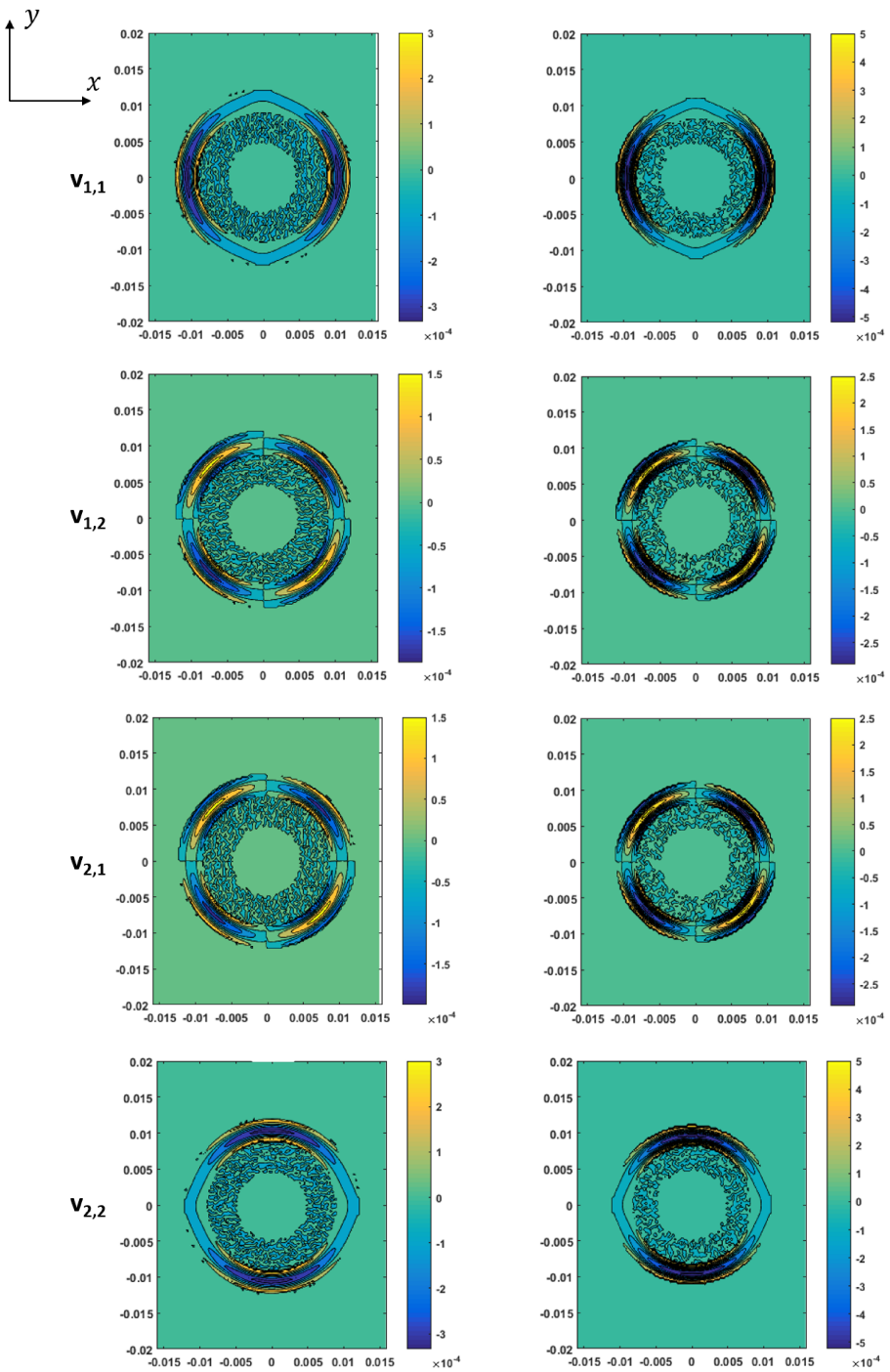

Figure 5.6: Comparison between the spatial derivatives of the displacements obtained by our analytic expressions (right) using Equation 5.9 and semi-analytic results (left) derived from the first-order finite-difference approximations. From top to bottom, the panels correspond to $v_{1,1}$, $v_{1,2}$, $v_{2,1}$ and $v_{2,2}$.

5.3.2 Source mechanism of the main event

The experiment is divided into two stages separated by a relatively large event, called the main event. The first stage is a confined compression test with a confining stress equal to 10 MPa. This stage terminates when the axial stress reaches 90% of its peak strength (Figure 5.3b), followed by the main event. Next the axial and confining stresses are fixed in the second stage to observe the influence of the main event.

The main event that will be analyzed in the following simulations is composed of 14 bond failures, including 5 tensile and 9 shear failures (Figure 5.4). Figure 5.7 shows the moment tensor solution using the algorithm from Hazzard and Young (2004). The moment tensor is illustrated by equivalent forces. The two pairs of arrows correspond to the principal values of the moment tensor. The directions and lengths of the arrows represent the orientations and magnitudes of the principal stresses. This event grows with time in magnitude, and weakens after 7 calculation steps. At first, it is a closing event along a sub-vertical direction. This is likely because the axial stress is the dominant stress sustained in the model. The compression in the axial direction forces the particles in between to move to the sides, which corresponds to tension. The amount of tension (opening) and the minimum principal stress increases with time, although it remains a closing event in general. The orientation of the maximum principal stress also changes with time. It is sub-vertical first, then becomes more vertical, and finally back to sub-vertical again. The main event evolves to a more shearing-like event in the last few steps.

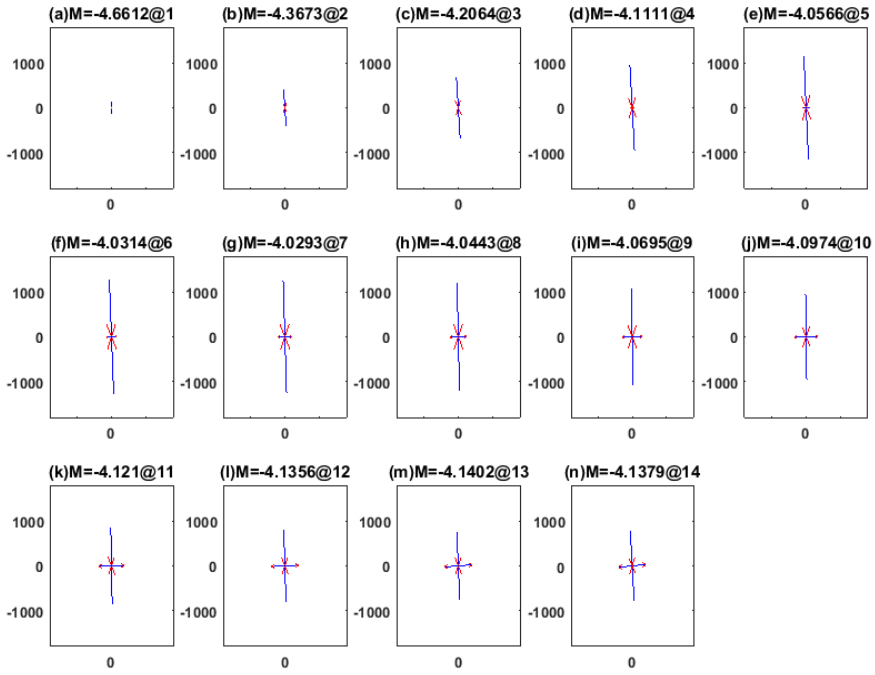

Figure 5.7: Evolution of the moment tensor of the main event. The moment tensor solution is represented by two sets of arrows corresponding to the principal values of the moment tensor indicating respectively compression and extension depending on the direction of the arrows.

5.3.3 Approach 1: static and dynamic simulations

The influence of the major event is first explored by conducting two simulations in the form of static and dynamic runs. Both simulations allow for spontaneous bond failures and are run for 70 steps after the major event. Figure 5.8 shows the stress curve for the dynamic and static run, with a full compression test. It clearly shows the dynamic run experiences a larger stress drop than the static run in response to the forced main event. Then the cracks formed in these two runs are further compared in terms of quantities and locations of subsequent smaller failures to compare the effect of dynamic and static stress changes after a major failure event.

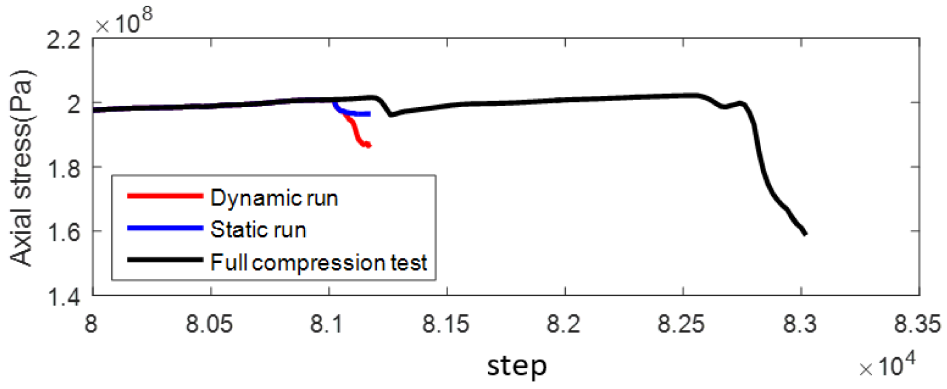

Figure 5.8: Stress curves for the dynamic (red) and static (blue) run, with a full compression test (black).

First, the quantity of cracks formed in the two modes are examined. Figure 5.9 shows the time and location of the newly formed cracks together with particle velocities for both runs. The velocity used is the root mean square of the x- and y- particle velocities. The particle motion is stronger in the dynamic run in terms of extent and strength due to the additional released strain energy converting into kinetic energy compared with the static run. In other words, more wave motion occurs in the dynamic run. More cracks have formed in the dynamic mode during the same simulation time, namely 15 and 2 for respectively the dynamic and static runs in the analyzed 70 steps. It is worth noting that the two cracks formed in the static run (Figure 5.9d and e) also occurred in the dynamic run, but at an earlier time (Figure 5.9b). These two cracks are found to be critically stressed before the main event. The stresses at these bonds exceed 90% of their bond strengths. So they fail in the static run with a smaller stress disturbance as well as in the dynamic run with an apparently larger stress perturbation. The dynamic waves cause the same bond failures as in the static run. They also cause bond breakages that would not otherwise have occurred.

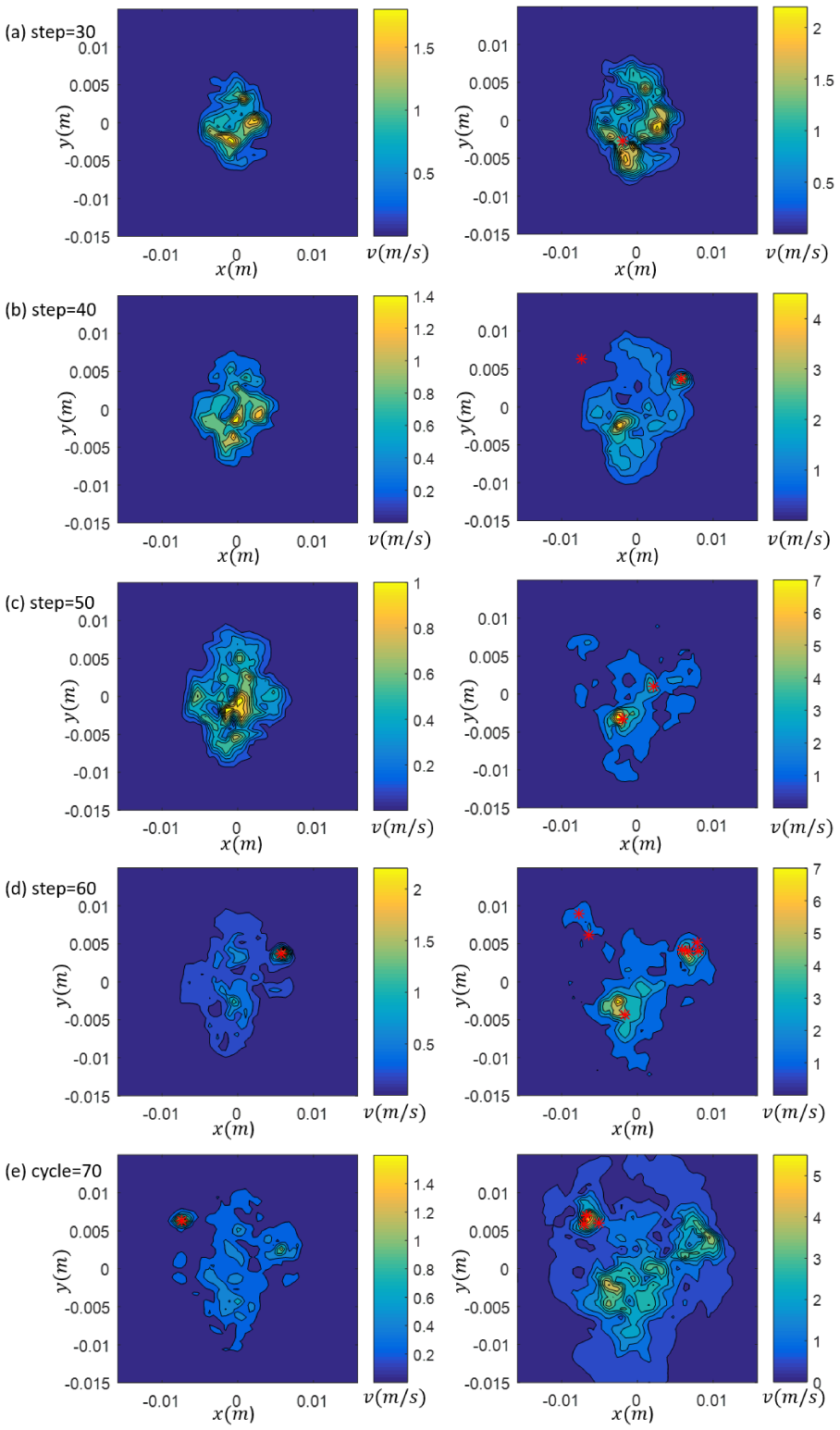

Figure 5.9: Cracks (red asterisks) formed in the static (left column) and dynamic (right column) modes in 70 cycles after the main event overlain with contours of particle velocities (note different color scales in each figure).

The locations of cracks are easily discerned in Figure 5.9. For the dynamic run, cracks form at positions further from the main event in the first 40 cycles (Figure 5.9a and b). In the following cycles, new cracks occur at the vicinity of the existing cracks instead of further positions. This relates to two aspects. To begin with, a dynamic wave is propagating outwards with a larger wavefront. The dynamic stress due to the main event declines because of geometric spreading (attenuation), becoming less effective in causing bond failures at a larger distance. Meanwhile, the cracks that form in the early stage emit new dynamic energy, which may contribute ultimately more to the overall stress changes. So new cracks concentrate around the existing cracks to form clusters. With increasing simulation time, more cracks are expected to occur around the old ones. Figure 5.10a shows bond failures at 90 cycles. The old cracks (first 70 cycles) are shown in red for tensile and blue for shear. New cracks (green and black) which are formed in the next 20 cycles are observed to locate around the old ones as expected.

Figure 5.10b shows the source mechanism of the new events in the dynamic run. Cracks form close in time and space are registered as events. The source mechanism varies with each event. Closing, opening, shearing and hybrid mechanisms are all observed. The source mechanism is decided by the in-situ stress which is a combination of the stress from the main event, and most importantly, the initial stress field established by the long-term loading due to the boundary stresses. This also holds for the static run which shows fewer bond failures (Figure 5.11). Although fewer cracks are formed, the source mechanisms show similarities with those in the dynamic run.

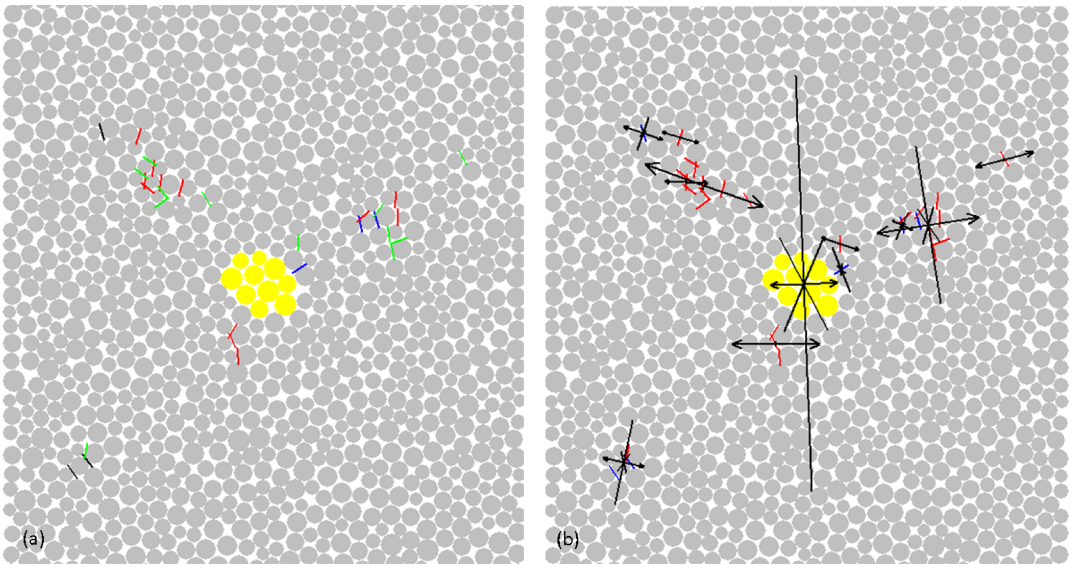

Figure 5.10: (a) Cracks formed in the dynamic run at cycle = 90. The old cracks in the first 70 cycles are shown in red and blue for tensile and shear cracks respectively. New cracks are represented in green for tensile and black for shear cracks. (b) Source mechanism of the new events subsequent to the main event. The representation of the source mechanism follows Figure 5.7. Also shown are tensile cracks in red and shear cracks in blue.

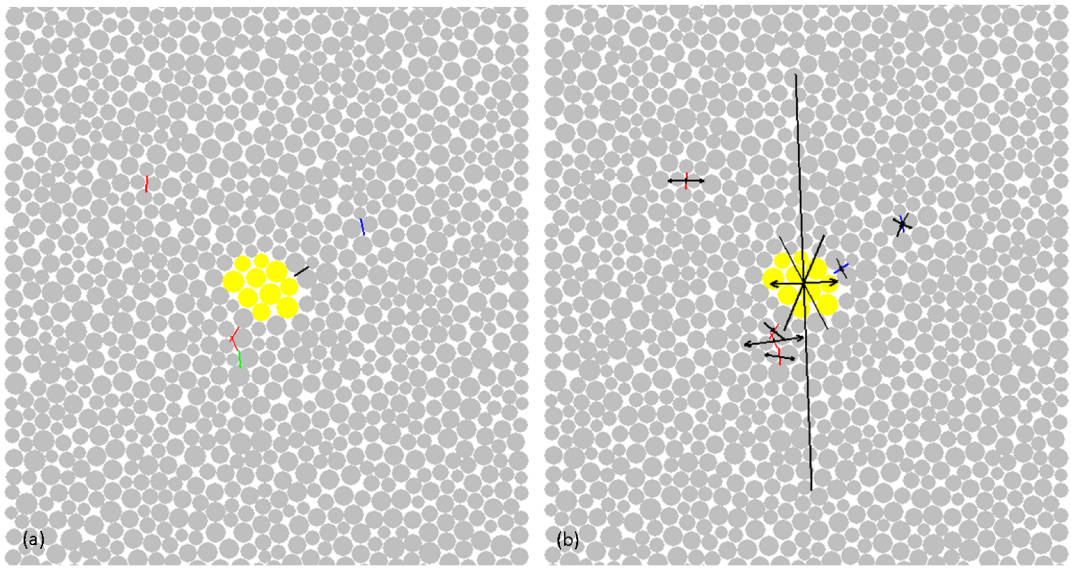

Figure 5.11: (a) Cracks formed in the static run at cycle = 90. (b) Source mechanism of the new events subsequent to the main event. Same labels as in Figure 5.10.

In this section two modes of simulation were performed and analyzed. The

dynamic run is observed to have more cracks formed than in the static run. Next, the new cracks are analyzed in terms of locations and source mechanisms using the analytically predicted dynamic stresses using Equation 4.1 and 5.9 as outlined above.

5.3.4 Approach 2: dynamic stress field and its correlation with new cracks

The second approach deals with the dynamic simulation. First, the analytic dynamic stress field due to the main event is calculated. Then the stress field influenced by the dynamic stress due to the main event is compared with new cracks that form following the main event.

Analytic and numerical solutions of the stress field

The dynamic stress field is analytically calculated by Equation 4.5 and 5.9. Figure 5.12 shows the analytic solution of stress field due to the main event after 70 cycles, together with the numerical result in PFC. The analytic stresses show again two concentric loops, similar to the stress field due to a single force (Figure 4.6). Each loop is composed of alternating lobes with a 90° periodicity. The symmetrical axises vary with different stress components. The warm color represents tension and cold is compression for the normal stresses.

The stress field at the same time instant measured by PFC using the dynamic run is shown in the bottom panel. The numerical stress field is derived by fixing all the bonds so that no bonds will break. This treatment ensures only the dynamic stress field due to the main event is exhibited. The stress field in PFC is less clear compared with the analytical one due to speckle noise patterns. Also, stresses in the center with large strengths add more discrepancy from the

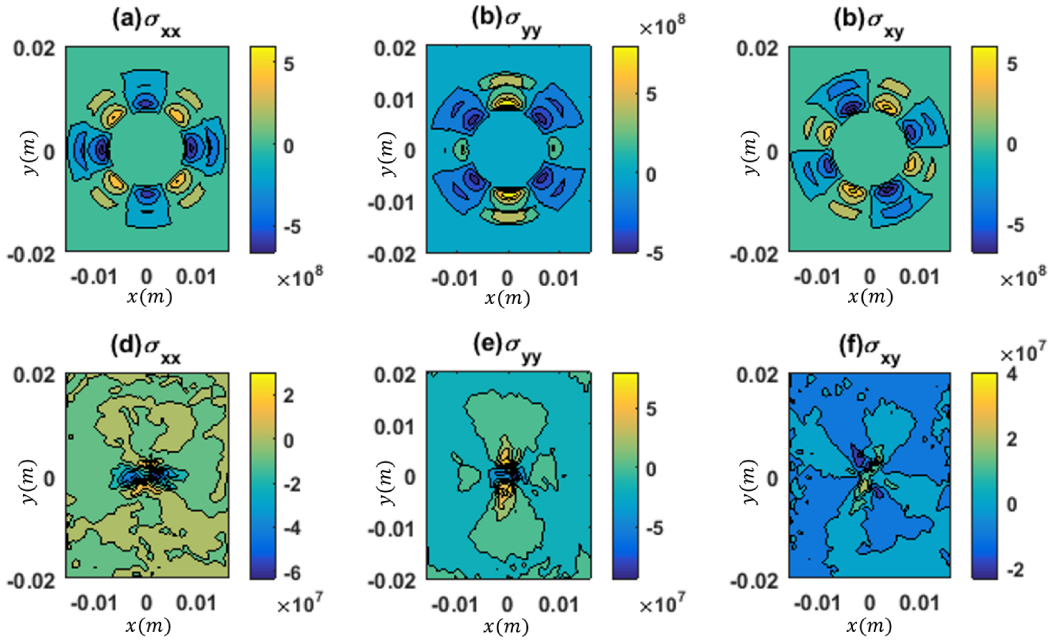

Figure 5.12: Stress field due to the main event at cycle = 70 in terms of normal and shear stresses: (top) analytic and (bottom) PFC results. For normal stresses σ_{xx} and σ_{yy}, positive values represent tension whereas negative ones denote compression.

analytic solution. Unlike a source wave with limited duration (non-zero values) used in the analytic solution (Equation 5.9), particles in PFC are in persistent motion. So the source region shows a strong motion and hence significant stress values. Apart from the source region, PFC results show comparable patterns with respect to polarities and relative strengths with the analytic results. So it is reasonable to use the analytic solutions of dynamic stresses to analyze the crack formations.

Correlation of dynamic stress changes with new cracks

Figure 5.9 shows more cracks have formed due to dynamic wave propagation and they concentrate in a certain regions instead of scattering evenly. The dynamic stress field is further converted into normal and shear forces on con-

tact planes to explain this preferential distribution. Only the tensile cracks are considered here as most cracks during this compression test are tensile.

The calculation of bond forces depends on the stress tensor as well as the contact plane orientations. The random packing creates an almost even distribution of contact plane orientations shown in Figure 5.13a. The orientation is represented by the angle between the unit normal and the x-axis in the positive sense. Though evenly oriented in all directions with regard to all the contacts, the contacts with critical bonds have a preferential orientation. The critical bonds are ones with a relative large load, hence being closer to failure. Compared to others, the critical bonds are more likely to fail so the contacts with critical bonds are considered here. The long-term axial loading has the bonds with a larger load orientated nearly parallel with the maximum principal stress direction. The critical state is set to be 70% of the tensile strength. Figure 5.13b shows that the unit normals for these contacts deviate from the horizontal axis with very small angles. So a unit normal with 10° is used to compute the bond forces.

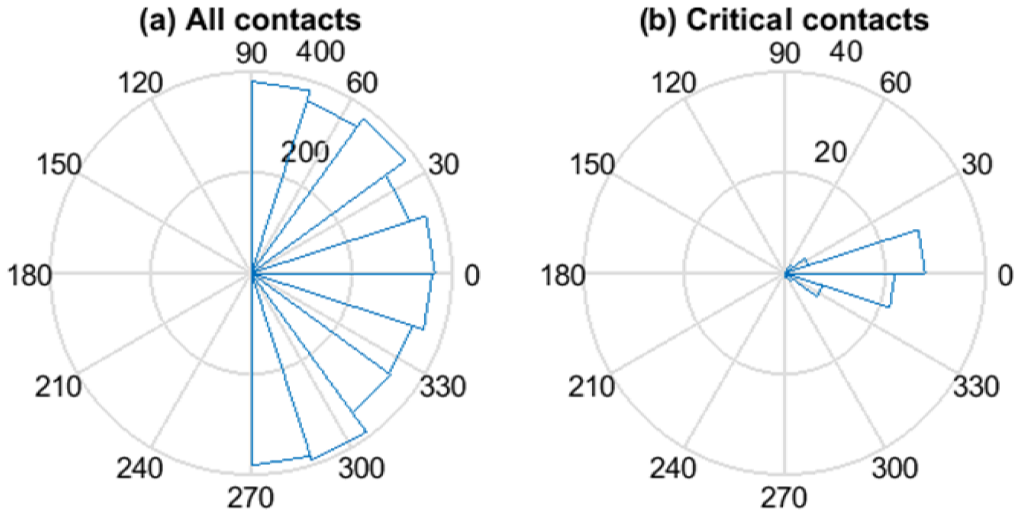

Figure 5.13: Angle histogram of the unit normals for: (a) contact planes between all bonded particles and (b) contact planes for critical bonds whose tensile stress is above 70% of the tensile strength. Vertical contact planes are displayed as 0°.

The analytic stresses are then converted to forces at the bonds in the normal direction by assuming a sub-vertical contact plane, with a unit normal at 10 degrees from horizontal (Figure 5.14). The tensile cracks that form after the main event in the dynamic mode are also shown as red circles. The tensile cracks are found to concentrate in regions where bond forces become more tensile. This implies that the dynamic stresses are indeed responsible for failure at these locations. As the bond force is calculated at 70 cycles after the event while cracks are formed during this time interval, most cracks are located inside the lobes, especially the early ones. Figure 5.15 shows bond forces for a range of contact plane orientations. The angles range from -30° to 30°. Despite the variance of the contact plane orientations, most cracks fall in the regions with tensile force change. The correlation between the dynamic stress and new cracks is thus further confirmed.

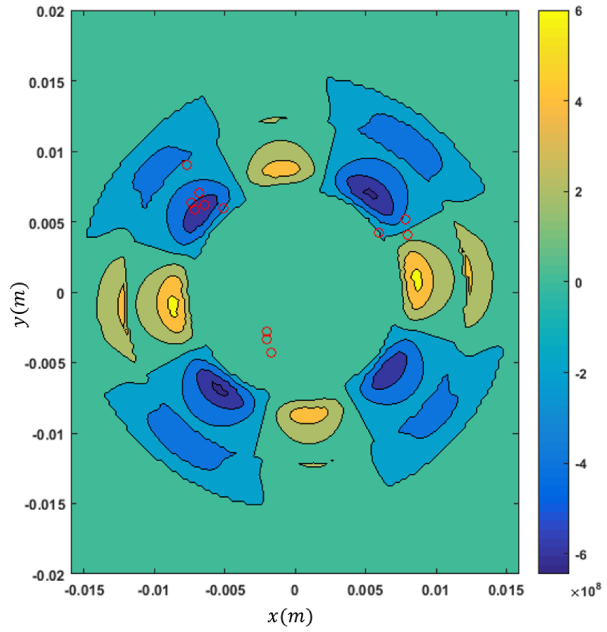

Figure 5.14: Analytic result of the normal bond force changes due to the main event assuming a sub-vertical crack plane at cycle = 70, together with the newly-formed tensile cracks in the dynamic run (red circles). Positive values represent compression; negative ones denote tension.

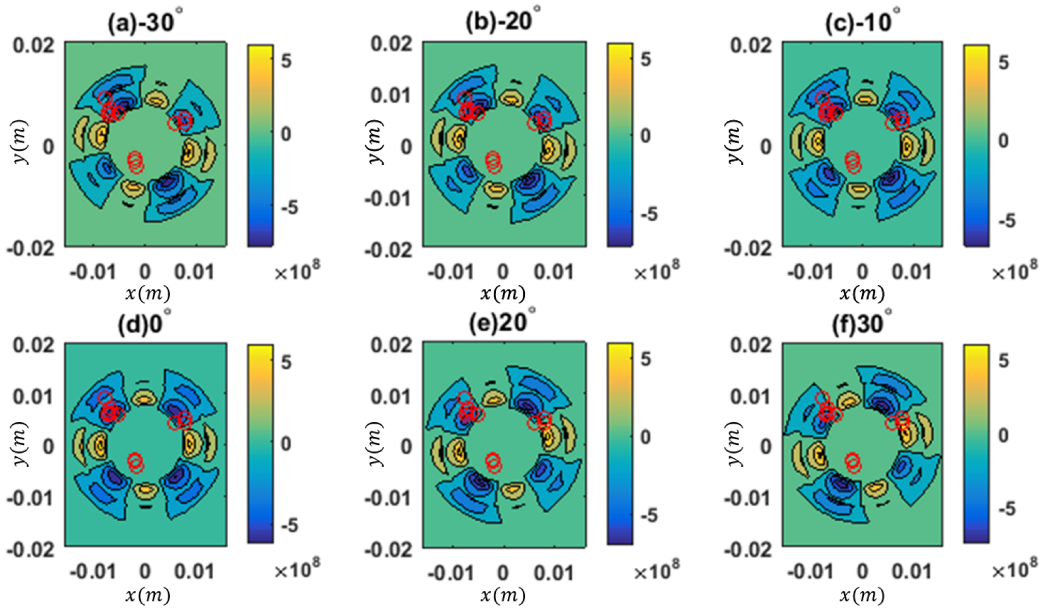

Figure 5.15: Analytical normal bond force changes on a series of sub-vertical contact planes. The angles of the contact normal are (a)-30°, (b)-20°, (c)-10°, (d)0°, (e)20°, (f)30°. Same representation is used as for Figure 5.14.

5.4 Discussion

The preceding approach calculates the theoretical dynamic stress field due to the main event and converts it into tension and compression of bond forces. The correlation of the tensile regions prone to failure and new cracks indicates the causal relationship between the dynamic stress and the newly formed cracks. However, strictly speaking, not only the dynamic stress due to the main event, but also the static stress induced by the main event, as well as both the static and dynamic stresses generated by the new cracks modify the absolute stress changes and hence influence the crack formation. Approach 1 shows more cracks are formed in the dynamic than the static run, namely, 15 and 2 respectively. The static stress due to the main event plays a less important role than the dynamic stress in crack formation, especially for the additional cracks. Meanwhile, the new cracks are smaller in magnitude and size compared

with the main event and hence the static and dynamic stresses they create are limited in magnitude. So it is reasonable to argue that the dynamic stress generated by the main event is responsible for new crack formations.

In seismology, static and dynamic stress changes are pervasively calculated to explore the interaction between a major earthquake and the following ones (King et al., 1994; Freed, 2005; Cotton and Coutant, 1997; Belardinelli et al., 1999; Kilb et al., 2000). It is found that the stresses induced by the main shock influence its neighbouring ones through a Coulomb-type friction law. The aftershocks are found to mainly concentrate in regions with elevated Coulomb stress changes due to either the dynamic or static stresses (Figure 5.2). The preceding analysis shows similar results in a granular model. The dynamic stresses due to the main event influence bond forces in a certain pattern decided by the source mechanism of the causative event. The following bond failures lie in regions where bond forces are increased by dynamic stresses (Figure 5.14). Moreover, numerical modeling offers the access to conduct the static and dynamic simulations (Figure 5.9) and hence examine the influence of static and dynamic stresses separately. The additional cracks formed in the dynamic run proves the role of the additional loading associated with dynamic stresses, which is more important than static stresses.

5.5 Conclusions

An event is stimulated to explore its radiation pattern and influence on the subsequent bond failures. Two simulations with different damping parameters are conducted. The static run with a high damping parameter is believed to be solely influenced by the static stress due to the main event. The dynamic run corresponding to low damping includes both the static and dynamic stresses.

The dynamic run has more cracks compared with the static run. The dynamic waves cause the same bond failures as in the static run, as well as additional ones. These cracks are found to concentrate in the form of clusters. The failure mechanisms of these new failures vary from event to event. These failure mechanisms likely depend on the initial stress field before the main event, which is determined by the long-term loading.

To explain the occurrence of the additional cracks in the dynamic run, the analytic solution of the dynamic stress field is derived. The analytic result shows comparable patterns with the numerical one in PFC and it aids in analyzing the stress state and failure occurrence as an independent reference.

The analytic stress is further converted to bond forces which have a more direct link to bond failures. The tensile force changes due to waves emanating from the main event show both areas of tensile force increase and decrease. Subsequent cracks are formed predominantly in areas of tensile force increase. This correlation between new failure locations and areas of tensile force increase implies the dynamic stresses are responsible for their occurrences. Static stress changes are thought to play a lesser role since only 2 out of the 15 events occur during the static run.

Numerical modeling, like PFC, has the advantage of the direct and continuous scrutiny of stress and failure. It offers the opportunity to compute stress changes and check failure locations to explore the causal relationship between the main event and the subsequent events. Dynamic stresses are shown to play an important role in altering the absolute stress state, to the point of introducing additional local cracks.

Chapter 6

Analysis of triggered acoustic emissions in a compression test [1]

6.1 Introduction

The previous chapter illustrates that dynamic stresses due to wave propagation influence failure patterns. In this chapter, the influence of dynamic waves is further explored. Instead of forcing an internal event, an external vibration is applied to study the triggering influence of previous acoustic emissions on subsequent ones.

Apart from introducing a linear component to the in-situ stress, the interaction between dynamic waves and a medium also causes a nonlinear interaction. Jia et al. (2011) conduct a uniaxial compression test on polydisperse glass beads and find that elastic parameters like wave velocities of the granular pack decrease after wave propagation. Johnson et al. (2008) and Ferdowsi et al. (2014) observe frictional weakening in sheared granular media due to wave propagation through laboratory experiments and numerical simulations respec-

[1] Part of this chapter is published as Lu and van der Baan (2016)

tively. The nonlinear behaviour of noncohesive materials such as loose sands and beads in response to dynamic waves is well-documented through physical and numerical experiments (Michlmayr et al., 2012; van den Wildenberg et al., 2013; Giacco et al., 2015). The effect of dynamic stresses on cohesive materials such as sandstones and granites is less well studied.

The objective of this chapter is to study the role of acoustic emissions in the failure process of a mechanically stressed cohesive medium. A wave with a specified amplitude and frequency is introduced by adding an external vibration to the same granite model as the one in Chapter 5. The influence of their amplitudes and dominant frequencies on failure patterns are characterized.

6.2 Model description and procedure

The model used here is the same in terms of microproperties as those in the previous chapter. A 31.7 x 63.4 mm block of Lac du Bonnet granite is represented by an assembly of 1866 particles being confined by four walls (Figure 6.1a). The average particle diameter is 1 mm. A compression test is simulated at a confining pressure σ_c equal to 10 MPa with an increasing axial stress. The axial load is added by moving the top and bottom platens at a constant velocity (strain rate), v_0 of 31.7 mm/s which corresponds to a strain rate of 1 s^{-1}. In contrast to the previous chapter, the damping parameter is kept at a constant low level equal 0.0157 to attain a realistic attenuation of the granite (Q=100).

The simulations are separated by two modes. One with an additional external loading is called a perturbed run and the other without any perturbations is called the reference run. An external vibration is introduced in the perturbed runs by assigning a sinusoidal-varying velocity to the bottom platen (Figure

6.1a) while the top platen keeps loading at the same velocity as before. The temporal change of the bottom platen movement is as follows:

$$v_y(t) = v_0 + Asin(2\pi f(t - t_0)), \tag{6.1}$$

where v_0 is the original loading velocity and t_0 is used to control gradual rising. This sinusoid has an angular frequency $w = 2\pi f$, and an amplitude A. Figure 6.1b and c shows an example of the movement of the bottom platen in a perturbed run (A=0.6) compared with the reference run. The sinusoidal-varying platen velocity causes oscillations in terms of platen displacement and hence stress changes.

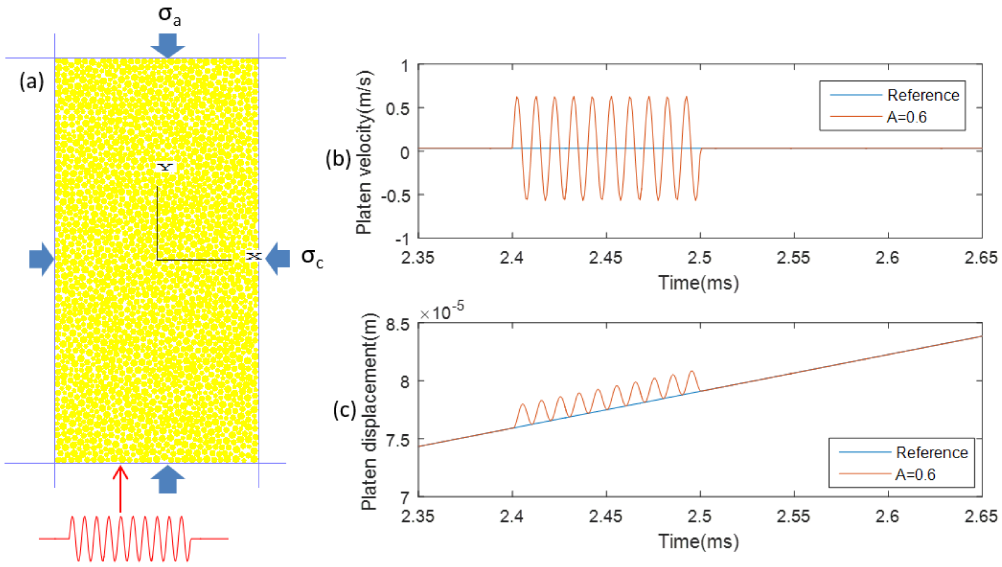

Figure 6.1: (a) Setup of the model and the implementation of the perturbed run: a sinusoidal-varying velocity is assigned at the bottom platen while the top and lateral platens keep the same configuration as the reference run. (b) Temporal changes of bottom platen velocity for the reference run and a perturbed run (A = 0.6 m/s): a sinusoid is added to the constant velocity. (c) Temporal changes of bottom platen displacement for the reference run and a perturbed run: the introduced perturbation causes a positive change compared with the reference run.

First, the influence of vibrational amplitudes is explored. The amplitudes range from 0.01 to 1 m/s, which correspond to strains on the order of 10^{-7} to 10^{-5} considering the sample dimensions. These are reasonable values in terms of dynamic strain (Ferdowsi et al., 2014). The frequency is set to be 100 kHz which corresponds to a P-wavelength equal to 55.3 particles and S-wavelength equal to 33.1 particles (Table 4.3). This value is chosen based on the size of particles in the model to decrease both dispersion and scatter in the discrete model (Toomey and Bean, 2000). Also, the model displays a severer oscillation at 100 kHz than others (Figure 4.15).

Chapter 4 show that the frequency of events during numerical compression tests ranges from 50 to 250 kHz. As a result, for tests aimed at the influence of frequencies, f is set to {50, 80, 100, 150, 200} kHz. For each simulation with a specific frequency value, a series of amplitudes are tested. The amplitude values correspond to the same strain range as the perturbed run at 100 kHz: {2.5e-7, 2.5e-6, 7.5e-6, 1.0e-5, 1.25e-5, 1.5e-5, 2.25e-5, 2.5e-5}.

The perturbation is set to last 1 ms and it is arranged shortly before one major failure event chosen from the reference run. The timing is decided based on two reasons. (1) The model has to be loaded close to failure, otherwise less failure can be observed. (2) The chosen failure is made up of several bond breakages which makes for an obvious stress drop in the axial stress curve. The influence of the dynamic waves can then be easily detected solely based on the axial stress.

During each simulation, the axial stress is monitored as an indicator of failure occurrences and the overall stress state throughout the model. It is calculated by averaging the forces of the top and bottom platens (Equation 3.8). As the axial stress is a rough estimate of the internal stress state, the

change in axial stress cannot display every event clearly. Only the larger events associated with more energy can be captured by the stress curve in the form of a stress drop. So bond breakages in the form of acoustic emissions (AE) and clusters (AEc) (Hazzard and Young, 2002) are also recorded. Each bond breakage is called an AE due to energy release into its kinetic form. Bonds that break close in time and space are thought to form an event, also called AEc, an acoustic emission cluster. Particle motion in the vicinity of one event is recorded to calculate the kinetic energy for an event (Chorney et al., 2012; Chorney, 2014).

6.3 Results

6.3.1 Reference run

The reference run sets a benchmark for the perturbed simulations. Figure 6.2 shows the changes in terms of axial stress, event magnitude and failure energy. The axial stress increases linearly at first until 1.2 ms when bonds start to break (black circles). Then the stress slope gradually decreases and bonds start to fail now and then, releasing stress concentration and converting strain energy to kinetic energy. The stress drop occurring at 2.56 ms (highlighted by the red star) corresponds to a major failure. After a temporary stress drop, stress continues to increase due to the constant loading. The final failure occurs abruptly after the peak stress with a large amount of bond breakages and energy release.

Figure 6.3 shows the spatial distribution of bond failures before and after the peak stress. At first, the distribution of bond breakages is spatially uncorrelated due to the intrinsic inhomogeneity. Stresses develop unevenly throughout the sample; local failures occur in regions with stress concentrations and lower

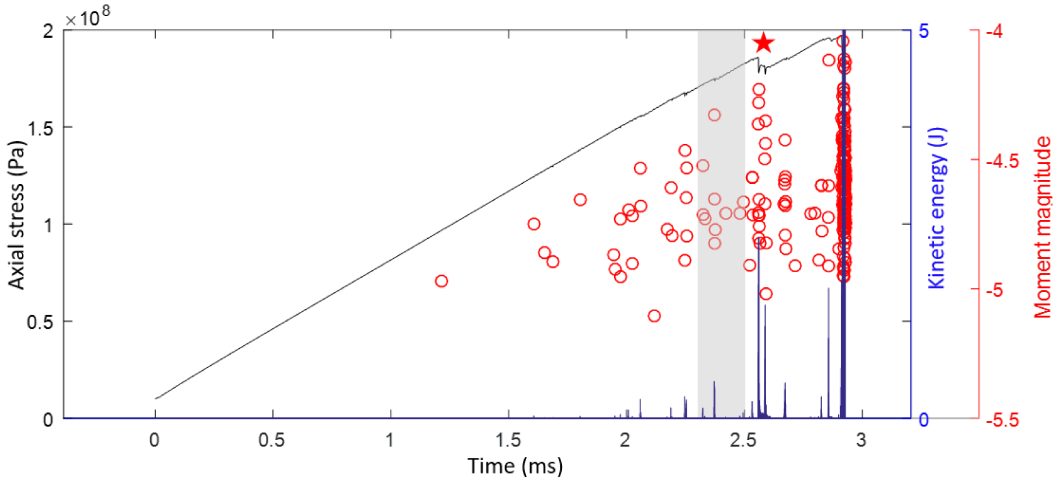

Figure 6.2: Characteristics of the reference run: histories of the axial stress (continuous black line), the magnitude of events (dots) and failure energy associated with events (blue histogram). The red star highlights the first major stress drop at 2.56 ms. The shaded area corresponds to the vibration interval in the following perturbed runs.

bond strengths. The spatially diffused bond breakages begin to coalesce into the macroscopic failure plane (blue ellipse in Figure 6.3b) when the peak stress is achieved. The catastrophic failure occurs with significant bond breakages and a considerable energy release shown in Figure 6.2 around 3 ms. This numerical simulation shows similar behaviour as laboratory tests, e.g. Figure 5a and Figure 7 in Lockner et al. (1992).

6.3.2 Influence of perturbation amplitudes

The external vibration is added before the known major failure in the reference run (shaded area in Figure 6.2) to investigate the influence of dynamic waves on failure. Figure 6.4a shows the result of the perturbed runs with different vibrational amplitudes compared with the reference run. The most notable changes are stress oscillations during the vibration interval (shaded area). Besides, the perturbation changes the failure process from the reference run in both the short and long term.

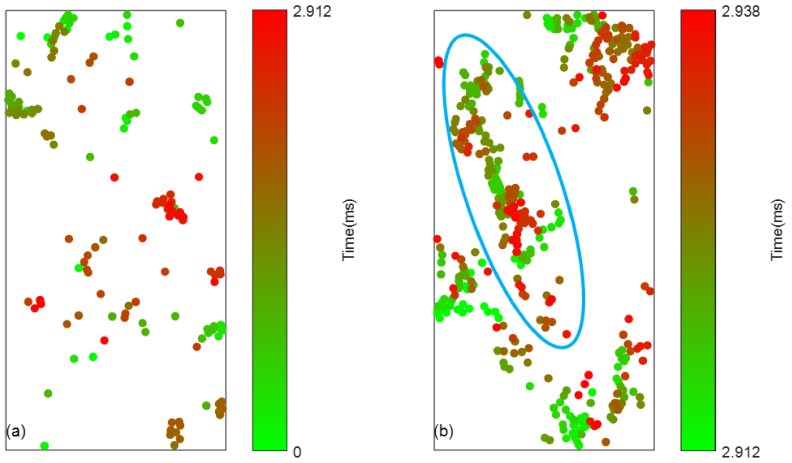

Figure 6.3: Location of bond breakages formed (a) before and (b) after peak stress. The dot color represents time of occurrence. Green is early and red is late in time (note different color scales for two plots). The blue ellipse in (b) highlights the macroscopic shear failure plane.

Short-term influence of the external perturbation

Figure 6.4b is the zoomed-in image illustrating the immediate changes due to the vibration. During the perturbation, the axial stress oscillates in step with the top platen velocity (Figure 6.1b). The amplitude of stress oscillations scales with the vibrational amplitude. After termination of the perturbation, the stress curves continue to increase due to the constant loading. The perturbation is arranged at the time before a major failure to explore the influence of the dynamic waves on its occurrence. Figure 6.4b shows that the introduced vibration changes the time of the expected major failure at 2.56 ms in the reference run. This failure is associated with an obvious stress drop. Further, Figure 6.5 plots the time difference of the first major stress drop in the perturbed runs from that of the reference. A negative value implies an earlier occurrence. Generally speaking, the introduced perturbation above a threshold amplitude of 0.4 causes a stress drop which happens earlier compared with the

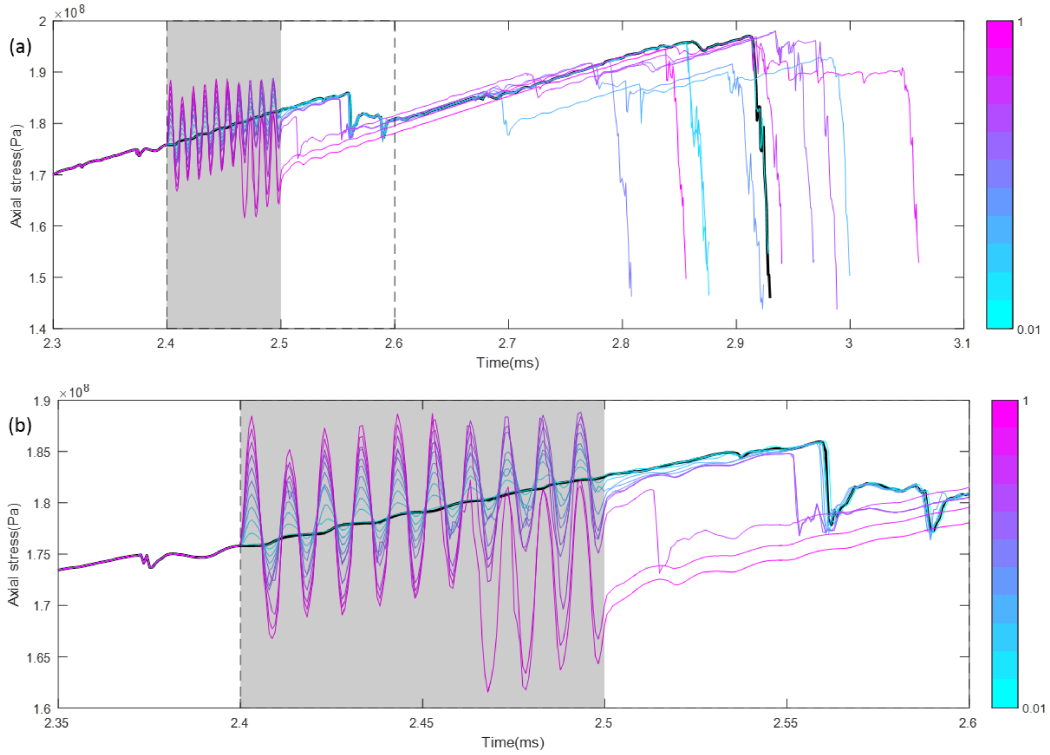

Figure 6.4: (a) Comparison of the reference (black curve) and perturbed runs in terms of axial stress. The vibration interval is shaded by gray color and the rectangle between times of 2.4 and 2.6 ms highlights the short-term influence of the vibration (curve colors coded by vibrational amplitudes A). (b) Detailed image of the short-term influence of the vibration.

reference run. Large vibrational amplitudes cause an advance of the first stress drop; yet vibrational amplitudes A $\leq$ 0.4 do not change the timing of the first stress drop, whereas amplitudes A $>$ 0.4 advance it, especially when A $>$ 0.7, a significant time advance is observed.

Apart from the temporal changes of the first major failure, the spatial influence is also examined. The location of bond breakages is checked for three perturbed runs for amplitude A equal to 0.1, 0.6 and 1 (Figure 6.6). These three runs correspond to the three kinds of the temporal influences: obvious advance, slight advance and no change in occurrence of the expected local failure.

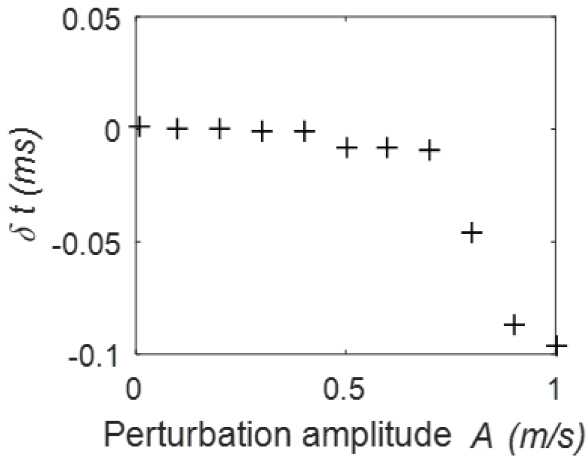

Figure 6.5: Time difference of occurrence of the studied local failures in the perturbed runs from the reference run. A negative value represents clock advance.

Four sets of symbols are used to represent the failed bond locations in four different simulations. Figure 6.6a shows bond breakages associated with the studied local failures. These four symbols overlap; difference lies in that additional blue crosses are observed in the left middle part of the model. It implies more bonds have failed in the simulation with the largest vibration (A=1). This indicates that strong vibrations bring about more bond breakages.

The energy associated with the expected local failure is further explored. Figure 6.7 displays energy release for the reference and three perturbed runs A=$\{0.1,\ 0.6,\ 1\}$. The cumulative energy curve for the smaller perturbation A=0.1 (green) traces that of the reference run (black). For the largest perturbation A=1, the blue curve exceeds the other three due to the advanced local failure as well as additional cracks shown in Figure 6.6a shortly after the introduction of the vibration. The red curve corresponding to the cumulative energy for the medium perturbation A=0.6 climbs above those of the reference and smallest perturbed curves (A=0 and A=0.1, respectively). The difference is largest when its major and clock-advanced event occurs (red star). The dif-

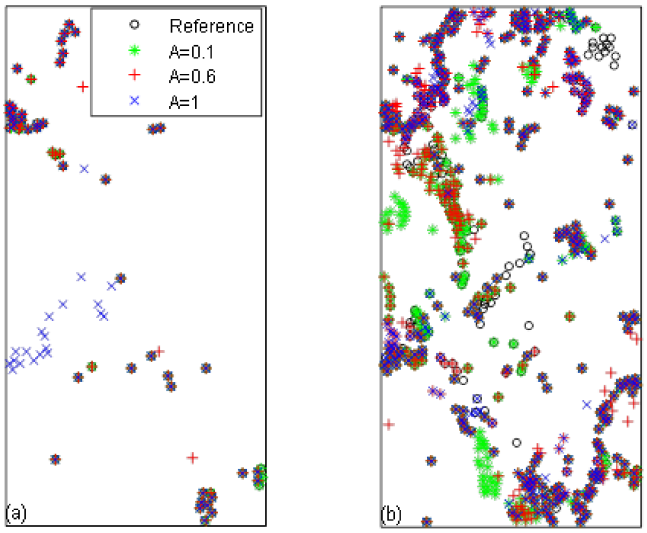

Figure 6.6: Location of bond breakages for reference and three perturbed runs at different time intervals: (a) bond breakages associated with the first major stress drop; (b) all bond failures throughout the loading stage.

ference becomes minimal when the major events occur in the A=0 and A=0.1 runs (black and green stars). This indicates that for all three runs A={0, 0.1, 0.6}, essentially the same number of cracks are formed and the same amount of kinetic energy is released in the short term but that the events can occur at different times. The A=1 run releases more energy and the local failure occurs earlier than all other tests at least in the short term.

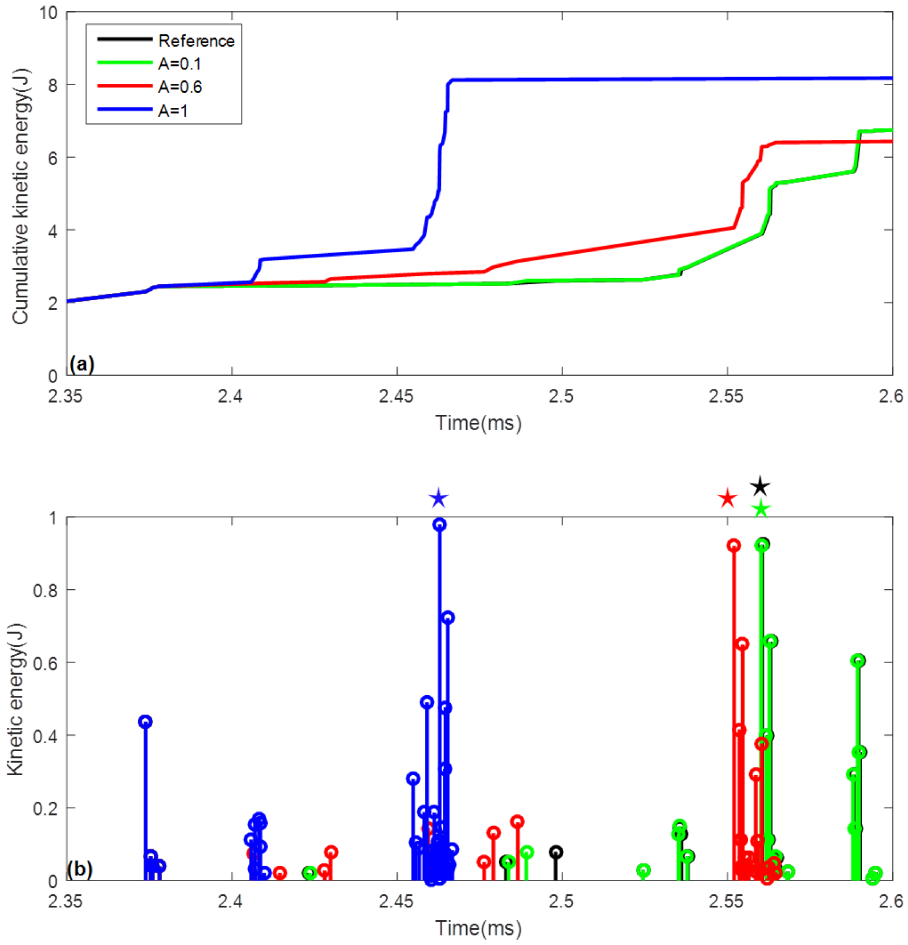

Figure 6.7: (a) Cumulative kinetic energy and (b) kinetic energy for reference and three perturbed runs related to the short-term influence. The stars in (b) highlight the occurrence of the measured major local failure.

Long-term influence of perturbation

The introduced vibration can not only cause an immediate clock-advance of the expected local failure, it also has long-term influences: changing the occurrence of (1) local failures and (2) the final macroscopic failure.

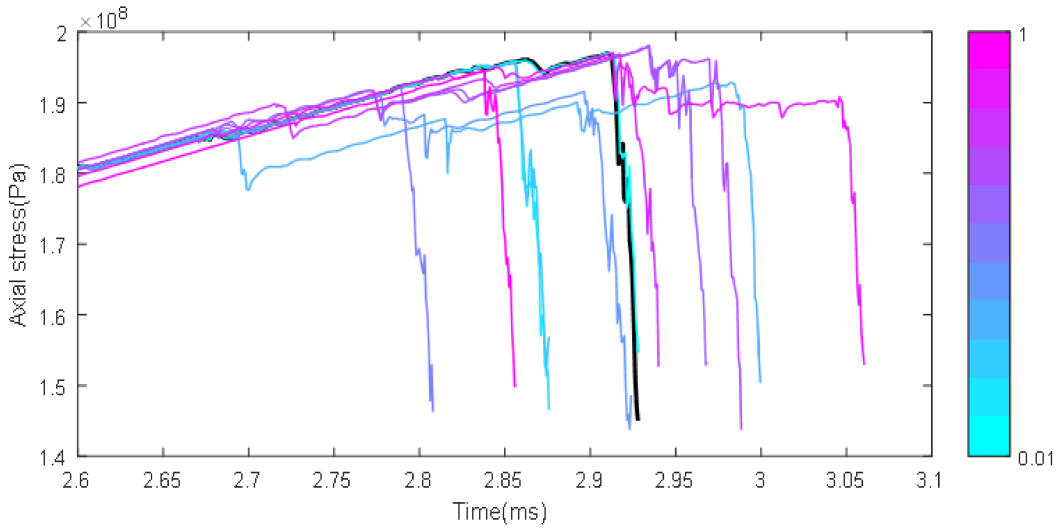

Figure 6.8: Detailed image of the long-term influence of the vibrational amplitudes. Color conventions follow those in Figure 6.4.

The final failure can be either advanced or delayed (Figure 6.8). The relative timing of the final failure is plotted in Figure 6.9 for all perturbed runs. A negative value represents clock advance. Contrary to Figure 6.5, no simple relationship between timing and perturbation amplitudes exists with both clock advances and delays occurring. Figure 6.10 presents the occurrence of events for the reference and perturbed runs. Events with energy release larger than 0.5 J are selected to exclude small ones that occur randomly. It shows that the external vibration disrupts the failure sequence. When the perturbation is substantially large, the final failure is advanced as the immediate local one. For a run with moderate perturbations, the final failure is preceded by one or more local failures and delayed compared with the reference run.

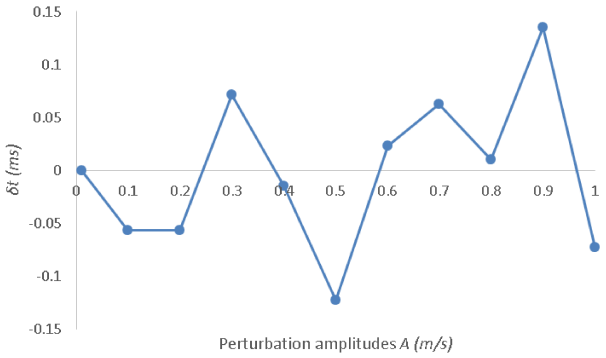

Figure 6.9: Time difference of occurrence of the final macroscopic failures in the perturbed runs from the reference run. Calculations follow Figure 6.5.

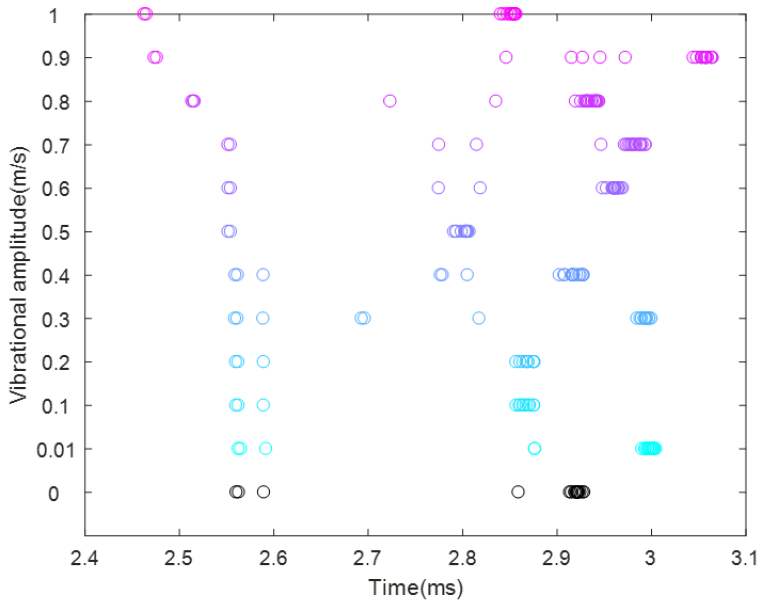

Figure 6.10: Event timing in the reference (black) and perturbed (colors scaled according to vibration amplitudes) runs.

In addition, vibrations change the amount and locations of bond breakages. Figure 6.6b shows the spatial distribution of all the bond breakages in four runs. The four sets of symbols overlap each other, part of which comprise a macroscopic shear failure plane as highlighted in Figure 6.3b. Still, some differences exist in the four simulations: (1) the additional short-term failures when A equals 1, the additional blue crosses in Figure 6.6a, also occur for the other

three runs (Figure 6.6b) but at a later time. This indicates that dynamic triggering induces more of an advance of the expected failure than simply creating additional ones; (2) the smaller vibration A=0.1 introduces some cracks not present in the other perturbations (green stars). Hence, the additional vibrations are not simply clock-advancing or delaying failure patterns. It may be that the slightly longer simulation time (Figure 6.4a) plays a role although the final axial stresses are similar.

6.3.3 Influence of perturbation frequencies

In the previous section, vibrations with a range of amplitudes are added during the loading stage to study the influence of dynamic waves. The behaviour in response to perturbations varies with the perturbation amplitude. A minimum value corresponding to a strain of 10^{-5} is required to advance the expected local failure. In this part, the influence of vibration frequencies is studied. The frequencies used are f={50, 80, 100, 150, 200}kHz. All the other perturbation parameters, including perturbation strain amplitudes which range from 2.5×10^{-7} to 2.5×10^{-5}, timing and duration, and confining stress are the same as used in the previous part.

Figure 6.11 shows the short-term influence in response to a series of amplitudes for different frequencies. All plots show similar features: (1) perturbations result in simultaneous stress oscillations proportional to vibrational strain amplitudes (see legends); (2) the expected local failure is advanced when the vibration strain strength exceeds a certain value of about 10^{-5}. However, stress oscillations for runs with the same strain amplitudes but different frequencies are proportional to vibrational frequencies. Besides, runs with high frequencies induce an earlier occurrence of the studied failure if the failure is advanced.

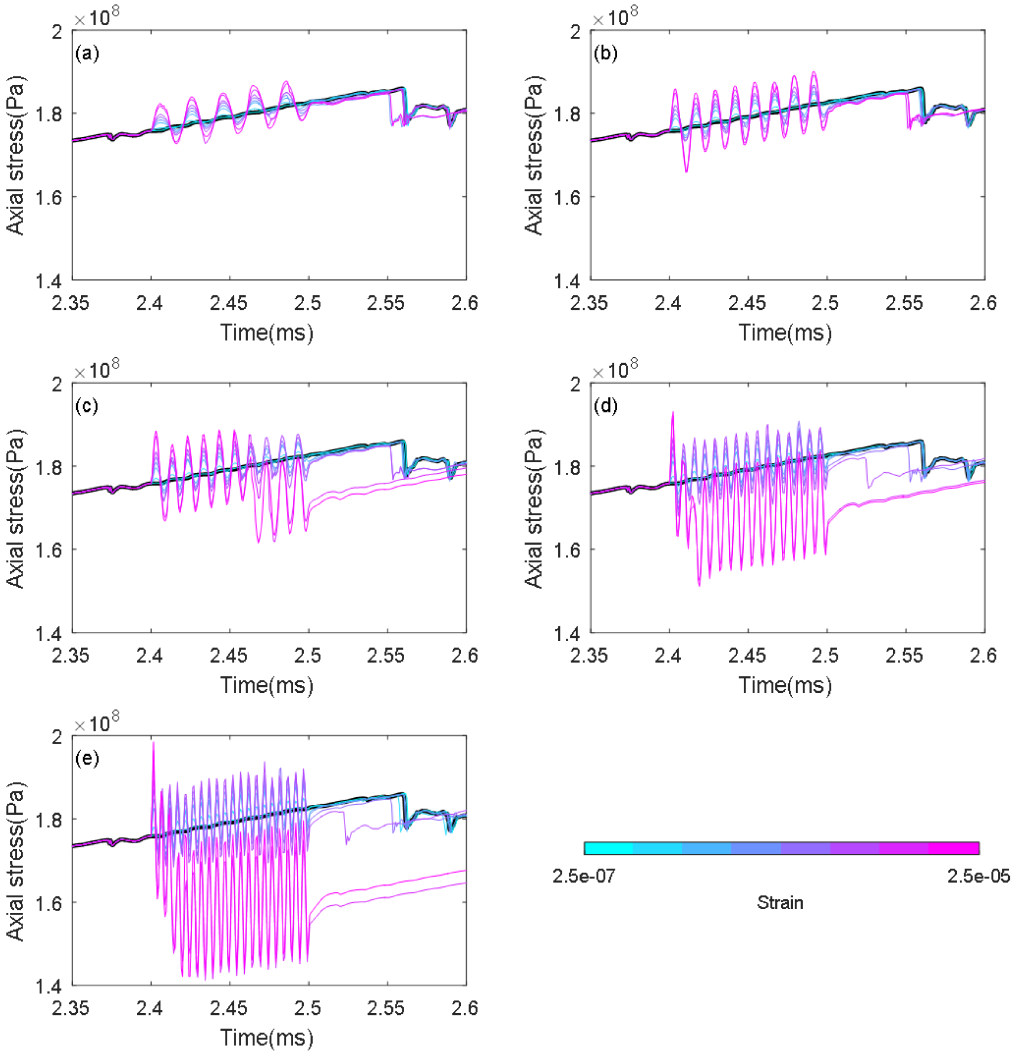

Figure 6.11: Short-term response to external vibrations with a range of strain amplitudes, using different frequency perturbations: (a)-(e) correspond to 50, 80, 100, 120, 200 kHz respectively. Curve colors are coded by vibrational strain values.

The influence of vibrational strain amplitudes on clock advance of local failures for different frequency perturbations is summarized in Figure 6.12. All curves display a transition to an obvious clock advance within a vibration strain range of 1.3×10^{-5} - 7×10^{-4}. For the tested frequency range, when the vibration strain is below this value, the perturbation tests show no or little changes from the reference run in the occurrence of local failures. It also shows per-

turbations with higher frequencies (magenta curves) have a more pronounced influence in terms of triggering efficiency: a smaller vibration strain is needed to achieve the same amount of clock advance time.

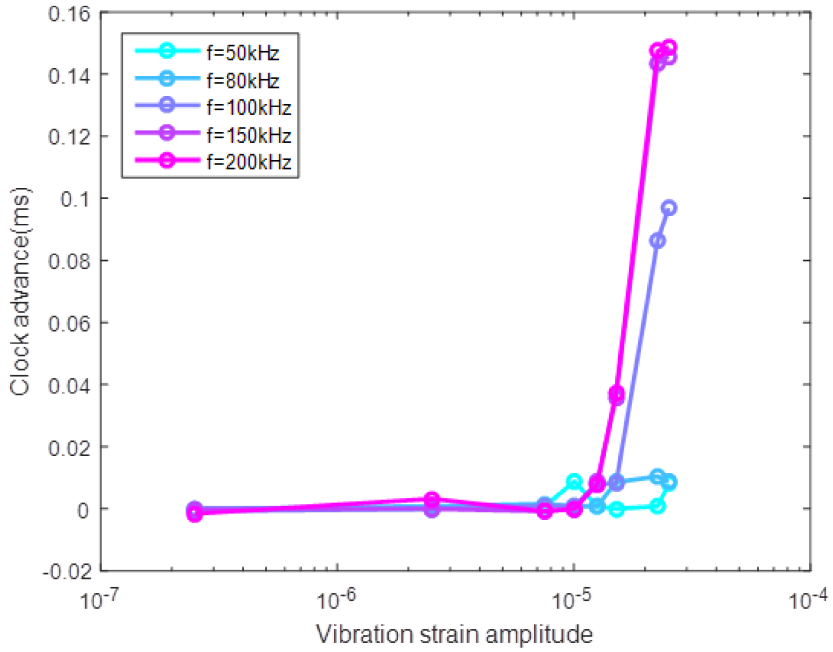

Figure 6.12: Influence of perturbation amplitudes on immediate triggering in terms of clock advance for different frequency perturbations.

Figure 6.13 displays the long-term influence on the failure process. Similar to the short-term influence, the failure process is altered due to the temporary vibration. For all tests with different frequency values, the final failure can be either delayed or advanced depending on the magnitude of vibration. An earlier failure occurs when A equals 0.1, 0.2, 0.5, 1. In cases with a delayed failure when A equals 0.01, 0.3, 0.6, 0.7, 0.9, a cyclic behaviour is observed.

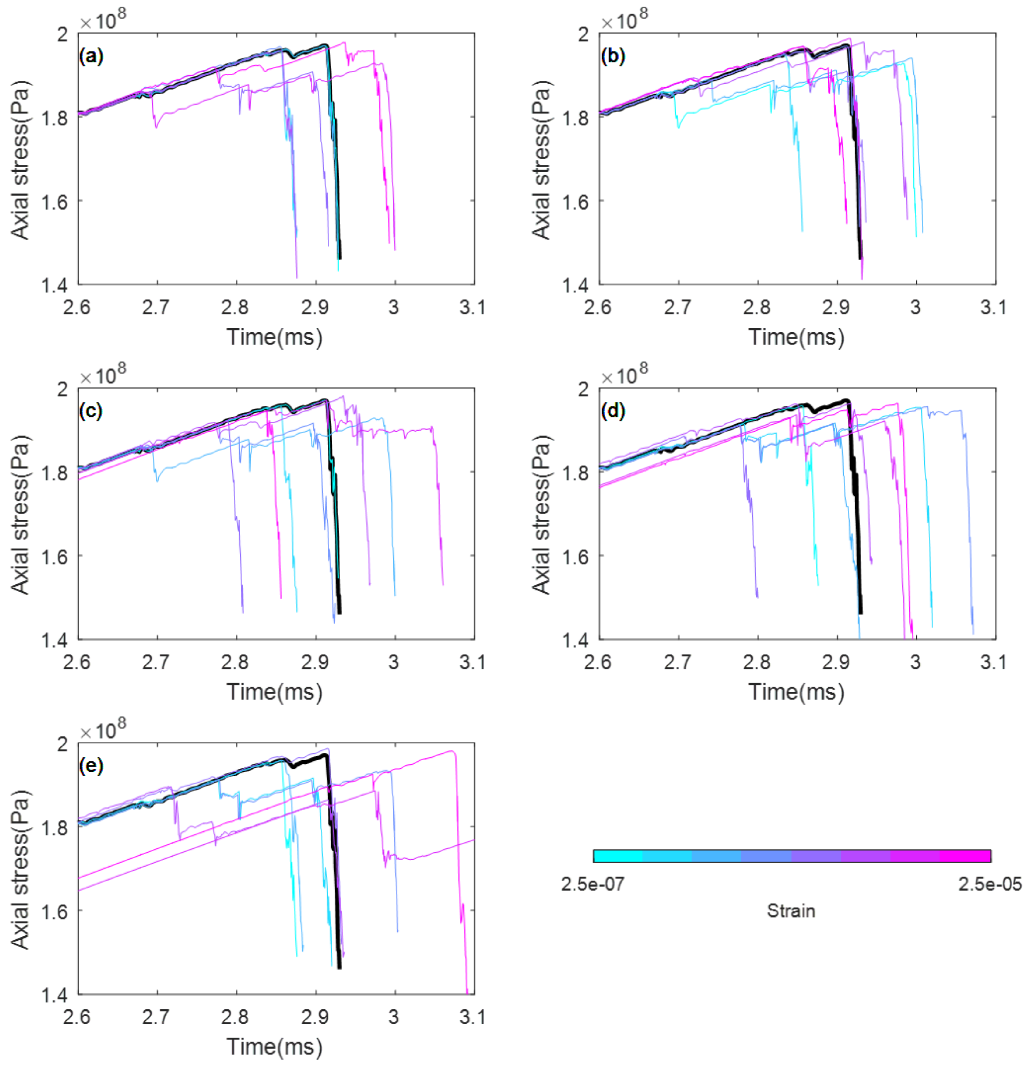

Figure 6.13: Long-term response to external vibrations with a range of amplitudes using different frequency perturbations: (a)-(e) correspond to 50, 80, 100, 120, 200 kHz respectively. Curve colors follow those in Figure 6.11

6.4 Discussion

6.4.1 Dynamic triggering

An external vibration introduced before a major failure event has an immediate influence of advancing this failure when the induced strain amplitudes are larger than 1.25×10^{-5}. All curves with different frequencies show the threshold

of the strain amplitude being about 10^{-5} to induce a clock advance of an expected local failure. This value is larger than the finding of a threshold of 10^{-6} in a sheared granular medium (Ferdowsi et al., 2015). It is probably mainly due to the cohesion between particles in BPM which adds to the strength of the model. Besides, model setup including the confining stress and the driving mechanism are different.

External strain vibrations result in oscillations of axial stresses (Figure 6.4b). To explore what is going on beneath the stress oscillations, an autoregressive (AR) model (Tary et al., 2013) is applied to the recorded time series to remove sinusoids. The AR model is a linear prediction filter to describe time-varying processes using previous samples. In practice, the input parameters of an AR model include the pole number and window length. Filter coefficients are computed using the Burg method which is based on a recursive least-square scheme to minimize prediction errors.

The AR model is used to reconstruct and remove harmonics in the axial stress. Three poles and a window of 80 length are used based on visual tests. Figure 6.14 shows how the AR model is applied to the case when A equals 0.6. First, the data are prepared by removing the trend of the axial stress and the segment of 126 points containing the sinusoids is selected as the input signal of the AR model. The time-frequency representation of the segment shows a frequency of 100 kHz, which coincides with the frequency of the imposed vibration. Figure 6.14d shows the reconstruction of the sinusoidal part along with the original segment and they match quite well. The error, which is the residual after detracting the reconstructed signal from the original one, is almost negligible. The reconstruction and error signals are then concatenated with the other parts in the data. Figure 6.14e shows a perfect match between the original and reconstructed signal, validating the AR model and its parameters.

Figure 6.14f shows a nearly constant decrease in stress after the removal of the perturbation influence. This procedure is applied to all other runs with different vibrational amplitudes (Figure 6.15). A stress decrease is observed after removing sinusoids due to vibrations when compared with the reference curve. The value of decrease is proportional to the perturbation strength. This implies material weakening. The perturbation in the form of constant loading and unloading somehow weakened the sample so that it cannot support the load it could bear previously in the reference run (FFigure 6.1c). And when the vibrational amplitude exceeds the threshold value, the weakened model responses with clock-advanced failures.

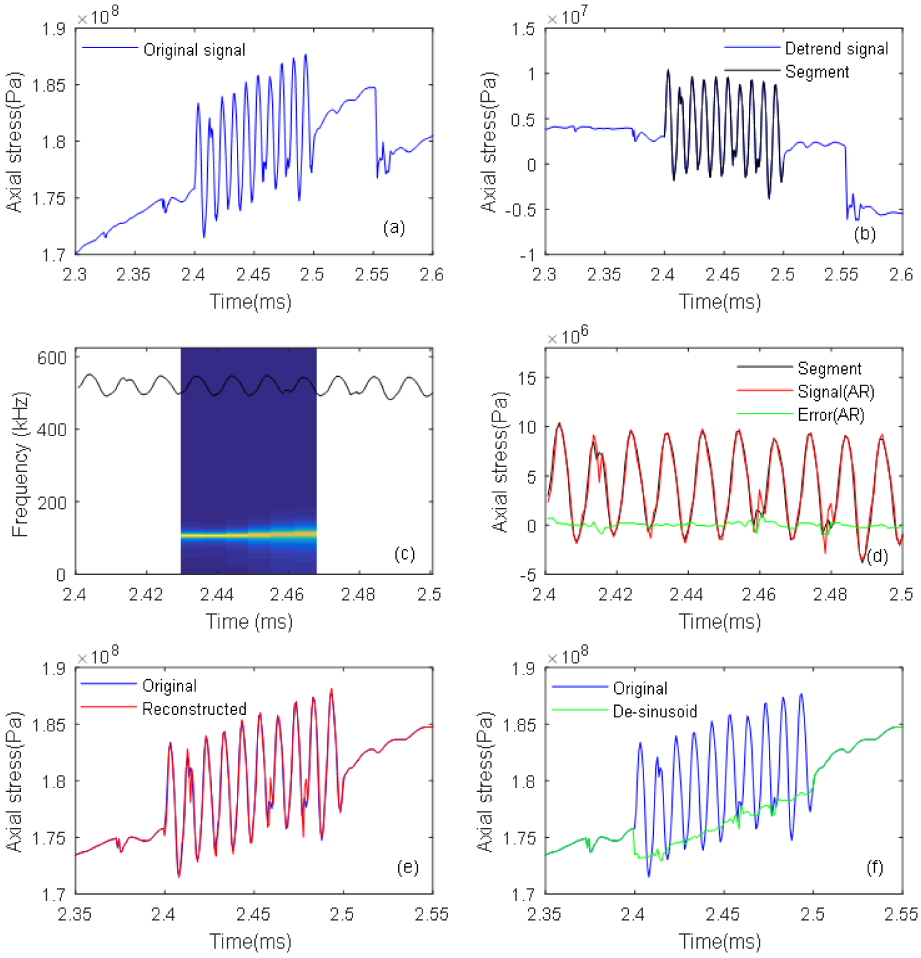

Figure 6.14: Procedure of sinusoids removal: (a) time series of axial stress, (b) detrended signal (blue) and the segment data used for analysis (black), (c) segment data (black) and its time-frequency representation, (d) comparison of the data segment (black), reconstructed data using AR model (red) and the residual (green), (e) comparison of the original (blue) and constructed (red) data, (f) comparison of the original (blue) and de-sinusoid (green) data.

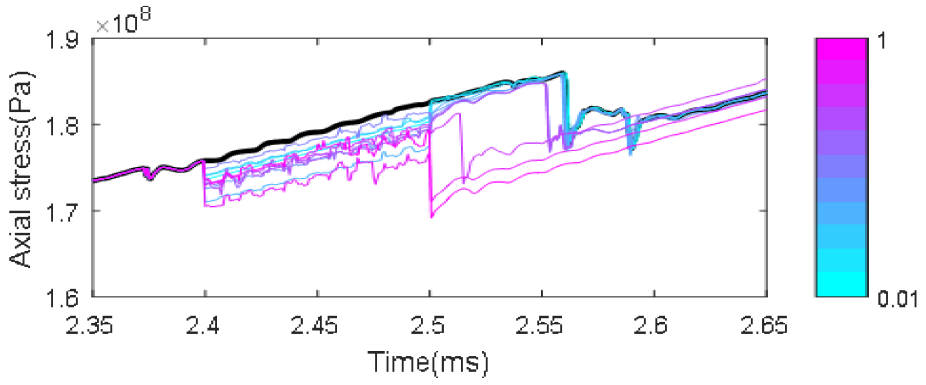

Figure 6.15: Axial stress curves after the removal of sinusoids due to the vibrations. Color conventions follow those in Figure 6.4.

Micromechanical analysis

To understand how weakening occurs because of vibrations, the model is further studied at the micro-scale. In a discrete model where particles interact at contacts, the model behaviour is decided by contact dynamics. The external loading is not evenly shared by all contacts (Oda et al., 1982). The contacts can be subdivided into two categories according to the amount of force carried by each contact. Weak contacts are the contacts carrying forces smaller than the average contact force of the model. Strong contacts are those carrying forces larger or equal to the average contact force. These two subnetworks work together in a complementary way. The strong contact network forms the main force chain bearing most of the external load. It tends to align with the direction of the major principal stress. The weak contacts facilitate deformation by sliding (Radjai et al., 1998). Contact forces are computed in PFC at each calculation step and two time slides are presented in Figure 6.16 using the plotting functions in the embedded package *Fishtank* in PFC: contact forces before and during loading. The black columns represent contact forces between particles. The width is proportional to the force value. The contact force is more isotropic before loading. When subject to the external load, contacts tend

to align with the maximum principal stress direction, here the axial direction, to form a network sustaining the deviatoric stress. The angle histogram in Figure 6.17 further confirms this. The strong contacts have a preferential direction parallel with the maximum principal stress direction whereas the weak contacts are more isotropic in all directions.

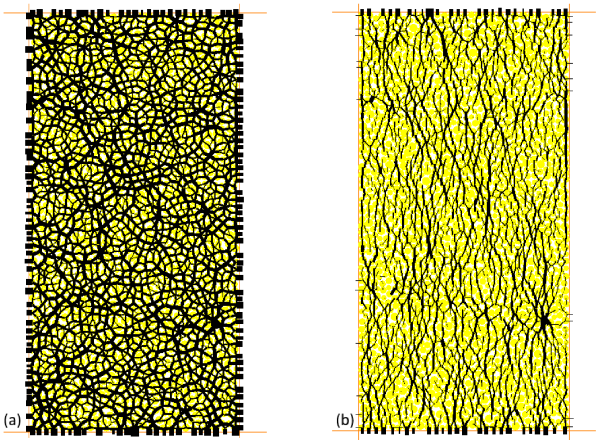

Figure 6.16: Contact forces (a) before and (b) during loading. The black column represents contact force with its width proportional to the force value (scaled to their maximum value).

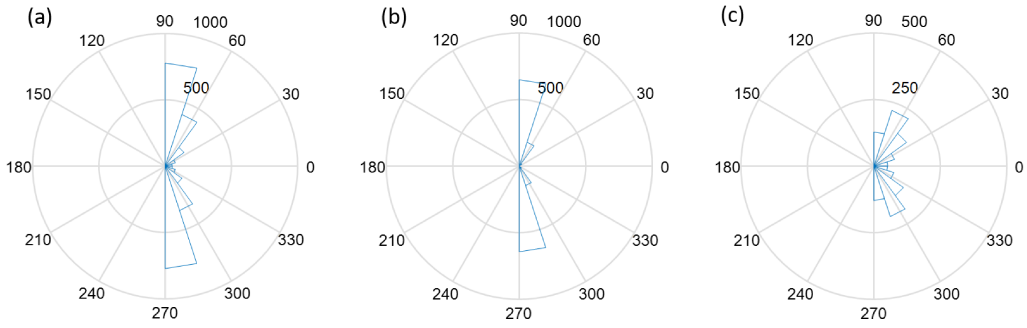

Figure 6.17: Angle histogram of the contact force orientations during loading corresponding to Figure 6.16b: (a) all contact forces and (b) strong contact forces and (c) weak contact forces. Vertical contact forces are displayed as 90°.

The contact force and contact network is investigated for the reference and three perturbed runs when A={0.1, 0.6, 1} for frequency f equals 100 kHz

(Figure 6.18). The average contact force changes for the perturbed runs show periodic variations similar to the axial stress in Figure 6.4. Significant decreases in contact force ensue from local failures. The quantities of strong and weak contacts also experience oscillations during each perturbation. The difference lies in that the strong contacts have losses while the weak contacts have gains. This fact confirms the weakening phenomenon. The vibration weakens the strong contact network, which supports the main body of the load. For smaller perturbations (A=0.1), the decrease of strong contacts and increase of weak ones terminates along with the vibration and the contact network composition recovers to that of the reference run. In response to medium and large perturbations, e.g., A=0.6 and 1, the variations in the contact network are more pronounced and irreversible at least in the short term by changing the timing of the measured local failure event.

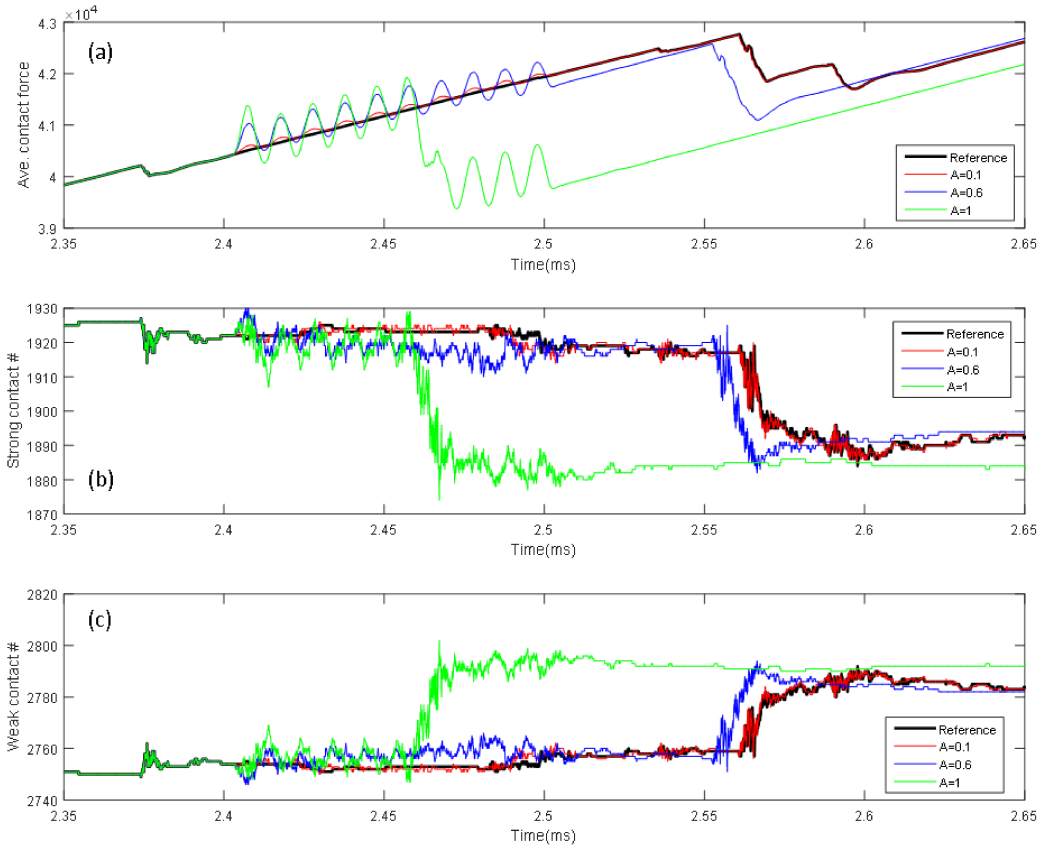

Figure 6.18: Micromechanical analysis of the contact networks: (a) history of average contact force; (b) number of strong contacts carrying forces larger than the average; (c) number of weak contacts carrying forces below the average.

6.4.2 Occurrence of the final failure

The immediate influence of an external vibration is to induce advanced local failures. An amplitude threshold exists for this time advance (Figure 6.5). For the long-term influence in terms of the occurrence of the final macroscopic failure, a simple linear relationship is not sufficient to describe the dependence on strain amplitudes. Analysis of the kinetic energy shows a chain reaction exists, similar to the clock advance-suppression-recovery cycle observed in sheared granular media in response to dynamic waves (Ferdowsi et al., 2014). The measurement of kinetic energy is applied on particles activated by a specific

event (Chorney et al., 2012; Chorney, 2014). It is measured per event. The cumulative kinetic energy is also recorded to deliver an overall measurement. Figure 6.19 shows the kinetic energy results for the reference run and perturbed run with A equal to 0.6 at 100 kHz. Bonds break due to the propagation of the dynamic waves induced by the bottom platen movement. The bond breakages are associated with conversion of strain energy into kinetic energy (Figure 6.19c). The cumulative kinetic energy curve for the perturbed run (red) starts to deviate from the reference curve (black) at the introduction of the vibration. This active stage is characterized by advance of the local failure. The failure is accompanied by a stress drop, resulting in a lower stress at bonds which are less likely to fail. For the perturbed run, it is less active in bond breakages. The red curve is exceeded by the black one when the major local failure occurs in the reference run. This indicates that the expected event is smaller in the perturbed run than the reference one. Following Ferdowsi et al. (2014), this stage is called energy suppression because of less energy release. However, this stage of quiescence is temporary and terminated by a series of new failures. Constant loading leads to stress concentration at bonds. Failures occur with more energy release than for the reference run in the same time interval. This compensates for the previous energy suppression stage. Bond breakages alleviates stress concentrations and leaves most of bonds at a lower stress requiring more time to fail. So the final failure for the perturbed run is delayed compared to the reference run. This indicates a chain reaction of acoustic emission occurrences and energy release: the advanced failure leads to periods of energy suppression, the recovery stage with energy compensation leads to the delayed final failure. But this does not always happen. When the vibration is extremely large, e.g., the A=1 run, the advanced local failure is followed by the advanced final macroscopic failure (Figure 6.8). This is possibly due to the large amount of energy release due to the clock-advance event (Figure 6.7).

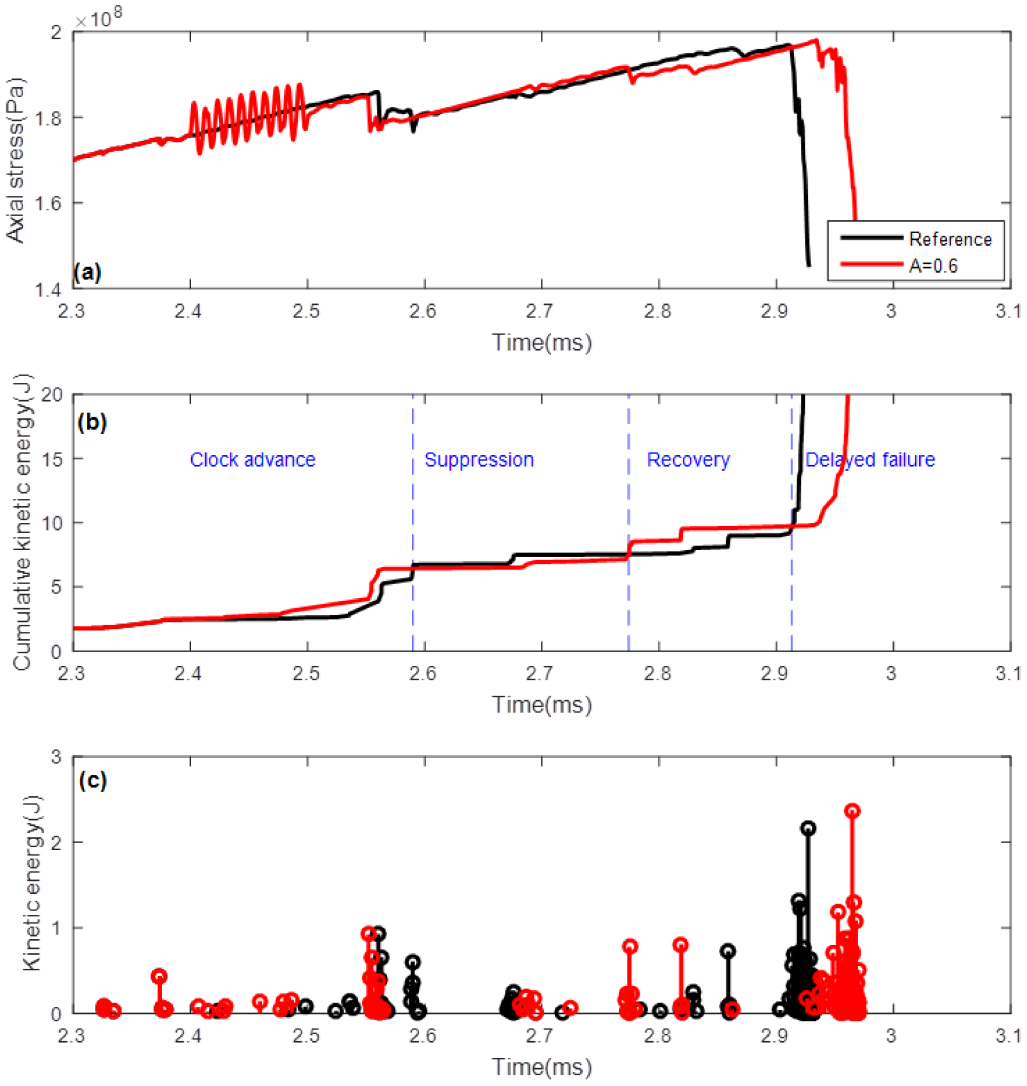

Figure 6.19: Characteristics of the dynamic behaviour of the reference run and perturbed run with A=0.6: (a) Axial stress history. It shows the time advance of the first stress drop. (b) Cumulative kinetic energy due to bond breakages. After the advanced energy release, the perturbed run experiences stages of suppression and recovery. (c) Kinetic energy of each event showing the occurrence of events.

6.5 Conclusions

An external vibration is added temporarily during a compression test to study the triggering influence of previous acoustic emissions on subsequent ones. The

introduced vibration at the bottom platen propagates through the sample, carrying a dynamic stress and affecting the background stress field. It is found that:

1. The perturbation weakens the model by softening the strong contact network. It can cause an advanced local failure during the vibration interval when the vibrational strain amplitude is large; it leads to an advanced failure after the termination of vibration when its amplitude is moderate; it does not make any difference in terms of timing of the local failure when the perturbation is small. A frequency-dependent amplitude threshold of about 10^{-5} exists in the cohesive granular model, which is larger than 10^{-6} in the non-cohesive granular system.

2. The long-term influence is less clear than the short-term response. The final failure can be either advanced or delayed. For runs with a moderate perturbation, the local failure is advanced with less energy release for the same event. So more local events occur to compensate for the energy suppression, yet the final failure is delayed.

3. The temporal and spatial analysis of acoustic emissions shows that dynamic triggering leads to an 'advance', but does not simply 'create' more events in the short term. The external vibrations may change the timing of events but rarely their locations. The long-term influence in terms of acoustic emission quantities is hard to determine as the simulation time is an important factor.

4. Higher frequency perturbations have a more effective triggering influence. For the same vibrational strain amplitude, the runs with higher frequen-

cies have a more advanced local failure.

Chapter 7

Conclusions and future work

In this thesis, the topic of dynamic triggering of acoustic emissions is studied using the Bonded Particle Method (BPM).

The capability of BPM handling elastodynamical problems is first examined in **Chapter 4**. A single force excitation is added in a granite rock model using BPM. The comparison with analytical solutions regarding wavefields and the associated stress patterns shows a comparable result. Speckle noise and waveform distortions are caused by the use of a discretized and irregular grid of individual particles, masking partial details visible in the analytical solutions. Nonetheless, numerical solutions using BPM exhibit the main features in terms of patterns and polarities, and hence allow for the examination of stresses related to wave propagation in this thesis.

The study of dynamic triggering of acoustic emissions is carried out by simulating a compression test. In **Chapter 5**, a major event is created within the model. The influence of dynamic stresses is examined in two approaches. The first one is to compare the influence of the static and dynamic stresses directly by simulating a static and a dynamic run respectively. The dynamic run is found to experience a more vibrant motion and have more bond failures

compared with the static run in response to the same event. This implies dynamic stresses play a more important role than static stresses in causing bond breakages. The second approach aims at studying the interaction between the main event and the following ones using the analytic solution for the dynamic stresses. The expressions of the dynamic wavefield and stress patterns are derived and validated. The analytic dynamic stress is converted into the change of bond forces which is the direct indicator of whether a bond will fail in BPM. The correlation of bond force changes and bond breakages confirms the causal relation between dynamic stresses incurred by the main event and the occurrence of following events.

Chapter 5 demonstrates the role of dynamic stresses in altering the stress field and hence inducing a favorable change in the stress state for bond breakages by creating an internal event. To work in a more controllable way, in **Chapter 6**, a vibration is introduced externally to initiate wave propagation. The influence of wave characteristics in terms of amplitude and frequency on an immediate local failure and the final microscopic failure is studied. The external vibration weakens the model in the form of less load bearing than it does without perturbations. The micromechanical analysis corroborates this showing that strong contacts decrease substantially by vibrations. When the vibrational amplitude exceeds the threshold value, the weakened model responses with an advanced local failure. The amplitude threshold is frequency-dependent. It is about 10^{-5} in terms of the imposed strain amplitude, larger than 10^{-6} in a non-cohesive granular model. The final failure can be either advanced or delayed. A moderate perturbation advances the immediate local failure and delays the final one which can be explained by the chain reaction of energy release: the advanced local failure is associated with less energy release for the same event, and so more local events occur to compensate for the energy suppression and the final failure is thus delayed. For the tested frequency

range, higher frequency perturbations have a more effective triggering influence.

Apart from implementing this study in the three-dimensional context for a more realistic evaluation, several interesting topics arise for further study.

In **Chapter 6**, dynamic waves are found to expedite local failure. In practice, the addition of vibrations to hydraulic fracturing treatments may have a positive effect on their efficiency (Hulse, 1959). Yet more detailed investigations are needed to fully understand how vibrations influence the short- and long-term evolution of the stress field as well as the resulting failure patterns. This can be done by introducing a constant vibration during loading.

Another interesting point is similar to the role of local stress heterogeneities in generating dry microseismicity (Garcia-Teijeiro and Rodriguez-Herrera, 2014). The analysis into the force chain evolution (Figure 6.16) and spatial distribution of bond breakages (Figure 6.6) shows some bonds fail in the weak force zones or close to areas with very large force gradients instead of strong force regions. This implies the importance of the asymmetric force distribution in generating local bond failures. Still, a comprehensive statistical analysis of bond forces and contact forces is required. This will help in understanding how forces are transmitted, how the contact network evolves and accommodates local failure, potentially explaining the formation of the final macroscopic failure.

Bibliography

Aki, K., and Richards, P. G., 2002, Quantitative Seismology: University Science Books.

Anderson, E. M., 1951, The dynamics of faulting and dyke formation with applications to Britain: Oliver & Boyd.

Belardinelli, M. E., Cocco, M., Coutant, O., and Cotton, F., 1999, Redistribution of dynamic stress during coseismic ruptures: Evidence for fault interaction and earthquake triggering: Journal of Geophysical Research: Solid Earth, **104**, no. B7, 14925–14945.

Brace, W. F., Paulding, B. W., and Scholz, C. H., 1966, Dilatancy in the fracture of crystalline rocks: Journal of Geophysical Research, **71**, no. 16, 3939–3953.

Bronson, R., and Costa, G. B., 2008, Matrix Methods: Applied Linear Algebra: Elsevier Science.

Chorney, D., Jain, P., Grob, M., and van der Baan, M., 2012, Geomechanical modeling of rock fracturing and associated microseismicity: The Leading Edge, **31**, no. 11, 1348–1354.

Chorney, D. R., Jain, P., Grob, M., and van der Baan, M., 2014, Numerical analysis of acoustic emissions, the radiated energy and their moment tensors in triaxial deformation tests: 48th US Rock Mechanics/Geomechanics Symposium, ARMA Paper 14-7190.

Chorney, D., 2014, Geomechanical modeling of rock deformation and associated microseismicity: University of Alberta.

Cipolla, C. L., McCarley, D. L., Peterman, F., Nevels, H. F., and Creegan, T., 2005, Effect of well placement on production and frac design in a mature tight gas field: SPE Annual Technical Conference and Exhibition, SPE-95337-MS.

Cotton, F., and Coutant, O., 1997, Dynamic stress variations due to shear faults in a plane-layered medium: Geophysical Journal International, **128**, no. 3, 676–688.

Cundall, P. A., and Strack, O. D. L., 1979, A discrete numerical model for granular assemblies: Geotechnique, **29**, no. 1, 47–65.

Das, S., and Scholz, C. H., 1981, Off-fault aftershock clusters caused by shear stress increase: Bulletin of the Seismological Society America, **71**, no. 5, 1669–1675.

Deresiewicz, H., 1958, Mechanics of granular matter: Advances in applied mechanics, **5**, 233–306.

Ferdowsi, B., Griffa, M., Guyer, R. A., Johnson, P. A., Marone, C., and Carmeliet, J., 2013, Microslips as precursors of large slip events in the stick-slip dynamics of sheared granular layers: A discrete element model analysis: Geophysical Research Letters, **40**, no. 16, 4194–4198.

Ferdowsi, B., Griffa, M., Guyer, R. A., Johnson, P. A., Marone, C., and Carmeliet, J., 2014, Three-dimensional discrete element modeling of triggered slip in sheared granular media: Physical Review E, **89**, no. 4, 042204.

Ferdowsi, B., Griffa, M., Guyer, R. A., Johnson, P. A., Marone, C., and Carmeliet, J., 2015, Acoustically induced slip in sheared granular layers: Application to dynamic earthquake triggering: Geophysical Research Letters, **42**, no. 22, 9750–9757.

Freed, A. M., 2005, Earthquake triggering by static, dynamic, and postseismic stress transfer: Annual Review of Earth Planetary Sciences, **33**, 335–367.

Garcia-Teijeiro, X., and Rodriguez-Herrera, A., 2014, Dependence of stress-induced micro-seismicity on natural fracture properties and in-situ stress: SPE/CSUR Unconventional Resources Conference–Canada, SPE-171632-MS.

Giacco, F., Saggese, L., de Arcangelis, L., Lippiello, E., and Ciamarra, M. P., 2015, Dynamic weakening by acoustic fluidization during stick-slip motion: Physical review letters, **115**, no. 12, 128001.

Gilbert, F., 1973, Derivation of source parameters from low-frequency spectra: Philosophical Transactions for the Royal Society of London. Series A, Mathematical and Physical Sciences, 369–371.

Griffith, A. A., 1924, The theory of rupture: The theory of rupture:, First International Congress Applied Mechanics, 53–63.

Hazzard, J. F., and Young, R. P., 2002, Moment tensors and micromechanical models: Tectonophysics, **356**, no. 1, 181–197.

Hazzard, J. F., and Young, R. P., 2004, Dynamic modelling of induced seismicity: International Journal of Rock Mechanics and Mining Sciences, **41**, no. 8, 1365–1376.

Hazzard, J. F., Young, R. P., and Oates, S. J., 2002, Numerical modeling of seismicity induced by fluid injection in a fractured reservoir: 1023-1030.

Hazzard, J. F., 1998, Numerical modelling of acoustic emissions and dynamic rock behaviour: Keele University.

Hubbert, M. K., and William, W. R., 1959, Role of fluid pressure in mechanics of overthrust faulting: I. Mechanics of fluid-filled porous solids and its application to overthrust faulting:, **70**, no. 2, 115–166.

Hubbert, M. K., and Willis, D. G., 1957, Mechanics of hydraulic fracturing: US Geological Survey, **210**, 153–168.

Hudson, J. A., and Harrison, J. P., 2000, Engineering rock mechanics-an introduction to the principles: Elsevier.

Hulse, D. S. Fracturing process with superimposed cyclic pressure: US Patent 2915122A.

Inglis, C. E., 1913, Stresses in a plate due to the presence of cracks and sharp corners: Transactions of the insititution of naval artchitects, **55**, 219–241.

Itasca Consulting Group Inc., 2008, PFC2D/3D (Particle Flow Code in 2/3 Dimensions), Version 4.0. Minneapolis, MN.

Jaeger, J. C., Cook, N. G. W., and Zimmerman, R., 2009, Fundamentals of rock mechanics: John Wiley & Sons.

Jia, X., Brunet, T., and Laurent, J., 2011, Elastic weakening of a dense granular pack by acoustic fluidization: Slipping, compaction, and aging: Physical Review E, **84**, no. 2, 020301.

Jing, L., and Stephansson, O., 2007, Fundamentals of discrete element methods for rock engineering: theory and applications: Developments in geotechnical engineering, **85**, 1–21.

Jing, L., 2003, A review of techniques, advances and outstanding issues in numerical modelling for rock mechanics and rock engineering: International Journal of Rock Mechanics and Mining Sciences, **40**, no. 3, 283 – 353.

Johnson, P. A., Savage, H., Knuth, M., Gomberg, J., and Marone, C., 2008, Effects of acoustic waves on stick–slip in granular media and implications for earthquakes: Nature, **451**, no. 7174, 57–60.

Johnson, S., Settgast, R. R., Fu, P., and Walsh, S., 2014, Microseismicity and geomechanics: modeling and comparisons: Unconventional Resources Technology Conference, Denver, Colorado, 25-27 August 2014, 1873–1882.

Julian, B. R., Miller, A. D., and Foulger, G. R., 1998, Non-double-couple earthquakes: Reviews of Geophysics, **36**, no. 4, 525–549.

Kilb, D., Gomberg, J., and Bodin, P., 2000, Triggering of earthquake aftershocks by dynamic stresses: Nature, **408**, no. 6812, 570–574.

King, G. C. P., Stein, R. S., and Lin, J., 1994, Static stress changes and the triggering of earthquakes: Bulletin of the Seismological Society of America, **84**, no. 3, 935–953.

Le Calvez, J. H., Craven, M. E., Klem, R. C., Baihly, J. D., Bennett, L. A., and Brook, K., 2007, Real-time microseismic monitoring of hydraulic fracture treatment: a tool to improve completion and reservoir management: SPE Hydraulic Fracturing Technology Conference, SPE-106159-MS.

Lockner, D. A., Byerlee, J. D., Kuksenko, V., Ponomarev, A., and Sidorin, A., 1991, Quasi-static fault growth and shear fracture energy in granite: Nature, **350**, 39–42.

Lockner, D., Byerlee, J., Kuksenko, V., Ponomarev, A., and Sidorin, A., 1992, Observations of quasistatic fault growth from acoustic emissions: International Geophysics, **51**, 3–31.

Lockner, D., 1993, Room temperature creep in saturated granite: Journal of geophysical research, **98**, no. 1, 475–487.

Lu, H., and van der Baan, M., 2016, Simulation of dynamic triggering of acoustic emissions using a bonded-particle method: 50th US Rock Mechanics/Geomechanics Symposium, ARMA Paper 2016-519.

Malvern, L. E., 1969, Introduction to the mechanics of a continuous medium: Prentice-Hall series in engineering of the physical sciences Prentice-Hall.

Marketos, G., and O'sullivan, C., 2013, A micromechanics-based analytical method for wave propagation through a granular material: Soil Dynamics and Earthquake Engineering, **45**, 25–34.

Maxwell, S. C., Shemeta, J. E., Campbell, E., and Quirk, D. J., 2008, Microseismic deformation rate monitoring: Microseismic deformation rate monitoring: SPE Annual Technical Conference and Exhibition, SPE-116596-MS.

Maxwell, S. C., 2011, What does microseismic tell us about hydraulic fracture deformation: CSEG Recorder, **36**, no. 8, 31–45.

Michlmayr, G., Cohen, D., and Or, D., 2012, Sources and characteristics of acoustic emissions from mechanically stressed geologic granular mediaa review: Earth-Science Reviews, **112**, no. 3, 97–114.

Oda, M., Konishi, J., and Nemat-Nasser, S., 1982, Experimental micromechanical evaluation of strength of granular materials: effects of particle rolling: Mechanics of materials, **1**, no. 4, 269–283.

Pankow, K. L., Arabasz, W. J., Pechmann, J. C., and Nava, S. J., 2004, Triggered seismicity in Utah from the 3 November 2002 Denali fault earthquake: Bulletin of the Seismological Society of America, **94**, no. 6B, S332–S347.

Parry, R. H. G., 1995, Mohr circles, stress paths and geotechnics: CRC Press.

Pollitz, F. F., and Johnston, M. J. S., 2006, Direct test of static stress versus dynamic stress triggering of aftershocks: Geophysical research letters, **33**, no. 15.

Potyondy, D. O., and Cundall, P. A., 2004, A bonded-particle model for rock: International journal of rock mechanics and mining sciences, **41**, no. 8, 1329–1364.

Potyondy, D. O., 2007, Simulating stress corrosion with a bonded-particle model for rock: International Journal of Rock Mechanics and Mining Sciences, **44**, no. 5, 677–691.

Radjai, F., Wolf, D. E., Jean, M., and Moreau, J. J., 1998, Bimodal character of stress transmission in granular packings: Physical review letters, **80**, no. 1, 61.

Radjai, F., Topin, V., Richefeu, V., Voivret, C., Delenne, J. Y., Azéma, E., and El Youssoufi, M. S., 2010, Force transmission in cohesive granular media: Mathematical Modeling and Physical Instances of Granular Flows, **1227**, no. 1, 240–259.

Secor, D. T., 1965, Role of fluid pressure in jointing: American Journal of Science, **263**, no. 8, 633–646.

Shearer, P. M., 2009, Introduction to seismology: Cambridge Univeristy Press.

Strang, G., and Fix, G. J., 1973, An analysis of the finite element method: Englewood Cliffs, NJ: Prentice-hall.

Tary, J., Herrera, R., and van der Baan, M., 2013, Time-varying autoregressive model for spectral analysis of microseismic experiments and long-period volcanic events: Geophysical Journal International, **196**, no. 1, 600–611.

Toda, S., Stein, R. S., Reasenberg, P. A., Dieterich, J. H., and Yoshida, A., 1998, Stress transferred by the 1995 Mw= 6.9 Kobe, Japan, Shock: Effect on aftershocks and future earthquake probabilities: Journal of Geophysical Research: Solid Earth, **103**, no. B10, 24543–24565.

Toomey, A., and Bean, C., 2000, Numerical simulation of seismic waves using a discrete particle scheme: Geophysical Journal International, **141**, no. 3, 595–604.

van den Wildenberg, S., van Hecke, M., and Jia, X., 2013, Evolution of granular packings by nonlinear acoustic waves: EPL (Europhysics Letters), **101**, no. 1, 14004.

Vasudevan, K., and Eaton, D. W., 2011, Hydraulic fracturing: Coulomb failure stress in fracture networks: CSEG Recorder.

Warpinski, N. R., Mayerhofer, M., Agarwal, K., and Du, J., 2013, Hydraulic-fracture geomechanics and microseismic-source mechanisms: SPE Journal, **18**, no. 04, 766–780.

Wolhart, S. L., Harting, T. A., Dahlem, J. E., Young, T., Mayerhofer, M. J., and Lolon, E. P., 2006, Hydraulic fracture diagnostics used to optimize development in the Jonah field: SPE Annual Technical Conference and Exhibition, SPE-102528-MS.

Yoon, J. S., Zang, A., and Stephansson, O., 2014, Numerical investigation on optimized stimulation of intact and naturally fractured deep geothermal reservoirs using hydro-mechanical coupled discrete particles joints model: Geothermics, **52**, 165–184.

Young, R. P., Collins, D., Hazzard, J., Heath, A., Pettitt, W. S., Baker, C., Billaux, D., Cundall, P., Potyondy, D., and Dedecker, F., 2004, An innovative 3-D numerical modelling procedure for simulating repository-scale excavations in rock–SAFETI: Proceedings of the Euradwaste04 Conference on Radioactive Waste Management Community Policy and Research Initiatives, Luxembourg.

Zhao, X., and Young, R., 2009, Numerical simulation of seismicity induced by hydraulic fracturing in naturally fractured reservoirs: SPE Annual Technical Conference and Exhibition, SPE-124690-MS.

Zhao, Q., Lisjak, A., Mahabadi, O., Liu, Q., and Grasselli, G., 2014, Numerical simulation of hydraulic fracturing and associated microseismicity using finite-discrete element method: Journal of Rock Mechanics and Geotechnical Engineering, **6**, no. 6, 574–581.

Zoback, M. D., 2010, Reservoir Geomechanics: Cambridge University Press.